Technische Universität München
Lehrstuhl für Aerodynamik

Large-eddy simulation of shock wave/turbulent boundary layer interaction

Maxim S. Loginov

Vollständiger Abdruck der von der Fakultät für Maschinenwesen der Technischen Universität München zur Erlangung des akademischen Grades eines

Doktor-Ingenieurs

genehmigten Dissertation.

Vorsitzender:	Univ.-Prof. W. H. Polifke, Ph.D. (CCNY)
Prüfer der Dissertation:	1. Univ.-Prof. Dr.-Ing. habil. N. A. Adams
	2. Univ.-Prof. Dr.-Ing. habil. R. Friedrich, i.R.
	3. Priv.-Doz. Dr. rer. nat. A. A. Zheltovodov, Russian Academy of Sciences, Novosibirsk

Die Dissertation wurde am 07.07.2006 bei der der Technischen Universität München eingereicht und durch die Fakultät für Maschinenwesen am 29.09.2006 angenommen.

Acknowledgments

This thesis is the result of an international cooperation between the Technical University of Munich (TUM) and the Institute of Theoretical and Applied Mechanics (ITAM) in Novosibirsk. First of all, I would like to thank my doctoral advisers Prof. Nikolaus A. Adams from TUM and Dr. Alexander A. Zheltovodov from ITAM. The first of them introduced me to the state-of-the-art techniques in numerical modeling of turbulent flows, supplied all necessary means for this work and spent enormous amount of time in discussing open problems and proofreading reports. While the latter taught me a lot in physical phenomena involved in shock / boundary layer interactions, pointed my attention to the interesting scientific problems, explained with patience details of the physical experiment and lend countenance in hard times. Also I would like to acknowledge Prof. Rainer Friedrich from TUM for honest interest in my work and for his kind agreement to be my co-examiner.

I am also grateful to Prof. Anatoly A. Maslov and Prof. Vadim A. Lebiga from ITAM for their amiable support and help in resolving different official issues in Novosibirsk encountered during my work in Germany.

The early stage of this work would be impossible without support of Prof. Leonhard Kleiser from the Institute of Fluid Dynamics (IFD) at the Swiss Federal Institute of Technology Zurich (ETHZ). He and his team helped me a lot in the first steps in large-eddy simulations and high-performance computing and provided a friendly atmosphere during my stay in Switzerland. In particular I am thankful to Steffen Stolz, Benjamin Rembold, Andreas Jocksch and other colleagues for helpful advises during my in deep studying and optimization of the code. The SCOPES grant from Swiss National Science Foundation supported that visit.

This work was supported by German Research Foundation (DFG). The computation resources were provided by the High Performance Computing Center Stuttgart (HLRS), its support team is acknowledged for resolving technical problems encountered.

Contents

List of Figures

List of Tables

Nomenclature

Roman symbols

a	speed of sound
$C_f = \frac{\tau_w}{\frac{1}{2}\rho_\infty U_\infty^2}$	skin-friction coefficient
h	compression-decompression corner height
E	total energy
F_E, F_S	convective and diffusive fluxes in streamwise direction
G	filter kernel, Görtler number
G_T	Görtler number for turbulent flow
G_E, G_S	convective and diffusive fluxes in spanwise direction
H_E, H_S	convective and diffusive fluxes in wall-normal direction
J	determinant of Jacobian matrix
k	specific-heats ratio
$M = \frac{U}{a}$	Mach number
p	static pressure
Pr	Prandtl number
q_x, q_y, q_z	heat fluxes in respective direction
Q_N	deconvolution operator
Re	Reynolds number
$Re_\delta = \frac{\rho_\infty^* U_\infty^* \delta^*}{\mu_\infty^*}$	Reynolds number based on boundary layer thickness
$Re_{\delta_1} = \frac{\rho_\infty^* U_\infty^* \delta_1^*}{\mu_\infty^*}$	Reynolds number based on displacement thickness
$Re_\theta = \frac{\rho_\infty^* U_\infty^* \delta_2^*}{\mu_\infty^*}$	Reynolds number based on momentum thickness
$Re_{\delta_2} = \frac{\rho_\infty^* U_\infty^* \delta_2^*}{\mu_w^*}$	Reynolds number based on momentum thickness and wall viscosity
t	time

T	static temperature
$u_\tau = \sqrt{\frac{\tau_w}{\rho_w}}$	friction velocity
U	velocity magnitude
u, u_1	streamwise velocity component
v, u_2	spanwise velocity component
w, u_3	wall-normal velocity component
x, x_1	streamwise coordinate in physical space
y, x_2	spanwise coordinate in physical space
z, x_3	wall-normal coordinate in physical space

Greek symbols

β	compression corner deflection angle
δ	boundary layer thickness
δ_1	displacement thickness
δ_2	momentum thickness
δ_{ij}	Kronecker's delta
μ	dynamic viscosity
$\nu = \frac{\mu}{\rho}$	kinematic viscosity
ν_T	eddy viscosity
λ	intermittency factor
ρ	density
τ_{ij}	viscous stress tensor components $(i, j = 1, 2, 3)$
ξ, ξ_1	streamwise coordinate in computational space
η, ξ_2	spanwise coordinate in computational space
ζ, ξ_3	wall-normal coordinate in computational space
χ	relaxation parameter

Other symbols

$\langle \bullet \rangle$	Reynolds averged quantity
$\{\bullet\}$	Favre averged quantity

Subscripts

$\bullet_S$	separation
$\bullet_R$	reattachment
$\bullet_0$	undisturbed boundary layer
$\bullet_\infty$	free-stream
$\bullet_{VD}$	van-Driest transformed
$\bullet_w$	at the wall

Superscripts

$\bullet^c$	contravariant component
$\bullet'$	fluctuation with respect to Reynolds averged quantity
$\bullet''$	fluctuation with respect to Favre averged quantity
$\bullet^+$	in wall units
$\bullet^*$	dimensional quantity[1]

Abbreviations

ADM	appoximate deconvolution model
DES	detached-eddy simulation
DNS	direct numerical simulation
LES	large-eddy simulation
LIA	linear interaction analysis
LSSM	large-scale shock motion
MILES	monotonically integrated large-eddy simulation
RANS	Reynolds-averged Navier-Stokes
RDT	rapid distortion theory
RMS	root-mean square
RRM	rescaling-recycling method
SGS	subgrid-scale
SRA	strong Reynolds analogy
SWTBLI	shock wave / turbulent boundary layer interaction
TKE	turbulent kinetic energy

[1] All results are presented in non-dimensional form. The reference parameters are given in section 2.2 (page 21), see also table 1.2 (page 14)

Abstract

Well-resolved Large-Eddy Simulations (LES) are performed in order to investigate flow phenomena and turbulence structure of the turbulent boundary layer along a supersonic compression-decompression ramp. For the first time it was possible to reproduce directly a reference experiment with a free-stream Mach number of $M_\infty = 2.95$ and a Reynolds number based on the incoming boundary-layer thickness of $Re_{\delta_0} = 63560$. The effect of subgrid-scales is modeled by the approximate deconvolution model.

An analysis of the results shows a good agreement with reference experiment in terms of mean quantities and turbulence structure. The computational data confirm theoretical and experimental results on fluctuation-amplification across the interaction region. In the wake of the main shock a shedding of shocklets is observed. The temporal behavior of the coupled shock-separation system agrees well with experimental data. The simulation data provide indications for a large-scale shock motion. Also the existence of three-dimensional large-scale streamwise structures, commonly referred to as Görtler-like vortices, is confirmed. The LES provide a reliable and detailed flow information, which helped to improve the understanding of shock-boundary-layer interaction considerably.

Kurzfassung

Mittels gutaufgelöster Grobtruktursimulationen (LES) werden Strömungsphänomene und Struktur der turbulenten Grenzschicht entlang einer Kompressions-Dekompressions-Rampe bei Überschallanströmung untersucht. Zum ersten Mal war es möglich, ein Bezugsexperiment mit einer Anström-Machzahl von $M_\infty = 2.95$ und einer Reynoldszahl von $Re_{\delta_0} = 63560$ direkt zu reproduzieren. Eine Analyse der Resultate zeigt eine gute Übereinstimmung zwischen Simulation und Referenzexperiment hinsichtlich statistischer Mittelwerte, wie z.B. der Stoßposition, Lage von Strömungsablösung und -wiederanlegen, Wandreibungs- und Oberflächendruckverteilungen und Turbulenzstruktur. Unmittelbar hinter dem Stoßsystem werden schwache, eingebettete Stöße generiert, die stromab konvektieren. Anhand der Simulationsdaten können auch Hinweise für eine großskalige Stoßbewegung gefunden werden. Ebenfalls kann die Existenz dreidimensionaler, großer, stromaborientierter Görtler-artiger Wirbel bestätigt werden.

Chapter 1

Introduction

Design of new high-speed vehicles requires a detailed knowledge of the flow behavior at supersonic and hypersonic speeds. Traditionally, the experiment was the major source of such knowledge. Growing computer power and development of reliable numerical techniques made it possible to obtain more detailed data from numerical modeling. Currently the flow field around an entire aircraft configuration can be modeled numerically based on inviscid and viscous models (Agarwal, 1999). Utilizing the Euler equations allows to capture the global flow structure, but because viscosity is neglected it cannot predict separation related to viscous-inviscid interaction (e.g. Volkov *et al.* (2002); Volkov & Loginov (2000)). Obtaining reliable results in case of turbulent flow, which is virtually every flow encountered in practical applications, is even more complicated. In spite of more than a century of research on turbulent motion, a closed theory still does not exist. Shock waves and their interaction with turbulent boundary layers are accompany flight at supersonic speeds. The shock wave / turbulent boundary layer interaction (SWTBLI) can have very complicated appearance. It usually occurs in inlets, near deflected control surfaces, near surfaces junctions, and has a big influence on structural loads, sometimes causing aircraft damage. This necessitates a reliable prediction tool with the ability to capture all relevant physical phenomena.

Two basic ways of computing turbulence have traditionally been direct numerical simulation (DNS) and Reynolds-averaged (RANS) modeling. In the former, the full, time-dependent, Navier-Stokes equations are solved numerically, essentially without approximations. The results are expected to be equivalent to experimental ones. In the latter, only the statistical mean flow is computed, and the effect of the turbulent fluctuations is modeled according to a variety of physical approximations. It was realized early that direct numerical simulations were too expensive for most cases of industrial interest, while Reynolds-averaged modeling was too dependent on the characteristics of particular flows for being generally applicable. Large-eddy simulations (LES) were developed as an intermediate approximation between these two approaches, the general idea being that the large, non-universal, scales of the flow were to

be computed explicitly, as in DNS, while the small scales were modeled. The hope was that the small scales, which are neglected from flow inhomogeneities and particular boundary conditions by several steps of the turbulent cascade, would be universal (independent of the particular flow) and isotropic enough for a single simple model to be able to represent them in all situations.

1.1 Flow physics of SWTBLI

For supersonic flows the interaction of turbulent boundary layers with shocks and rarefaction waves is one of the most prevalent phenomena governing the overall flow structure. Research on SWTBLI interaction commonly employs a range of canonical flow configurations. Among the canonical configurations two- and three-dimensional and axisymmetric geometries are considered: impinging normal shocks, oblique-shock reflections, compression ramps and one- and two fins mounted on a flat plate, cavity flows. For a detailed survey of the current knowledge on SWTBLI, mainly drawn from experiments, the reader is referred to Delery & Marvin (1986), Settles & Dolling (1990), Smits & Dussauge (1996), Zheltovodov (1996), Andreopoulos *et al.* (2000) and Dolling (2001). A generic feature of such flows is that the shock wave, formed by a deflected surface or by an external shock generator, alters the supersonic turbulent boundary layer developing along the surface. The changes can be local, but for sufficiently large pressure rise, the boundary layer separates and a separation region with reverse flow at the wall appears. The pressure distribution reveals a characteristic plateau region with almost constant pressure for the developed separation zones.

A compilation of a large range of available experimental data is provided by Settles & Dodson (1991, 1994). More than hundred studies were subjected to a test based on rigorous criteria and nineteen high-quality experiments on supersonic and hypersonic SWTBLI, suitable for use in turbulence modeling, were extracted. The data include axisymmetric, two- and three-dimensional interactions in a wide range of Mach and Reynolds numbers. Settles & Dodson (1994) recognized that selected cases do not cover realistic flight conditions for a modern aerospace vehicle, which operates on higher Mach and Reynolds numbers. On the other hand, currently only a low Reynolds number range is affordable for DNS/LES simulations due to limited computer power. Very few experiments exist in this range, making validation of DNS/LES difficult.

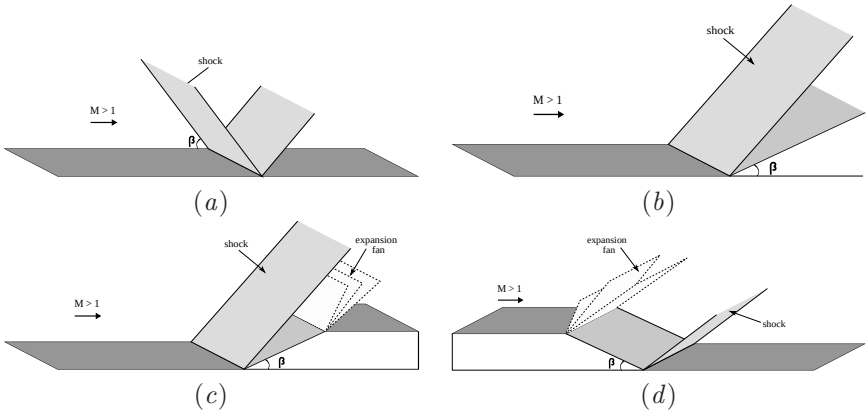

Figure 1.1: Examples of canonical configurations.

Recently some efforts in this direction are made by Bookey *et al.* (2005).

Engine-inlets as well as some other elements of supersonic planes often use successive forward and backward-facing ramp configurations, so that along with simplified configurations (figure 1.1*a,b*) also generic compression-decompression and decompression-compression ramps (figure 1.1*c,d*) are investigated. These interactions combine the effects of the mean shear, a longitudinal pressure gradient, the streamline curvature, volumic compression, and unsteady effects caused by separation. Seminal contributions on compression-corner flows were made by Settles *et al.* (1979), Dolling & Murphy (1983), and Smits & Muck (1987).

Essential flow phenomena for compression-decompression ramps are sketched in figure 1.2, following Zheltovodov (1991). The undisturbed incoming turbulent boundary layer is deflected at the compression corner. The resulting compression shock penetrates into the boundary layer where the penetration depth depends on the local Reynolds number (Adamson & Messiter, 1980). For sufficiently large deflection angles the rapid compression within the boundary layer results in a region of mean-flow separation near the compression corner. The separation region is surrounded by a detached shear layer which reattaches at the deflected part of the compression ramp. A λ-shock system is generated near the separation region. The forward foot of the λ-shock originates

from the region of flow separation, the rearward foot from the region of flow reattachment. Further downstream, the reattached boundary layer reaches the decompression ramp and passes through the Prandtl–Meyer expansion. Even further downstream, the boundary layer relaxes again towards a developed zero-pressure-gradient boundary layer.

In figure 1.2 separation and reattachment lines are indicated by S and R, respectively. Turbulence is amplified by interaction with a rapid compression within the boundary layer (item 1) and by direct interaction with the shock in the external flow, item 2. Note also that the shock foots spread out towards the wall due to reduced local Mach number and due to turbulent diffusion. Item 3 points to the damping of turbulent fluctuation by the interaction with the expansion wave at the expansion corner. After reattachment at the deflected part of the compression ramp a turbulent boundary layer is reestablished, item 4. Experimental and computational results, which are discussed in section 4, support the existence of pairs of large counterrotating streamwise vortices in the reattachment region, item 5. Within the area of flow separation the reverse mean flow has the character of a wall jet which exhibits indications of relaminarization, item 6.

The shock-turbulence interaction in free and wall-bounded flows is reviewed by Andreopoulos *et al.* (2000). Turbulence amplification through shock wave interactions is a direct effect of the Rankine-Hugoniot relations applied in the instantaneous sense. In turn changing conditions in front of and behind the shock cause it to deform and oscillate. The mutual influence makes the interaction very complex. Three major factors in the interaction can be identified: mean flow compression across the shock, shock front curvature, and unsteady shock front motion. Kovasznay (1953) suggested to decompose small-amplitude fluctuations into three elementary modes of mutually independent fluctuations: vortical, acoustic, and entropic. Linear interaction analysis (LIA), developed by Ribner (1954), relates the turbulent fluctuations downstream of the shock wave with the orientation, amplitude, and length scale of incident elementary wave. LIA, assumed a small fluctuation, such that the Rankine-Hugoniot condition can be linearized, also valid in case of evident shock front deformation. On the other hand rapid distortion theory (RDT) was found inappropriate for the analysis of shock/turbulence interaction, since the shock front curvature and the shock front unsteadiness cannot be accounted for in the analysis (Lee *et al.*, 1997). Anyiwo & Bushnell (1982) identify primary mechanisms of turbulence enhance-

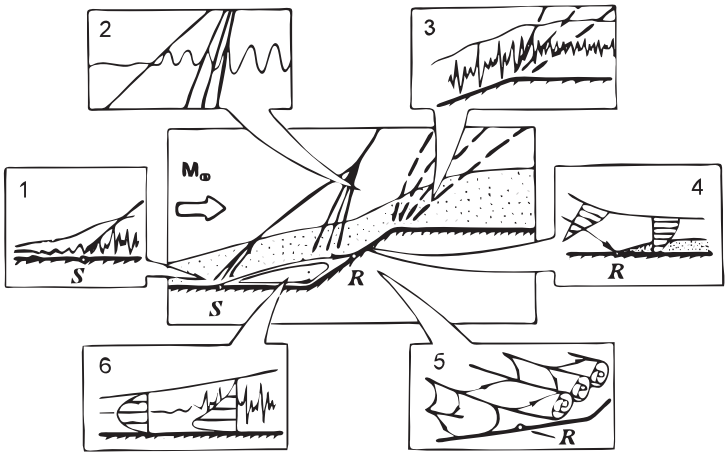

Figure 1.2: Essential flow phenomena in compression ramp flows (for explanations see text on page 4)

ment: amplification of the vorticity mode, generation of acoustic and entropy modes from the interaction, and turbulence pumping by shock oscillations.

Near the decompression corner the flow experiences a short region of favorable pressure gradient, as well as stabilizing effects of convex curvature. It is found that the expansion wave / boundary layer interaction reduces the intensity of turbulent fluctuations (Smits & Wood, 1985; Zheltovodov & Yakovlev, 1986). The experimentally determined temperature/velocity correlation coefficient of about 0.8 supporting the validity of the strong Reynolds analogy (SRA) of Morkovin (1962) in this region. Furthermore, a rapid distortion analysis demonstrated reasonable agreement with the experimental results. Knight *et al.* (2003) provide a review of the compressible turbulent boundary layers in the compression/expansion corners.

The unsteadiness of the shock is an important feature of separated flows. It was observed for different configurations: two-dimensional and swept corner interactions and wall-mounted blunt fins. The shock foot motion can be described by two primary components: a low frequency,

large-scale motion and a high frequency, small-scale motion. The characteristic frequencies of these components differ significantly: in the unswept compression corner interaction the order of magnitude of the first motion it is about 100Hz, while for the latter one is about 10000Hz Dolling (2001). Note that the use of the terms *high – low* frequency and *large – small* scales refer to the shock, not the turbulent scales of the boundary layer. Andreopoulos & Muck (1987) found that small-scale shock oscillation is indeed driven by the oncoming large-scale turbulent fluctuations. Erengil & Dolling (1991) confirmed their conclusions, evaluating a correlation between the wall pressure fluctuations beneath the incoming boundary layer and the shock foot velocity. The large-scale shock motion (LSSM) was also observed. There are several theories trying to explain LSSM. According to the experiment of Erengil & Dolling (1991) the large-scale motion is a result of the shock displacement due to the expansion and contraction of the separation bubble. A physical model of the shock unsteadiness was developed from these observations, in which the expansion and contraction of the separation bubble displaces the shock upstream or downstream. Plotkin (1975) suggested a one-dimensional theory, which is based on perturbation of a shock by random fluctuations in the incoming turbulent flow. This model mimics the manner analogous to linearly damped Brownian motion, in which relatively broadband perturbations in the incoming turbulent flow lead to relatively low-frequency motion of the separation bubble and its associated shock system. Recently Poggie & Smits (2001, 2005) re-evaluate data of blunt fin interactions and reattaching shear layers and found that Plotkin's theory can describe shock motion with good accuracy. Recently J.-P. Dussauge & J.-F.Debiève (2006) in their shock reflection experiment found a connection between downstream vortical structure and low frequency shock motion. The vortical structures have frequency scales of the same order as the dominant shock motion frequencies. A frequency scaling based on the separation length and on the upstream external velocity as suggested formerly by Erengil & Dolling (1991) is likely to be the proper scaling for the flow. Finally, the experimental setup might have an artificial influence on large-scale low-frequency shock motion (Dolling, 2001). For example, the Görtler vortices developing in the nozzle of the wind tunnel may introduce temporal variations in the incoming boundary layer, which cause LSSM.

Streamwise vortices affect the turbulence structure and the properties of the mean flow significantly (Inger, 1977; Brazhko, 1979; Zheltovodov

et al., 1983; Zheltovodov & Yakovlev, 1986; Floryan, 1991; Simeonides, 1993; Lüdeke *et al.*, 2004). Probably the first who observed and documented the streamwise vortices in reattaching supersonic turbulent flow was Ginoux (1971). Experiments on backward facing steps and axisymmetric hollow cylinder flare showed a striation pattern at the surface with a wavelength of about two to three boundary layer thicknesses. An influence of streamwise vortices on skin-friction and heat-transfer distribution in spanwise direction and limiting streamline pattern with saddle and nodal points near reattachment was suggested. Based on oil-flow visualizations Zheltovodov *et al.* (1983) proposed a more detailed pattern of limiting streamlines presented in figure 1.3(a). Along the reattachment line (divergence line in oil-flow pattern) nodal and saddle points can be identified. Downstream of the reattachment line clear footprints of vortices appear. Inside the separation zone such footprints are only weak. From the surface flow pattern also the existence of singular (saddle and nodal) points on the upstream located convergence line can be implied. There are two convergence lines near separation, caused probably by the unsteadiness of the separation-shock system. Based on these observations a Görtler-like vortex configuration can be inferred as shown in figure 1.3(b).

A generic model of the deflected X-38 flap was investigated by Lüdeke *et al.* (2004) using a 20°-degree ramp under $M_\infty = 3$. Artificial perturbations were introduced near the leading edge of the flat plate by using thin foils in the shape of a zigzag band. The influence of the perturbation magnitude and wavelength on the vortices was investigated by varying the thickness of the foil and cusp distance. The vortices did not appear until the perturbation magnitude exceeded a certain value, i.e. as long as the wall can be assumed as hydraulically smooth. Different perturbation wavelengths result in similar vortex width, and circular vortices were most amplified. The facts support the interpretation that a mechanism selecting a certain wavelength exists.

1.2 Referenced experiments

A series of experiments for forward- and backward facing steps was performed in the Institute of Theoretical and Applied Mechanics by Zheltovodov *et al.* (1983); Zheltovodov & Yakovlev (1986); Zheltovodov *et al.* (1987); Borisov *et al.* (1993). The data obtained in the experiments are well validated and were found to be accurate enough to include them

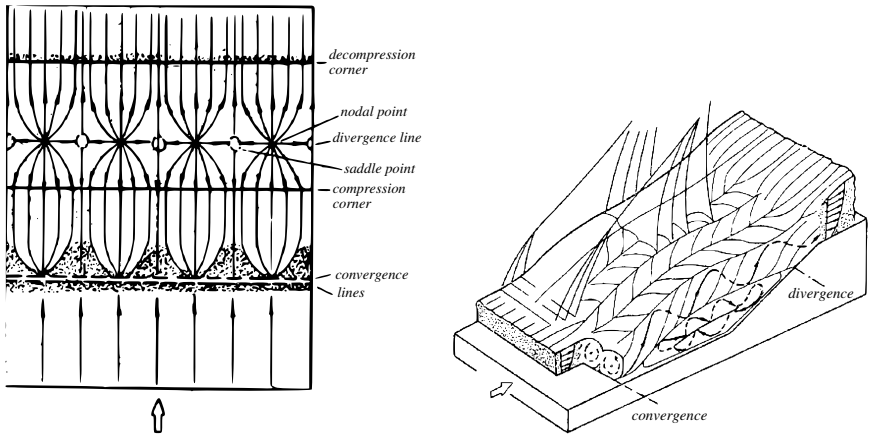

Figure 1.3: Experimentally suggested flow field with streamwise vortices.

into the database of Settles & Dodson (1994). The experimental data are available in tabulated form and described in detail by Zheltovodov *et al.* (1990). The experiments were performed using two models of the same shape, but of different linear scales: the big one had a step height of $h = 15$mm, whereas $h = 6$mm for the small model. The surface deflection angles were $\beta = \pm 8°; \pm 25°; \pm 45°; 90°$, the negative sign corresponding backward facing steps.

The mean flow is investigated in detail for the big forward facing step with a free-stream Mach number of $M_\infty = 2.9 \pm 1.5\%$ and Reynolds number of $Re_{\delta_0} = 110000 - 150000$. For this purpose static and pitot pressure are measured along vertical lines at several downstream stations, the velocity was obtained using Crocco's relation. The validity of this relationship has been verified by optical measurements of the density field (Zheltovodov, 1979). The surface-pressure distribution and the skin-friction coefficient, obtained from the velocity profiles, are also available. Surface oil-flow techniques and Schlieren photographs are used for flow visualization. Additional experiments have been performed at $M_\infty = 2.25$ and 4 (Zheltovodov *et al.*, 1983).

The turbulence characteristics are investigated for the small model

under free-stream conditions $M_\infty = 2.95$ and $Re_{\delta_0} = 63560$ (Zheltovodov & Yakovlev, 1986). A constant-current hot-wire measurement was employed to obtain total temperature and mass-flux fluctuations, based on the technique of Kovasznay (1953). The mass-flux fluctuation was decomposed into density and velocity fluctuations using the strong Reynolds analogy. The mean skin-friction measurements were performed by the Global Interferometry Skin Friction technique (GISF) (Borisov *et al.*, 1993).

Heat transfer measurements for the small model were performed by Zheltovodov *et al.* (1987) at free-stream conditions $M_\infty = 2.9$, $Re_{\delta_0} = 86520$ and $M_\infty = 4$, $Re_{\delta_0} = 100000$. The data include adiabatic and heated-wall temperature distributions and the heat transfer coefficient.

An experimentally obtained flow field structure and the measurement stations are sketched in figure 1.4 for a 25°-degree compression ramp. The positions of the stations in terms of the downstream coordinate measured along the wall from the compression corner position, are summarized in table 1.1. Obviously, the big model allowed more detailed measurements of the mean flow. The Reynolds numbers based on the undisturbed boundary layer thickness are $Re_{\delta_0} = 144000$ and $Re_{\delta_0} = 63560$ for big and small models respectively. Despite of significant Reynolds number differences, the mean flow structure is rather similar if scaled in δ_0 as shown by Zheltovodov & Yakovlev (1986), so both experiments may be used together for a detailed analysis.

1.3 Prediction capabilities

As pointed out by Dolling (1998, 2001) and confirmed by a more recent comprehensive analysis (Knight *et al.*, 2003) the numerical prediction of SWTBLI by statistical turbulence modeling is yet unsatisfactory. For situations with shock-induced flow separation computational results employing Reynolds-averaged (RANS) turbulence modeling exhibit a large scatter of predicted separation lengths for various geometrical configurations. Although numerous computations based on the Reynolds-averaged Navier-Stokes equations (RANS) have been performed, currently only weak and moderate interactions, characterized by low supersonic Mach number or small flow deflection angles, can be predicted by RANS computations without specific *a posteriori* adjustment of turbulence models. For strong interactions, the results of RANS computations show generally a significant disagreement with experimental data

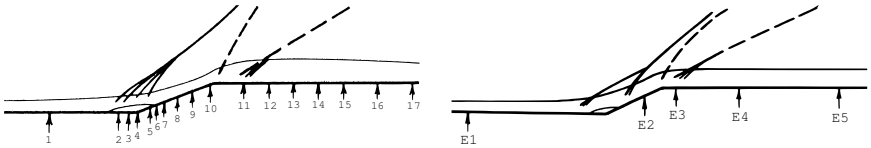

(a) (b)

Figure 1.4: Sketch of flow structure and measurement stations for big (a) and small (b) forward facing steps with $\beta = 25°$.

Symbol	$x_1^*, [mm]$	x_1
1	-3.3	-8.05
2	-1.2	-2.93
3	-0.8	-1.95
4	-0.5	-1.22
5	0.5	1.22
6	1.1	2.68
7	1.25	3.05
8	1.7	4.15
9	2.35	5.73
10	3.1	7.56
11	5.0	12.20
12	6.25	15.24
13	7.85	19.15
14	9.85	24.02
15	11.7	28.54
16	13.6	33.17
17	15.05	36.71

(a)

Symbol	$x_1^*, [mm]$	x_1
E1	-35.	-15.42
E2	10.	4.41
E3	18.	7.93
E4	34.	14.98
E5	59.	25.99

(b)

Table 1.1: Streamwise distance of the measurement stations for big (a) and small (b) forward facing steps with $\beta = 25°$.

in terms of surface pressure, skin friction, and heat transfer distributions. Furthermore, these approaches turn out to be unable to predict the unsteadiness of the shock system, which is, however, a very important feature of SWTBLI. Comprehensive summaries of the current status of computational fluid dynamics (CFD) on the prediction of SWTBLI are due to Zheltovodov *et al.* (1992); Zheltovodov (1996), and Knight & Degrez (1998).

A main deficit of RANS approaches is that for unsteady flows, statistical turbulence modeling can be expected to reproduce the proper temporal mean-flow behavior only if mean-flow time scales and fluctuation time scales are separated so that standard assumptions involved in turbulence modeling can be applied. This is not the case for SWTBLI because of its essential unsteadiness. Sinha *et al.* (2005) proposed a shock-unsteadiness correction for $k-\epsilon$, $k-\omega$ and Spalart-Allmaras turbulence models. The simulations in 16, 20 and 24°-degree compression corners demonstrated an improvement over existing models, although the length of the separation zone was not predicted correctly.

An alternative to RANS are the Large-Eddy-Simulation (LES) and Direct Numerical Simulation (DNS) approaches. DNS recovers the entire temporal and spatial flow information. Since all relevant flow scales need to be resolved DNS is limited essentially by the available computer power. In practice, only rather small Reynolds numbers and narrow computational domains can be considered. The range of flow parameters where most of experimental data are available cannot be reached. Spatial and temporal resolution requirements can be lowered by employing LES at the expense of modeling the effect of discarded scales. For LES, evolution equations for the low-pass filtered solution are solved. The instantaneous interaction of these so-called resolved scales with the remainder range of scales needs to be modeled. For a comprehensive account of current LES the reader is referred to the textbooks of Sagaut (2002); Garnier *et al.* (2007). Nevertheless, LES maintains the main advantages of DNS, namely providing the full spatial and temporal flow information down to the smallest resolved scales. Based on recent advances in modeling and computing, LES nowadays can be considered as the most appropriate numerical tool for the analysis of complex unsteady transitional and turbulent flows. However, as pointed out by Knight *et al.* (2003) and Zheltovodov (2004), even LES predictions need to be interpreted with care.

LES simulations can be very expensive at high (experimental)

Reynolds numbers mainly because of resolution requirements near the wall. Different techniques are investigated in order to decrease computational costs. Detached-eddy simulation (DES) (Squires, 2004) and wall modeling (Moin, 2002) are common examples. The DES approach attempts to treat near-wall regions in a RANS-like manner, and treat the rest of the flow in an LES-like manner. The second approach utilizes wall functions, which provide an algebraic relationship between the local wall stresses and the tangential velocities at the first off-wall velocity nodes.

Zheltovodov (2004) and Knight *et al.* (2003) provide an extensive comparison of RANS and LES, applied to supersonic compression ramps. The numerical details of compression ramp simulations can be found in appendix B. Probably the first attempt of an LES for a compression-ramp flow was done by Hunt & Nixon (1995), who qualify their simulation as a very large-eddy simulation. The results show some agreement with the experiment of Dolling & Murphy (1983), e.g. in terms of the shock-motion frequency. For a weak interaction at a free-stream Mach number of $M_\infty = 3$ and a ramp deflection angle of $\beta = 8^\circ$ no mean-flow separation was found in the LES of Urbin *et al.* (1999), Kannepalli *et al.* (2002), and El-Askary *et al.* (2003), although instantaneous reverse flow regions may exist. A thin separation zone was observed in the DNS of Adams (2000) at $M_\infty = 3, \beta = 18^\circ$. No large-scale shock motion (LSSM) was found. The observed small-scale shock-motion has a dominant frequency which is close to the inverse characteristic time scale of bursting events within the incoming boundary layer. An instantaneous Schlieren-type visualization exhibits compression waves shed by the main compression shock above the separated shear layer and downstream of the interaction. These DNS results were confirmed by the LES of Stolz *et al.* (2001*a*) and by von Kaenel *et al.* (2004) for the same configuration. For both LES the approximate deconvolution model (ADM) was employed for sub-grid scale (SGS) modeling, whereas finite-volume discretization is used in the latter.

The same free-stream flow parameters as in Adams (2000) were considered by Rizzetta *et al.* (2001) and El-Askary *et al.* (2003). Computations without SGS model agreed with LES with a Smagorinsky model and with a dynamic model at the same resolution, indicating that the effect of the employed SGS model was negligible. No agreement was found with the results of Adams (2000) in terms of skin-friction and surface-pressure distribution in the interaction area. Aside of the mod-

eling issues, the main reason for this disagreement is that the incoming boundary layers were different. A case with a strong interaction was studied by Urbin *et al.* (2000) and Yan *et al.* (2000, 2001) at $M_\infty = 3$ and $\beta = 25°$. A range of deflection angles $\beta = 8°, 16°, 20°, 24°$, corresponding to experiments of Smits & Muck (1987), Dolling & Murphy (1983) and data of Settles & Dodson (1991), was investigated by Rizzetta & Visbal (2002). The latter case of $\beta = 24°$ was also considered by Kannepalli *et al.* (2002). However, for all these computations the momentum-thickness Reynolds number of the incoming boundary layer was about one to two orders of magnitude smaller than for the experiments. For none of these computations a developed pressure plateau near the corner was observed, a result which is typical for low Reynolds numbers. Also the separation length was not reproduced correctly. There was no LSSM found and the temporal evolution of the shock-separation system, in terms of the surface-pressure intermittency, exhibits quantitative differences from the experiment. Recently Smits *et al.* (2006) presented results for a DNS of a 24°-compression corner at a free-stream Mach number $M = 2.9$ and an incoming-boundary-layer momentum-thickness Reynolds number of $Re_\theta = 2900$, corroborating the above findings. Only a preliminary analysis and comparison with the experiment of Bookey *et al.* (2005) at the same Reynolds number is provided. So far there is to our knowledge no direct comparison with a compression-ramp experiment. The only example of a successful comparison between experiment and LES is the work of Garnier *et al.* (2002), who investigated impinging shock / turbulent boundary layer interaction using a mixed-scale model and found a good agreement of mean and turbulent quantities.

For some simulations the separation length agrees with the experiment although the experimental Reynolds number is much larger. This fact contradicts the dependency of the separation length on Reynolds number as reported by Knight *et al.* (2003). Most of the currently available analysis is restricted to spanwise-averaged flow data and a detailed investigation of the flow structure is not available. An open question is the existence of large-scale periodic streamwise vortex structures in the reattaching flow and their origin. Experimental oil-flow patterns suggest the presence of pairwise counter-rotating vortices near reattachment. For a transitional interaction Comte & David (1996) found Görtler-like vortices for an LES of the boundary-layer along a generic body-flap configuration at $Re_{\delta_0} \approx 840$, where δ_0 is the incoming boundary-layer thickness. It was shown that these vortices have a strong effect on local skin friction

Parameter	value
M_∞	2.95
β	25°
Re_{δ_0}	63560
$U^*_\infty, [m/s]$	614.6
$T^*_\infty, [K]$	108
$\rho^*_\infty, [kg/m^3]$	0.314
$\mu^*_\infty, [kg/(ms)]$	6.89×10^{-6}
$\delta^*_0, [mm]$	2.27
$\delta^*_1, [mm]$	0.79
$\delta^*_2, [mm]$	0.15

Table 1.2: Free-stream conditions of the reference experiment.

and heat transfer.

Simulation considering more complex interactions with different types of perturbations imposed onto the turbulent boundary layer sequentially are not numerous. Xiao *et al.* (2003) used a hybrid LES/RANS approach to calculate full 25° compression-decompression ramp configuration at the same flow conditions as the experiment of Zheltovodov *et al.* (1983). Knight *et al.* (2001) computed the backward facing step at $Re_{\delta_0} = 2000$.

1.4 Objectives of the present work

The objective of the numerical investigation is a direct comparison with an available experiment, along with a detailed investigation of the instantaneous and the averaged flow structure. For this purpose all flow parameters and the flow geometry are matched to an available experiment of Zheltovodov *et al.* (1983) and Zheltovodov & Yakovlev (1986). The free-stream Mach number is $M_\infty = 2.95$, the Reynolds number based on the incoming boundary-layer thickness is $Re_{\delta_0} = 63560$, the ramp deflection angle is $\beta = 25°$. The experimental conditions are collected in table 1.2, where the data corresponding to the undisturbed boundary layer are included. In the following we refer to the experiment at these conditions as "reference experiment" (figure 1.4*b*). Additional experimental data at $M = 2.9$ and $Re_{\delta_0} = 144000$ for the same geometry will be used and

referred to as "higher-Reynolds-number experiment" (figure 1.4*a*). By matching directly the experimental parameters, the prediction quality of the employed sub-grid-scale model can be assessed without further assumptions. Given a successful validation, the computational results provide a reliable source for further analysis.

While the reference experiment is done for the entire compression-decompression ramp configuration, in the simulation we split this configuration into two parts, namely, the compression- and the decompression-corner part. The reason for splitting the problem into two parts is twofold. First, the estimated computational cost of well-resolved LES for the full configuration is rather large and leads to rather long computational times. Second, the compression-corner interaction is sufficiently complex to justify a separate investigation. Preliminary compression-corner results based on the analysis of limited statistical data were given by Loginov *et al.* (2004*c*, 2006*b*).

In section 2 we provide the problem formulation and give a brief summary of the simulation method which is essentially the same as in Stolz *et al.* (2001*a*). A simulation for the turbulent boundary layer along a flat plate was used to provide inflow data for the compression ramp. Results for this precursor simulation are summarized in section 3. The main subject of this paper is the analysis of the compression-corner flow in section 4. A discussion of results of the successive decompression corner simulation is given in section 5. The last section 6 gives a summary and final conclusions.

Chapter 2

Simulation method

2.1 Domain and grid

A well-resolved LES for the full configuration requires about 29 million gridpoints. It requires a lot of memory (about 15 Gb) and computational time (about 35 000 CPUh), leading to huge simulations on a current supercomputer. For this reason the domain of the full configuration (figure 2.1a) was split into two parts, namely the compression and the decompression corner part, as shown in figure 2.1(b). The domain size is chosen according to the reference experiment, the arrows denote experimental stations $E1 - E4$ (figure 1.4b). The domain does not cover the experimental station $E5$ since it would almost double the gridsize for the same resolution requirements. The compression-corner domain is continued beyond the decompression corner position ensuring that outflow boundary condition does not affect the upstream flow. The upstream influence of the decompression corner is not modeled in the first simulation. The inflow section of the decompression-corner domain is matched to a cross-section of the compression-corner domain. The station $E2$ belongs to both domains, allowing for a cross-check of the results. The spanwise domain size is chosen wide enough so that large-scale coherent structures such as Görtler-like vortices can be captured.

A generalized-coordinate formulation of the compressible Navier-Stokes equations (NSE) in conservation form is employed. The NSE are written in the Cartesian (x_1, x_2, x_3) physical space, using a transformation to computational space (ξ_1, ξ_2, ξ_3) as detailed by Adams (1998). The computational-space coordinates are orthogonal and normalized, where ξ_1 corresponds to the streamwise direction, ξ_2 to the spanwise direction and ξ_3 to the wall-normal direction. Note that the lines $\xi_1 = const$ and $\xi_3 = const$ are non-orthogonal in physical space, see figure 2.2. In this figure a side-view of the computational meshes of compression and decompression parts are shown, where only every 10th mesh line is displayed. For conciseness we use a tensor notation with summation convention. Since only two-dimensional configurations in the (x_1, x_3)-plane are considered, the spanwise direction x_2

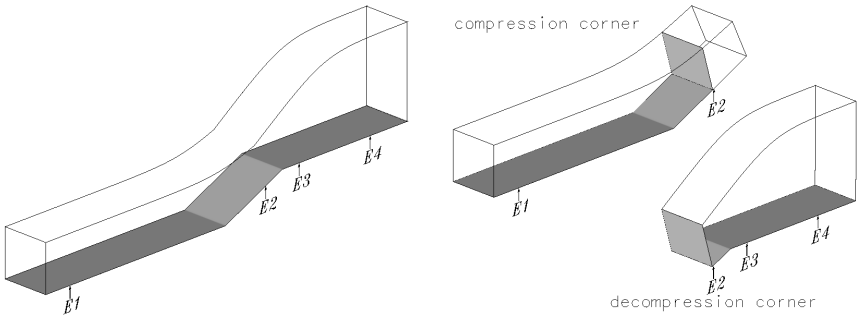

Figure 2.1: Domain splitting.

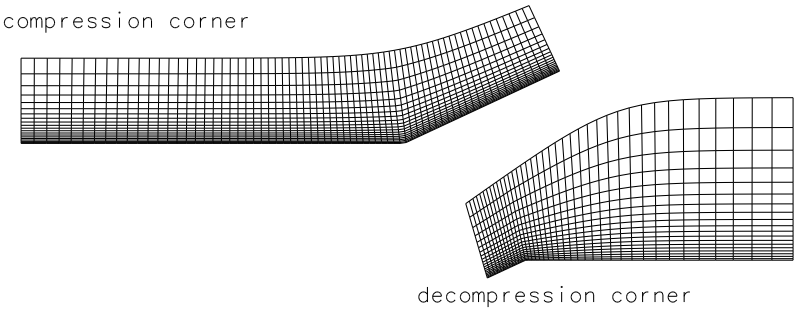

Figure 2.2: Computational mesh (each 10th line is shown).

is orthogonal on the (x_1, x_3) plane and ξ_2 is mapped onto x_2 linearly. Further domain and grid details are given below. In the following we use synonymously $\{x_1, x_2, x_3\} \equiv \{x, y, z\}$, $\{\xi_1, \xi_2, \xi_3\} \equiv \{\xi, \eta, \zeta\}$ and $\{u_1, u_2, u_3\} \equiv \{u, v, w\}$ for notational convenience.

2.2 Governing equations

The compressible Navier-Stokes equations in curvilinear coordinates are written as

$$\frac{\partial}{\partial t}\frac{f}{J}+\frac{\partial}{\partial \xi}\frac{F_E}{J}+\frac{\partial}{\partial \eta}\frac{G_E}{J}+\frac{\partial}{\partial \zeta}\frac{H_E}{J}=\frac{\partial}{\partial \xi}\frac{F_S}{J}+\frac{\partial}{\partial \eta}\frac{G_S}{J}+\frac{\partial}{\partial \zeta}\frac{H_S}{J} \quad , \quad (2.1)$$

where the conservative variables are $f = \{\rho,\ \rho u_1,\ \rho u_2,\ \rho u_3,\ E\}$. The convective fluxes F_E, G_E, H_E are defined as:

$$F_E = \left\{ \begin{array}{c} \rho(u\xi_x + w\xi_z) \\ \rho u(u\xi_x + w\xi_z) + p\xi_x \\ \rho v(u\xi_x + w\xi_z) \\ \rho w(u\xi_x + w\xi_z) + p\xi_z \\ (E+p)(u\xi_x + w\xi_z) \end{array} \right\}, \qquad G_E = \left\{ \begin{array}{c} \rho(v\eta_y) \\ \rho u(v\eta_y) \\ \rho v(v\eta_y) + p\eta_y \\ \rho w(v\eta_y) \\ (E+p)(v\eta_y) \end{array} \right\},$$

$$H_E = \left\{ \begin{array}{c} \rho(u\zeta_x + w\zeta_z) \\ \rho u(u\zeta_x + w\zeta_z) + p\zeta_x \\ \rho v(u\zeta_x + w\zeta_z) \\ \rho w(u\zeta_x + w\zeta_z) + p\zeta_z \\ (E+p)(u\zeta_x + w\zeta_z) \end{array} \right\}$$

and F_S, G_S, H_S are the diffusive fluxes:

$$F_S = \left\{ \begin{array}{c} 0 \\ \tau_{xx}\xi_x + \tau_{xz}\xi_z \\ \tau_{xy}\xi_x + \tau_{yz}\xi_z \\ \tau_{xz}\xi_x + \tau_{zz}\xi_z \\ -q_x\xi_x - q_z\xi_z + (u\tau_{xx} + v\tau_{xy} + w\tau_{xz})\xi_x + (u\tau_{xz} + v\tau_{yz} + w\tau_{zz})\xi_z \end{array} \right\},$$

$$G_S = \left\{ \begin{array}{c} 0 \\ \tau_{yx}\eta_y \\ \tau_{yy}\eta_y \\ \tau_{yz}\eta_y \\ -q_y\eta_y + (u\tau_{yx} + v\tau_{yy} + w\tau_{yz})\eta_y \end{array} \right\},$$

$$H_S = \left\{ \begin{array}{c} 0 \\ \tau_{xx}\zeta_x + \tau_{xz}\zeta_z \\ \tau_{xy}\zeta_x + \tau_{yz}\zeta_z \\ \tau_{xz}\zeta_x + \tau_{zz}\zeta_z \\ -q_x\zeta_x - q_z\zeta_z + (u\tau_{xx} + v\tau_{xy} + w\tau_{xz})\zeta_x + (u\tau_{xz} + v\tau_{yz} + w\tau_{zz})\zeta_z \end{array} \right\}$$

in the respective coordinate directions. $J = \xi_x\zeta_z - \xi_z\zeta_x$ is the Jacobian of the mapping $(x, z) \leftrightarrow (\xi, \zeta)$. A linear mapping of y to η results in a constant mapping coefficient $\eta_y = 1/L_y$. The normal stresses are defined as

$$\tau_{xx} = \frac{\mu}{Re}\left[\frac{4}{3}\left(\frac{\partial u}{\partial \xi}\xi_x + \frac{\partial u}{\partial \zeta}\zeta_x\right) - \frac{2}{3}\frac{\partial v}{\partial \eta}\eta_y - \frac{2}{3}\left(\frac{\partial w}{\partial \xi}\xi_z + \frac{\partial w}{\partial \zeta}\zeta_z\right)\right],$$

$$\tau_{yy} = \frac{\mu}{Re}\left[\frac{4}{3}\frac{\partial v}{\partial \eta}\eta_y - \frac{2}{3}\left(\frac{\partial u}{\partial \xi}\xi_x + \frac{\partial u}{\partial \zeta}\zeta_x\right) - \frac{2}{3}\left(\frac{\partial w}{\partial \xi}\xi_z + \frac{\partial w}{\partial \zeta}\zeta_z\right)\right],$$

$$\tau_{zz} = \frac{\mu}{Re}\left[\frac{4}{3}\left(\frac{\partial w}{\partial \xi}\xi_z + \frac{\partial w}{\partial \zeta}\zeta_z\right) - \frac{2}{3}\frac{\partial v}{\partial \eta}\eta_y - \frac{2}{3}\left(\frac{\partial u}{\partial \xi}\xi_x + \frac{\partial u}{\partial \zeta}\zeta_x\right)\right].$$

The viscous shear stresses are:

$$\tau_{xy} = \frac{\mu}{Re}\left[\left(\frac{\partial v}{\partial \xi}\xi_x + \frac{\partial v}{\partial \zeta}\zeta_x\right) + \frac{\partial u}{\partial \eta}\eta_y\right],$$

$$\tau_{xz} = \frac{\mu}{Re}\left[\left(\frac{\partial u}{\partial \xi}\xi_z + \frac{\partial u}{\partial \zeta}\zeta_z\right) + \left(\frac{\partial w}{\partial \xi}\xi_x + \frac{\partial w}{\partial \zeta}\zeta_x\right)\right],$$

$$\tau_{yz} = \frac{\mu}{Re}\left[\left(\frac{\partial v}{\partial \xi}\xi_z + \frac{\partial v}{\partial \zeta}\zeta_z\right) + \frac{\partial w}{\partial \eta}\eta_y\right].$$

The heat fluxes are defined as

$$q_x = -\frac{\mu}{(\kappa-1)M_\infty^2 PrRe}\left(\frac{\partial T}{\partial \xi}\xi_x + \frac{\partial T}{\partial \zeta}\zeta_x\right),$$

$$q_y = -\frac{\mu}{(\kappa-1)M_\infty^2 PrRe}\frac{\partial T}{\partial \eta}\eta_y,$$

$$q_z = -\frac{\mu}{(\kappa-1)M_\infty^2 PrRe}\left(\frac{\partial T}{\partial \xi}\xi_z + \frac{\partial T}{\partial \zeta}\zeta_z\right).$$

We assume the solution to be L_2-periodic in x_2. A perfect gas with a specific-heat ratio of $\kappa = 1.4$ is assumed and the viscosity is calculated according to Sutherland's law

$$\frac{\mu^*}{\mu_\infty^*} = \left(\frac{T^*}{T_\infty^*}\right)^{\frac{3}{2}}\frac{T_\infty^* + 110.4}{T^* + 110.4}$$

with a reference temperature $T^*_\infty = 108$ K and a reference viscosity $\mu^*_\infty = 6.89 \times 10^{-6}$kg/(m s). Dimensional quantities are indicated by an asterisk. Non-dimensionalization is done by

$$u_i = u_i^*/U^*_\infty \ , \qquad \rho = \rho^*/\rho^*_\infty \ , \qquad T = T^*/T^*_\infty \ ,$$
$$p = p^*/(\rho^*_\infty {U^*_\infty}^2) \ , \qquad E = E^*/(\rho^*_\infty {U^*_\infty}^2) \ .$$

u_i denotes the Cartesian velocity component in x_i direction, ρ is the density, p is the pressure and $E = p/(\kappa - 1) + \rho u_i u_i/2$ is the total energy. The reference length is the mean boundary-layer thickness of the experiment $\delta^*_0 = 2.27$mm at the first reference station $E1$. The boundary-layer thickness is measured as the distance from the wall where 99% of the mean free-stream velocity is reached. The time t is non-dimensionalized by the characteristic time scale of the mean incoming boundary layer at the reference station E1, $\delta^*_0/U^*_\infty = 3.69\mu$s.

2.2.1 SGS modelling

For LES, equations (2.1) are filtered at the expense of the appearance of unclosed SGS terms. The resulting equations are solved with respect to the filtered variables $\bar{f} = G * f$, where G is the filter kernel of width Δ and $*$ denotes a convolution operation. Here a brief description of basic SGS model is given, the incompressible formulation is used in order to highlight the general idea. In the traditional approach unclosed terms are rearranged to form the SGS stress tensor $\tau^{SGS}_{ij} = \overline{u_i u_j} - \bar{u}_i \bar{u}_j$. An eddy-viscosity model assumes that

$$\tau^{SGS}_{ij} = 2\nu_T \bar{S}_{ij},$$

when different methods to define the eddy-viscosity ν_T can be used. Here $S_{ij} = \frac{1}{2}(\frac{\partial u_i}{\partial x_j} + \frac{\partial u_j}{\partial x_i})$ is the strain-rate tensor. The classical model of Smagorinsky (1963) constructs ν_T as a product of a length scale and a velocity difference at that scale:

$$\nu_T = C_S \Delta \left(\Delta (2 S_{ij} S_{ij})^{\frac{1}{2}} \right),$$

where C_S is the Smagorinsky constant. The similarity model of Bardina *et al.* (1980) assumes turbulence scale invariance, thus τ^{SGS}_{ij} must be similar to a stress tensor constructed from the resolved velocity field:

$$\tau^{SGS}_{ij} = C_s(\widehat{\bar{u}_i \bar{u}_j} - \hat{\bar{u}}_i \hat{\bar{u}}_j).$$

Here $\hat{}$ denotes a second (test) filter with filter width $k\Delta, (k > 1)$, C_s is a scaling factor (usually about 1). Germano *et al.* (1991) proposed to determine model constants dynamically instead of prescribing or tuning them. The approach again uses the assumption of scale invariance by applying the coefficient measured from the resolved scales to the SGS range. Formally, the dynamic procedure is based on the Germano identity:

$$L_{ij} = T_{ij}^{SGS} - \widehat{\tau_{ij}^{SGS}}$$

where $L_{ij} = \widehat{\bar{u}_i \bar{u}_j} - \hat{\bar{u}}_i \hat{\bar{u}}_j$ is the resolved stress tensor and $T_{ij}^{SGS} = \widehat{\bar{u}_i \bar{u}_j} - \hat{\bar{u}}_i \hat{\bar{u}}_j$ is the SGS stress at the test level. In the monotonically integrated large-eddy simulation (MILES, sometimes also referred as "unresolved DNS" or "no-model") approach τ_{ij}^{SGS} is not modeled explicitly. Instead a numerical dissipation plays the role of SGS dissipation. For a more comprehensive analysis and a discussion of different SGS models the reader is referred to the review of Meneveau & Katz (2000).

In this work the deconvolution SGS model, namely the approximate deconvolution model (ADM) of Stolz *et al.* (2001*a*) is used. A detailed description of ADM can be found in this reference and in Stolz *et al.* (2001*b*). Here, we only summarize the most important facts. With ADM a discrete filter G is explicitly applied along with its approximate inverse, the deconvolution operator $Q_N \approx G^{-1}$. The operator Q_N is applied to the filtered variables $\bar{f}$ in order to approximate the unfiltered variables by $f^\star = Q_N * \bar{f}$. A key feature of ADM is that the flux terms in (2.1) are computed directly using the approximately unfiltered fields $f \approx f^\star$ which are subsequently filtered explicitly with the discrete filter G. To model the transfer of energy to scales which cannot be represented on the computational mesh a relaxation term is added. No *a priori* estimates for model parameters are needed. Inverse relaxation times for density, momentum and energy are determined dynamically. The equations solved have the following form

$$\begin{aligned} &\frac{\partial}{\partial t}\frac{f}{J} + G * \frac{\partial}{\partial \xi_1}\frac{F_E}{J} + G * \frac{\partial}{\partial \xi_2}\frac{G_E}{J} + G * \frac{\partial}{\partial \xi_3}\frac{H_E}{J} = \\ &= G * \frac{\partial}{\partial \xi_1}\frac{F_S}{J} + G * \frac{\partial}{\partial \xi_2}\frac{G_S}{J} + G * \frac{\partial}{\partial \xi_3}\frac{H_S}{J} - \chi(I - Q_N * G) * f \quad , \end{aligned} \tag{2.2}$$

where all fluxes are computed with the approximately deconvolved solution $f^* = Q_N * f$. The relaxation parameter χ is estimated dynamically

(Stolz *et al.*, 2001*a*). For simplicity we will omit the overbar on filtered quantities in the following, implying that all variables actually are filtered variables if not mentioned otherwise.

During the simulations it can occur that at isolated instances small flow regions are marginally resolved. In these cases, the deconvolution applied to the filtered temperature which is required for computing the energy transport term overamplifies numerical errors and can result in negative deconvolved temperatures. Note that ADM is designed to amplify non-resolved scales before the computation of the nonlinear transport. In such cases the deconvolved temperature is substituted by the filtered temperature in the neighborhood of where the event occurred. This approach is known as Landweber projection in regularized-deconvolution procedures when *a priori* bounds on the deconvolved solution are possible (Bertero & Boccacci, 1998). During our simulations these events occurred rarely (about once per 2000 time steps at a few random points near mean-flow separation) so that an adverse effect on the results can be excluded.

2.3 Discretization

For numerical integration, equations (2.2) are discretized on the mesh described above. A 6th-order compact central finite-difference scheme of Lele (1992) is used for discretizing all spatial derivatives at the inner mesh points. The accuracy is decreased to 4th order at the first point off the domain boundary and a one-sided approximation of 3rd order is used at the boundary. Time advancement is done with an explicit low-storage 3rd-order Runge-Kutta scheme (Williamson, 1980). A necessary condition for a stable time integration is that the eigenvalues of the spatially discretized linearized Navier-Stokes equations lie within the stability domain of the Runge-Kutta scheme. This stability criterion is maintained by a dynamic time-step control derived from a scalar model advection-diffusion equation. For a CFL number equal to 0.5 a typical timestep in the compression-corner calculation has a value of about $1 \times 10^{-3}\delta_0/U_\infty$, for a flat-plate calculation this value was about $2.8 \times 10^{-3}\delta_0/U_\infty$. It is well known that linear central finite-difference discretizations are generally not suitable for capturing shocks. However, Stolz *et al.* (2001*a*) have demonstrated that for finite Reynolds number ADM is able to reproduce the filtered-shock solution without local coupling to shock-capturing schemes. It should be emphasized that the

exact filtered shock solution, where the high-wavenumber part of the spectrum has been removed, is slightly oscillatory owing to the Gibbs phenomenon.

2.4 Boundary conditions

Boundary data are imposed as follows. At inflow we prescribe all conservative variables f as function of time, using data from a separate computation. For the compression corner calculation results of a flat plate boundary layer calculation are used. This calculation in turn supplies inflow conditions for the decompression corner. The rescaling and recycling method of Stolz & Adams (2003) is employed for the flat plate simulation, see section 3 for a discussion. Periodic boundary conditions were applied in the spanwise direction. At the outflow a sponge-layer technique is used (Adams, 1998). At the upper truncation plane of the computational domain non-reflecting conditions are imposed. The wall is assumed to be isothermal and no-slip conditions are enforced on the velocity. The wall-temperature distribution is uniform in spanwise direction, along the streamwise direction it is taken from the experiment of Zheltovodov *et al.* (1987), where the wall is supposed to be adiabatic. Since in this experiment the non-dimensional wall temperature on the flat plate has a small difference compared to that of the considered case, it was rescaled linearly. Then the data was smoothed and interpolated onto the computational grid as shown in figure 2.3. Isothermal conditions are preferable over adiabatic conditions since for the experiment an almost constant temperature distribution in time was observed during the measurements.

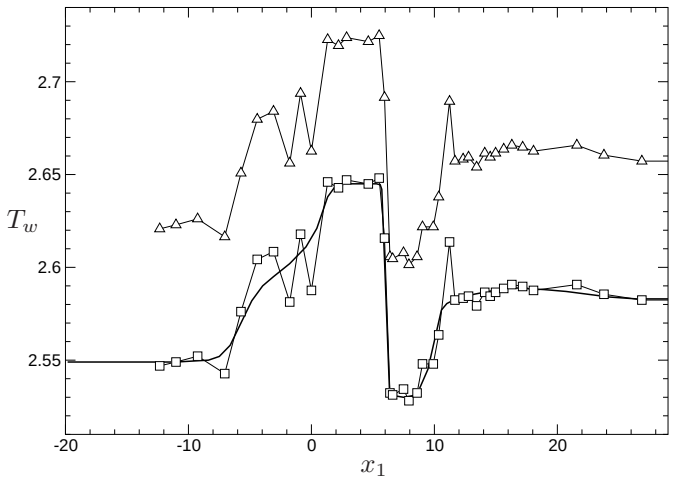

Figure 2.3: Streamwise distribution of the wall temperature. —— *smoothed and interpolated values;* —△— *experimental data (Zheltovodov* et al.*, 1990)* —□— *rescaled to the reference experimental value of* T_w.

Chapter 3

Flat plate boundary layer

A well known problem in the simulation of turbulent boundary layers is that realistic inflow data are needed. Recently Xu & Martin (2004) have reviewed different inflow generation techniques. Following them, the inflow generation techniques can be organized into three categories:

1 spatially evolving boundary layer simulating the full transition process;

2 using data from previous simulations (or data combined with those from experiment);

3 various techniques using an instantaneous downstream flow field (streamwise periodic boundary conditions, extended temporal approach, rescaling and recycling method, etc.).

A brief summary of available simulations can be found in appendix A. A DNS of a spatially evolving turbulent supersonic flat-plate boundary layer is conducted by Rai *et al.* (1995). A developed turbulent boundary layer with a momentum thickness of $Re_\theta \approx 4500$ was obtained by the simulation of laminar-turbulent transition initiated by a blowing/suction strip. This case is close to an experiment by Shutts *et al.* (case 55010501 in Fernholz & Finley (1977)) with $Re_\theta \approx 6000$ and $M_\infty = 2.25$. Later Gatski & Erlebacher (2002) and Pirozzoli *et al.* (2004) repeated this DNS on a finer grid. Their results showed that both the near-wall asymptotic behavior and the log-law exhibit similarities with the incompressible case when the van-Driest velocity transformation is applied. Similarly, the Reynolds stresses also are independent of Mach number when scaled with the mean density ratio as suggested by Morkovin (1962). The results also showed that the total temperature fluctuations were not negligible. LES of this case was performed by Spyropoulos & Blaisdell (1998) using a dynamic Smagorinsky model and by Rizzetta & Visbal (2004), using Smagorinsky, dynamic Smagorinsky and MILES approaches.

Guarini *et al.* (2000) employed a "slow growth" assumption to simulate a turbulent boundary layer at $Re_\theta = 1577$. It is assumed that the boundary layer grows slowly in the streamwise direction so that the turbulence can be treated as approximately homogeneous in this direction.

The slow growth is accounted for by a coordinate transformation and a multiple-scale analysis, resulting in some extra terms in the Navier-Stokes equations. The simulation confirmed the validity of mean flow and turbulence scaling. An extended form of the Reynolds analogy was also found to hold, nevertheless their results invalidate many of the assumptions made in deriving SRA.

A similar technique called extended temporal direct numerical simulation (ETDNS) is used by Maeder *et al.* (2001) to investigate turbulent boundary layers at different Mach numbers of $M_\infty = 3; 4.5; 6$ and $Re_\theta \approx 3000$. Their results showed that compressibility effects on turbulence statistics are small up to a Mach number of about 5. Additionally, the ratio of the Reynolds shear stress to the turbulent kinetic energy is approximately constant in the outer part of the boundary layer. Maeder *et al.* (2001) also confirmed that the total temperature fluctuations are not negligible, and that the streamwise velocity and temperature fluctuations are not perfectly anti-correlated.

A compressible extension of the rescaling and recycling method (RRM) of Lund *et al.* (1998) is used by Yan *et al.* (2002*a*,*b*) for adiabatic- and isothermal-wall boundary layers at $M_\infty = 2.88$ and 4. In this approach the instantaneous flow field is taken from a reference cross-section at a downstream position x_r at every timestep, rescaled according to empirical laws for mean flow and turbulence evolution and reintroduced at the inflow. The essential advantage of this method, which we will call the rescaling-recycling method RRM in the following, is that it allows a better control of the desired turbulent-boundary-layer properties at a certain downstream station and reduces the transient region downstream of inflow required to recover a developed turbulent boundary layer compared with other approaches. Stolz & Adams (2003) proposed another formulation of compressible RRM and determine the validity of the method by the simulations of flat plate boundary layer at $Re_\theta = 4530$ and 10049. Xu & Martin (2004) formulated an alternative technique for rescaling.

For the flat plate the computational domain is rectangular with extents of $16 \times 4 \times 4$ in the streamwise, spanwise and wall-normal directions. The mesh consists of $201 \times 132 \times 101$ grid points (about 2.7 million in total), the step size in physical space is uniform along streamwise and spanwise directions. In wall-normal direction gridpoints were condensed towards the wall. The first point off the wall is located at $x_3^+ = x_3 u_\tau / \nu_w = 2.4$, wall-unit distances in streamwise and spanwise

directions are 45.8 and 17.7. Here the friction velocity $u_\tau = \sqrt{\tau_w/\rho_w}$ and the kinematic viscosity at the wall $\nu_w = \mu_w/\rho_w$ are based on mean flow quantities. The boundary layer is resolved by 58 gridpoints in wall-normal direction, and by 2 points in the viscous sublayer. Such a resolution is found to be sufficient for the considered flow parameters (Stolz & Adams, 2003).

As initial data an instantaneous solution was taken from the previous flat plate simulations of Stolz & Adams (2003) and rescaled to match the required Mach number and domain size. Since in the previous simulation the domain width was only one third of the current, the initial field was composed by repeating this field three times in spanwise direction. The simulation was run long enough, so that a statistically stationary state was reached. Sequentially it was continued for $55.7\delta_0/U_\infty$ characteristic time-scales. Of all conservative variables (density, momentum and total energy) 400 samples were taken at evenly spaced consecutive time increments roughly spaced by $0.14\delta_0/U_\infty$ at the downstream position $x_r = 11.15$. for the estimation of mean and statistical quantities and for inflow preparation. In the following we distinguish between Favre, i.e. density-weighted statistical averages and Reynolds averages. The former is indicated by a double prime $f'' = f - \langle \rho f \rangle / \langle \rho \rangle = f - \{f\}$, the latter by a single prime $f' = f - \langle f \rangle$.

3.1 Instantaneous structures

The instantaneous flow field can be visualized in terms of the density field. Figure 3.1 reveals the existence of organized motions in the outer layer, which is characterized by the occurrence of large-scale intermittently appearing structures. These structures are separated from the surrounding essentially irrotational fluid by sharp interfaces having a three-dimensional character. Unlike the DNS, the LES resolution is not sufficient to show them clearly. The angle of the structures agrees with the values $45 - 60^\circ$ reported by Spina *et al.* (1994). They move downstream at approximately 90% of the freestream velocity. The average spanwise extent of the largest eddies is approximately $1/2\delta$ in the outer layer, and decreases towards the wall.

The near-wall resolution is sufficient to capture fine structures. The existence of elongated streaky structures of alternating high and low speed near the wall is illustrated in figure 3.2 by the wall-normal component of vorticity ω_z. The wall-parallel plane is located at $x_3^+ = 8.5$.

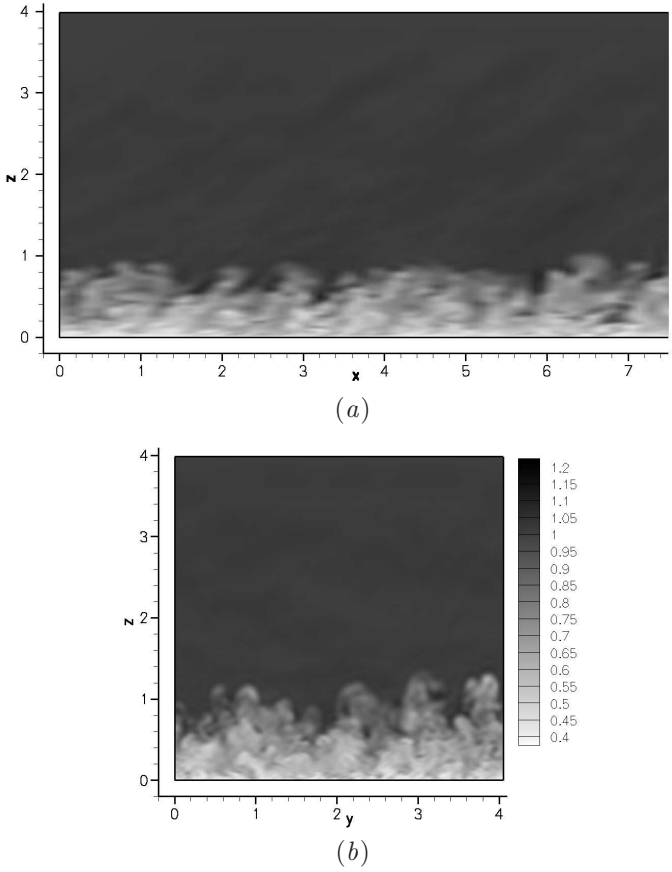

Figure 3.1: Instantaneous density in (a) $x-z$ section and (b) $y-z$ section at $x = x_r$.

The spanwise spacing of the streaks is found to be about 90 to 120 wall units, which is in agreement with Spina *et al.* (1994) and Stolz & Adams (2003). A time series visualization revealed a meandering and lateral motion of the streaky structures by about 100 wall units. The representation of these near-wall structures is important for correct prediction of the skin friction.

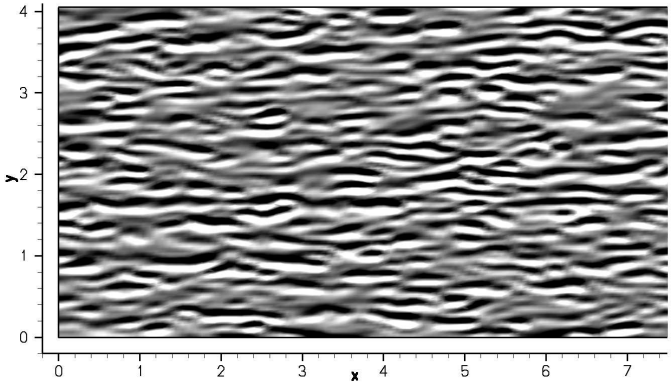

Figure 3.2: Instantaneous $z-$vorticity component ω_z in $x-y$ section.

3.2 Mean flow and statistical analysis

The mean-flow characteristics for the reference section x_r are summarized and compared with the experiment in table 3.1. δ_1 and δ_2 are displacement and momentum thickness, respectively. Re_{δ_2} is the Reynolds number based on the free-stream velocity, momentum thickness and viscosity at the wall. H_{12} is the shape factor. The agreement of δ_0, δ_1, δ_2, H_{12} with the experiment is good. The computed skin-friction coefficient C_f differs more significantly from the experiment with an uncertainty of about $\pm 10\%$. However, the discrepancy is within the limits of experimental-data scatter, as shown in figure 3.3. In this figure several experimental data sets C_f versus Re_{δ_2}, taken from Fernholz & Finley (1977, 1981), are shown along with our computed values and the experimental reference values at station $E1$. An empirical fit of the experimental data is shown by the dashed line, using a von Kármán-Schoenherr incompressible skin-friction formula

$$C_{f_{inc}} = \frac{1}{17.08(\log_{10} Re_{\theta_{inc}})^2 + 25.11 \log_{10} Re_{\theta_{inc}} + 6.012},$$

	δ_0	δ_1	δ_2	Re_{δ_2}	$C_f \times 10^3$	H_{12}
Experiment	1	0.35	0.066	1826	1.79	5.3
Computation	1.001	0.368	0.071	1954	2.05	5.22
Difference	0.1 %	5.3 %	7.0 %	7.0 %	14.5 %	1.5 %

Table 3.1: Summary of mean-flow parameters for the flat-plate boundary layer simulation.

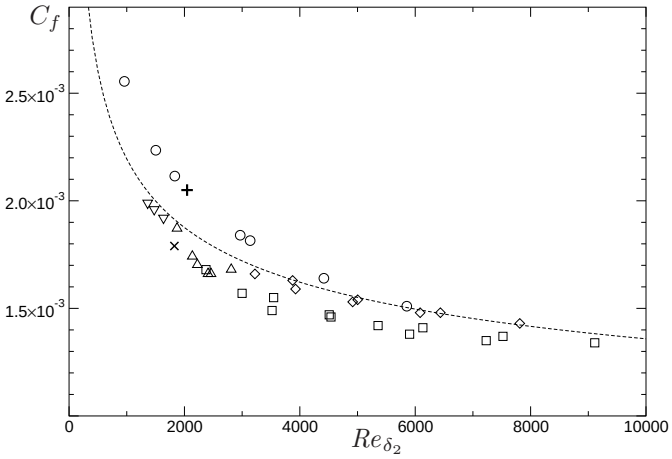

Figure 3.3: Skin-friction coefficient dependency on Reynolds number Re_{δ_2}. + , current LES at x_r position; × , reference experiment; □ , Mabey et al. *CAT7402 ($M_\infty = 3$); ◇ , Mabey* et al. *CAT7402 ($M_\infty = 2.8$); △ , Maier CAT7003 ($M_\infty = 2.9$); ○ , Stalmach CAT5802 ($M_\infty = 2.75$); ▽ , Laderman & Demetriades CAT7702 ($M_\infty = 3$); ---- , prediction by von Kárman-Schönherr skin-friction law with van-Driest-II transformation. Data from Fernholz & Finley (1977, 1981).*

extended to the compressible case as:

$$C_{f_{inc}} = F_C C_f,$$
$$Re_{\theta_{inc}} = F_\theta Re_\theta.$$

The van-Driest-II transformation for coefficients F_C and F_θ

$$\begin{aligned} F_C &= \frac{\frac{\kappa-1}{2} M_\infty^2 r}{\left(\arcsin\alpha + \arcsin\beta\right)^2}, \\ F_\theta &= \frac{\mu_\infty}{\mu_w} \end{aligned}$$

with

$$\begin{aligned} \alpha &= \frac{2A^2 - B}{\sqrt{4A^2 + B^2}}, \\ \beta &= \frac{B}{\sqrt{4A^2 + B^2}}, \\ A &= \sqrt{\frac{\kappa-1}{2} M_\infty^2 r \frac{T_\infty}{T_w}}, \\ B &= \left(1 + \frac{\kappa-1}{2} M_\infty^2 r - \frac{T_w}{T_\infty}\right) \frac{T_\infty}{T_w} \end{aligned}$$

is found to be superior to others by Hopkins & Inouye (1971). Here $r = 0.9$ is the temperature recovery factor. Obviously, the considered case ($Re_{\delta_2} \approx 2000$) is in the region of the rapid change of C_f, where data are much more scattered than at higher Reynolds number ($Re_{\delta_2} > 4000$). The calculated skin friction coefficient lies close to the upper limit of this scatter, the referenced experiment at the lower, but both of them agree well with established data from Fernholz & Finley (1977, 1981) and empirical correlations.

The wall normal distributions of mean Mach number, temperature, velocity, and density are compared with the experimental data in figure 3.4. In the bulk, the computed velocity profiles agree well with the experimental data, minor discrepancies can be observed for the density and temperature profiles. These differences are well within the experimental error margin. The computed van-Driest-transformed velocity profiles, shown in figure 3.5, agree well with the logarithmic law of the wall $U_{VD}^+ = \ln x_3^+ / 0.4 + 5.1$. Wall-law constants are taken for adiabatic walls, since our temperature at the wall is equal to the adiabatic one, this

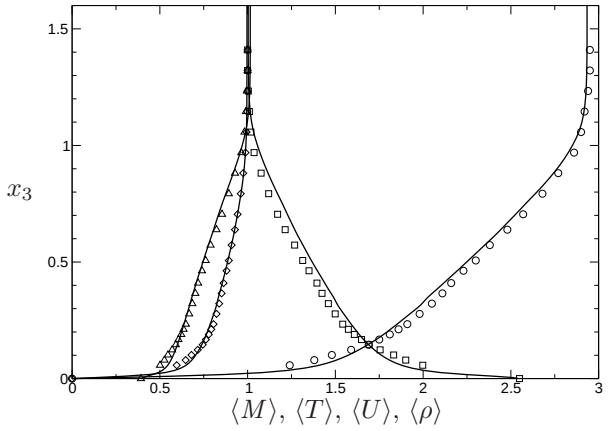

Figure 3.4: Wall-normal distributions of the mean-flow for the incoming flow at station x_r. ——— , current LES; ○ , Mach number; □ , temperature; ◇ , velocity; △ , density. Symbols denote data from the reference experiment.

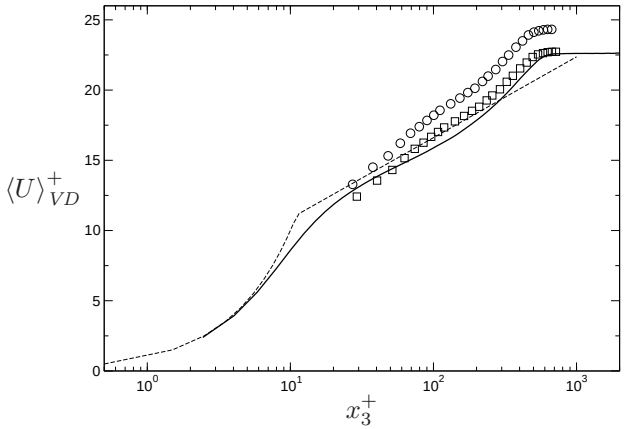

Figure 3.5: The Van-Driest transformed mean-velocity profiles for the incoming flow at station x_r. ○ , reference experiment; ——— , current LES; – – – – , linear and log-law $\ln x_3^+/0.4 + 5.1$; □ , reference experiment with corrected C_f.

comparison can be considered as valid. The velocity U_{VD} is computed as defined by Bradshaw (1977)

$$\langle U \rangle_{VD} = \int_0^{\langle U \rangle} \sqrt{\frac{\langle \rho \rangle}{\langle \rho \rangle_w}} d \langle U \rangle$$

and scaled by the wall-friction velocity $u_\tau = \sqrt{\tau_w / \rho_w}$. The wall-normal coordinate in wall units is $x_3^+ = u_\tau x_3 / \nu_w$. In wall units the experimental data, shown as open circles, differ more significantly from the law of the wall. A better agreement with the law of the wall is obtained if the experimental U_{VD} is scaled with u_τ of the simulation (open squares). This reflects the already mentioned fact of scattered skin friction data (see figure 3.3) and exhibits an influence of the accuracy of the C_f-measurement on the presentation of data in wall units.

As discussed by Zheltovodov & Yakovlev (1986) and Smits & Dussauge (1996) the scaling $\sqrt{\langle \rho \rangle \langle u_1' u_1' \rangle / \tau_w}$ provides an approximate self-similar correlation of experimental data for supersonic flat plate zero pressure gradient adiabatic boundary layers, although the measurements close to the wall are subject to considerable uncertainty. In figure 3.6 upper and lower bounds of an extensive set of experimental data for the Mach number range $M = 1.72 \div 9.4$ are displayed in accordance with the generalization of Zheltovodov & Yakovlev (1986). With respect to inner variables the density-weighted Reynolds-normal-stress and Reynolds-shear-stress profiles should agree with incompressible data in the near wall region (Smits & Dussauge, 1996). This is the case for our simulation data in the region $x_3^+ < 20$ as shown in figure 3.7 by a comparison with incompressible DNS of Spalart (1988).

3.3 Composition of inflow data

The results of the flat plate boundary layer simulation showed a good quality and can be considered as a reliable data for use in subsequent computation. We follow here the approach of Adams (2000) where a separate boundary-layer computation was performed in order to supply inflow boundary conditions. The data from 400 sequential samples described earlier were interpolated by 6th-order splines in the wall-normal direction to the finer grid which is used for the compression corner. Since the time step for the compression-corner simulation can differ from the sampling time intervals these data were interpolated in

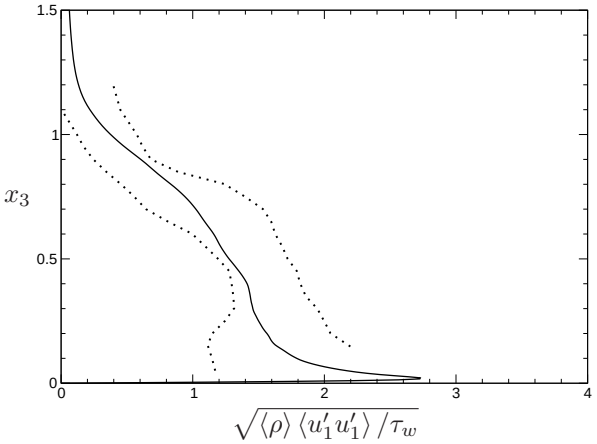

Figure 3.6: Streamwise Reynolds stress. ——— *, current LES;* ····· *, data of Zheltovodov & Yakovlev (1986).*

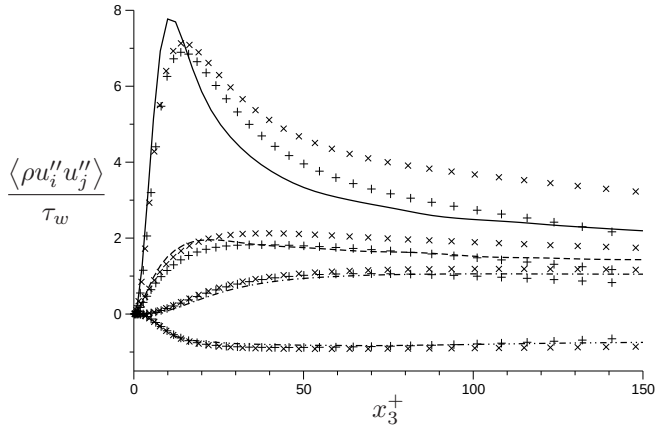

Figure 3.7: Profiles of the density-weighted Reynolds-normal and -shear stresses in wall units. ——— *,* $\frac{\langle\rho u_1'' u_1''\rangle}{\tau_w}$*;* - - - - *,* $\frac{\langle\rho u_2'' u_2''\rangle}{\tau_w}$*;* —·— *,* $\frac{\langle\rho u_3'' u_3''\rangle}{\tau_w}$*;* —··— *,* $\frac{\langle\rho u_1'' u_3''\rangle}{\tau_w}$*;* + *,* $Re_\theta = 670$*;* × *,* $Re_\theta = 1410$*. Symbols denote DNS data of Spalart (1988).*

time by a 3rd-order Neville-Aitken algorithm as described by Adams (2000). The interpolation causes a transient of about $3\delta_0$ and the mean flow parameters at station $E1$ are not exactly the same as at the reference station x_r in flat plate simulation. Nevertheless, the differences are small (Loginov *et al.*, 2006*a*). To allow for a longer time advancement of the ramp computation than the sampling-time period of the inflow data these data are repeated periodically in time. The inflow-data sampling interval T_{samp} was chosen in such a way that a strong scale separation $T_{SSSM} << T_{samp} << T_{LSSM}$ between the characteristic time scales of sampling $T_{samp} = 55.7\delta_0/U_\infty$, small-scale shock motion $T_{SSSM} \sim O(\delta_0/U_\infty)$, and large-scale shock motion $T_{LSSM} = 707\delta_0/U_\infty$ was satisfied. Such a procedure ensures that an artificial time scale imposed by the inflow data does not affect turbulence and LSSM time scales.

Another important issue in the preparation of inflow data is statistical homogeneity in time and over the spanwise direction. The first one is ensured by beginning the sampling after reaching statistical stationarity, it was checked using spanwise averaged quantities. The second issue was not considered previously. Unfortunately, spanwise homogeneity was not monitored during the calculations. The simulation resulted in a small spanwise inhomogeneity in the mean quantities. For example velocity contains disturbances over a range of wave numbers with an amplitude of at most $0.03U_\infty$. Several reasons were investigated in order to explain the appearance of such an inhomogeneity:

- The time evolution of the initial field was not long enough. By construction, the artificial spanwise wavelength of $L_2/3$ was imposed on the initial flow field.

- The sampling period (or number of samples) is insufficient to reach statistical convergence.

- The RRM procedure, which basically connects inflow and downstream sections, may play a role. In particular the streamwise distance x_r may not be sufficient to decorrelate the largest eddies.

In addition to the described flat plate calculation with 400 samples, the simulation was continued with the same sampling parameters. Additional 4×400 samples were collected over a time period of $220\delta_0/U_\infty$. Each of these additionally collected datasets were analyzed separately and exhibited the same statistical properties with very similar spanwise

variation, which is close to the one previously observed. This confirms the statistical stationarity and absence of an initial field influence. The mean properties calculated from the entire set of 2000 samples revealed the same kind of spanwise inhomogeneity. So, the first two reasons can be excluded. Using two-point correlations Stolz & Adams (2003) demonstrate that a streamwise distance of $x_r = 6.7\delta_0$ is sufficient to decorrelate turbulent fluctuations. On the other hand experimental data suggest that the large-scale structures persist for at least 4 boundary-layer thicknesses (and probably much farther) downstream (Spina *et al.*, 1994). In order to clarify this point the domain length was doubled in streamwise direction and the recycling station was set up to $x_r = 27.15$. Large scale turbulent structures can evolve over longer distances. This simulation gave a slight improvement, but did not suppress spanwise inhomogeneity entirely. This fact might indicate that a longer x_r is preferable. A further increase of x_r however, seems to be impractical, since the computational cost of the inflow field computation would approach that of the compression corner computation.

Chapter 4

Compression corner flow

The integration domain of the compression corner computation has the extents $L_1 = 25.9$, $L_2 = 4$, $L_3 \approx 4$, in the streamwise, spanwise, and wall-normal directions, respectively. The streamwise length measured along the surface, the inflow spanwise and wall-normal sizes are the same as in the flat plate calculation described in chapter 3. The computational mesh consists of $701 \times 132 \times 201$ (about 18.6 million in total) points. The spatial resolution of the simulation is matched to that of Stolz *et al.* (2001*a*) in terms of wall units, which was found to be sufficient to reproduce DNS results with good accuracy.

The ramp computation was started from synthetic initial data generated by an inviscid flow field superimposed with a laminar flat-plate boundary layer. After an initial transient the compression corner simulation was continued for 707 characteristic time scales of the incoming boundary layer δ_0/U_∞. This corresponds to about 27 flow-through times of the free stream through the computational domain and is about twice as long as for the earlier DNS of Adams (2000). Owing to the larger sampling time, smoother statistical data have been obtained, and also at least one period of low frequency large-scale shock motion (LSSM) could be captured (see section 4.3). During this time interval the flow field was sampled 1272 times for statistical analysis. Various statistical quantities and time-history data have been saved. This calculation required about 18000 CPU hours on $4 - 6$ CPUs running in parallel on vector-parallel platforms NEC SX-5 and SX-6. For additional details about computational resources and performance please refer to appendix C.

An overview of all relevant flow parameters is given in table 4.1. Additionally, the number of grid points N_i is specified for each coordinate direction $i = 1, 2, 3$. The extents of the computational domain in streamwise direction is L_1, in spanwise direction L_2, and in wall-normal direction at inflow L_3. Measured in wall units of the incoming boundary layer the grid size in the respective coordinate directions is given as $\Delta^+_{x_i}$, where for the wall-normal direction this refers to the distance of the first grid-point off the wall. There are 117 points inside the boundary layer at section 1.

In the following we present data along certain computational-grid

parameter	value	comment
β	25°	
M_∞	2.95	
Re_{δ_0}	63560	
Re_{δ_1}	22120	
Re_θ	4705	using ν_∞
Re_{δ_2}	2045	using ν_w
δ_1	0.37	at section $E1$
δ_2	0.071	at section $E1$
N_1	701	
N_2	132	
N_3	201	
L_1	25.8	along the wall
L_2	4	
L_3	≈ 4	
$\Delta^+_{x_1}$	16 to 34	
$\Delta^+_{x_2}$	17.7	at section $E1$
$\Delta^+_{x_3}$	1.1	first point off the wall at section $E1$

Table 4.1: Simulation parameters.

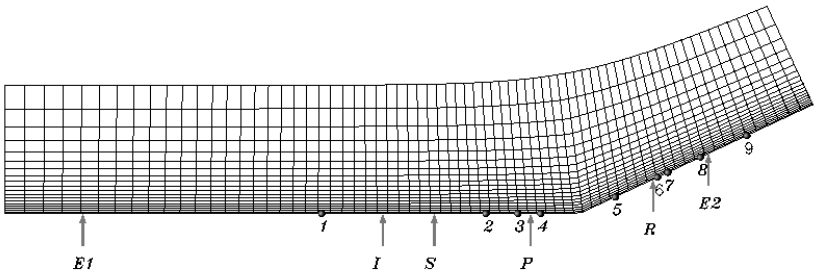

Figure 4.1: Compression corner mesh (each 10th line is shown); for selected reference stations as indicated by arrows and dots, refer to tables 4.2 and 1.1a.

Symbol	x_1	comment
$E1$	-15.4	experimental reference section E1
I	-6.1	incipient interaction
S	-4.5	mean-flow separation
P	-1.5	pressure plateau position
R	2.5	mean-flow reattachment
$E2$	4.4	experimental reference section E2

Table 4.2: Selected downstream stations.

lines $\xi_1 = const.$ For the analysis of the compression-corner flow selected downstream stations will be referred, as indicated in figure 4.1. The relevant sections are labeled with symbols which we refer to in the following. Their positions in terms of the downstream coordinate x_1, along with their particular significance, are summarized in table 4.2. Additional sections $1 - 9$ from higher-Reynolds-number experiment are shown in figure 4.1 by points and are also used for detailed mean flow analysis. Where appropriate, the velocity is represented by its contravariant components, $u_1^c = (u_1\partial\xi_1/\partial x_1 + u_3\partial\xi_1/\partial x_3)/\sqrt{(\partial\xi_1/\partial x_1)^2 + (\partial\xi_1/\partial x_3)^2}$, $u_2^c = u_2$, and $u_3^c = (u_1\partial\xi_3/\partial x_1 + u_3\partial\xi_3/\partial x_3)/\sqrt{(\partial\xi_3/\partial x_1)^2 + (\partial\xi_3/\partial x_3)^2}$. The computational grid is constructed in such a way that the difference between contravariant components and longitudinal components, where the ve-

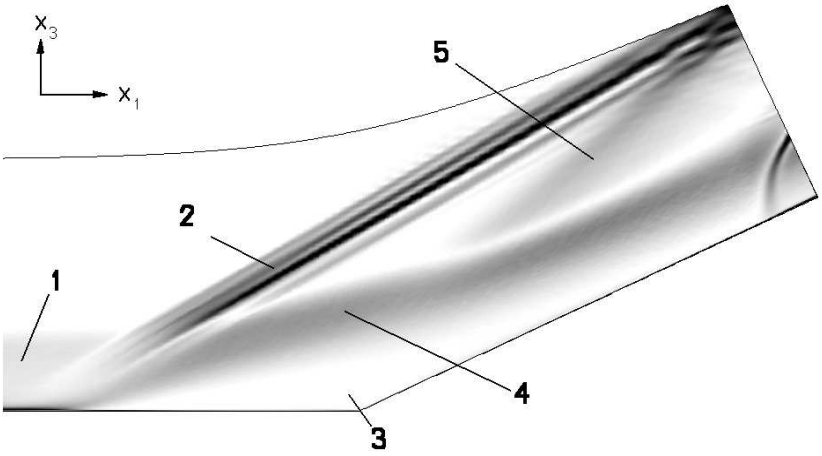

Figure 4.2: Mean density gradient $\|\nabla\rho\|$ averaged in spanwise direction (for legend see text on page 42).

locity is rotated into a Cartesian system aligned with the wall, is small. The contravariant projection, however, removes the ambiguity of the longitudinal projection near the corner.

4.1 Mean flow

For a general impression of the flow in figure 4.2 a Schlieren-imitation (density-gradient magnitude) of the mean flow in the interaction region is shown. A corresponding Schlieren photograph of the reference experiment would require an exposure of about 2.6ms. Note that the flow near the outflow boundary is affected by the sponge outflow treatment where artifacts can be seen, which are, however, not relevant for our analysis. The computed flow recovers the main flow features that were described in section 1. The ramp deflection angle of $\beta = 25°$ at $M_\infty = 2.95$ is large enough for the incoming boundary layer (1) to separate. Where the large near-wall density gradient of the incoming boundary layer detaches from the wall the separation region (3) begins. A detached shear layer (4) contains the reverse flow region (3). Since the Reynolds num-

ber is comparably large, the forward shock (2) penetrates rather deeply into the boundary layer. Near the wall increased turbulent diffusion and finite mean streamline curvature cause the shock foot to spread out so that it is hardly visible in the Schlieren image. LSSM and spanwise shock deformation give rise to apparent additional shock images around the main compression shock. The rear compression shock (5) appears as a converging set of compression waves originating from the reattachment region. Instantaneous data will show, however, that the rearward shock is in fact created by highly unsteady compression waves and shocklets.

Another important finding can be drawn from figure 4.3. The computational-domain boundaries are indicated by thin black lines, crossflow-planes are colored with local mean temperature. A translucent isosurface of mean pressure $\langle p \rangle = 1.2 p_I = 0.1$ represents the mean forward shock. This value is recommended by Hunt & Nixon (1995) for detecting the shock position. Despite the fact that the flow geometry is nominally two-dimensional, the interaction breaks the spanwise translational symmetry. The temperature distribution in a cross-flow plane after the interaction clearly shows a spanwise variation unlike for a cross-flow plane before the interaction. A rake of 10 colored mean streamlines identifies the recirculating flow in the separation region. Furthermore, a non-planar motion in the separation zone and a rotational motion after reattachment are evident. The streamlines originate from midspan position of inflow section at $x_3/\delta_0 = 0.002; 0.004; 0.01; 0.022; 0.026; 0.05; 0.066; 0.16; 0.33; 0.91$ or in wall units $x_3^+ = 1.1; 2.5; 6; 13; 21; 36; 52; 126; 267; 540$.

Two pairs of counterrotating streamwise vortices can be identified in the reattaching shear layer from isosurfaces of contravariant streamwise vorticity ω_1^c. Several identification methods based on point-wise analysis of the velocity gradient tensor as described by Chakraborty *et al.* (2005) are tried. All of them show quite similar results. Since the circulation of the vortices is rather small which makes them hard to extract from background noise, the streamwise mean vorticity was additionally filtered by a top-hat filter on the computational mesh for the purpose of visualization. Positive rotation is indicated by the color "cyan" and negative rotation by "magenta".

These streamwise vortices affect the turbulence structure and the properties of the mean flow significantly (Zheltovodov & Yakovlev, 1986; Floryan, 1991; Lüdeke *et al.*, 2004, e.g.). This is evident if we consider the computational analogue of an experimental oil-flow image in figure 4.4,

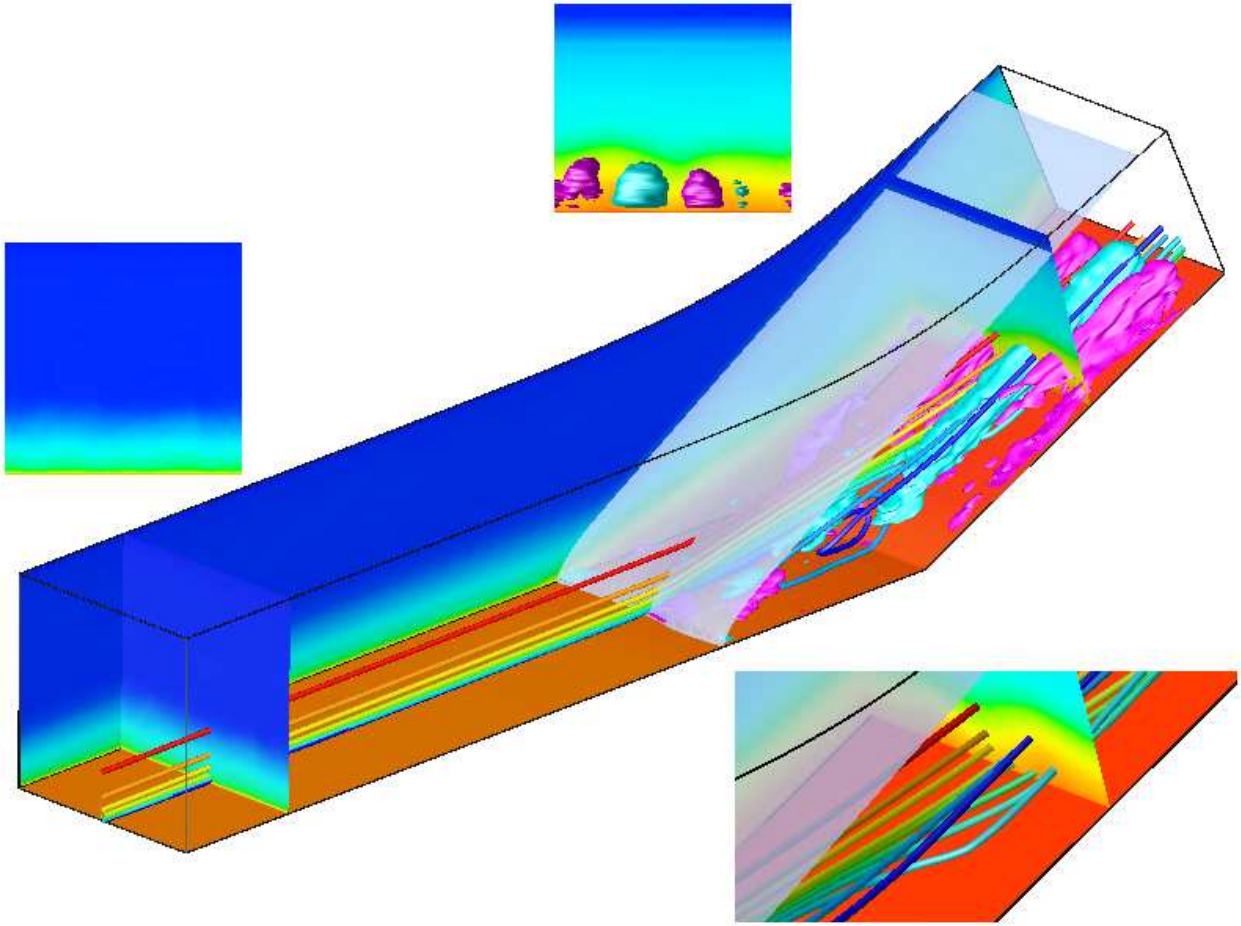

Figure 4.3: Three-dimensional mean flow.

where we show the distribution of the mean skin-friction coefficient. Solid lines represent the contour $C_f = 0$, the left-most line representing separation, the right-most reattachment. For reference, the corner is indicated by a dashed line. The skin-friction coefficient is calculated as follows. The viscous stress tensor $\tau_{ij} = \frac{\mu}{Re}\left(\frac{\partial u_i}{\partial x_j} + \frac{\partial u_j}{\partial x_i} + \frac{2}{3}\frac{\partial u_k}{\partial x_k}\delta_{ij}\right)$ was computed first, then it was projected onto the surface $\tau_{ij}n_j$, and finally the magnitude of the projected vector with appropriate sign is taken. Here $n_j = \{\partial\xi_3/\partial x_1, 0, \partial\xi_3/\partial x_3\}/\sqrt{(\partial\xi_3/\partial x_1)^2 + (\partial\xi_3/\partial x_3)^2}$ is the unit vector, normal to the wall ($\xi_3 = const$ surface). It is evident that although the separation line is curved without significant variations in the spanwise direction, the reattachment line clearly exhibits two pairs of flow convergence and divergence lines. The position of the convergence lines is approximately at $x_2 \approx \delta_0$ and at $x_2 \approx 3\delta_0$, the position of the divergence lines at approximately $x_2 \approx 2\delta_0$ and $x_2 \approx 4\delta_0$. The convergence lines can be attributed to cross-flow uplift and the divergence lines to cross-flow downwash, so that they represent footprints of two-pairs of counterrotating streamwise vortices. Consistent with experimental observations (Floryan, 1991, e.g.) we find that the spanwise width of each vortex pair is about $2\delta_0$. A surface oil-flow visualization obtained in the experiments of Zheltovodov *et al.* (1983); Zheltovodov & Yakovlev (1986) exhibits similar features, for the higher-Reynolds-number experiment the photo of oil-flow visualization is shown in figure 4.5. The characteristic pattern can be associated with a system of steady streamwise vortices. Again the vertical dashed line indicates the position of the ramp corner. The accumulation of oil downstream shows the typical mean-flow reattachment topology in the presence of streamwise vortices (Zheltovodov *et al.*, 1983; Lüdeke *et al.*, 2004) with a sequence of the singular saddle- and node- type points along the reattachment line (see also figure 1.3). Clearly visible are convergence and divergence lines in the reattaching flow, pairs of convergence and divergence lines being spaced by approximately $2\delta_0$. A similar footprint of streamwise vortices is observed on panoramic interferograms when measuring the skin friction in the reference experiment.

The spanwise variation of the mean skin-friction coefficient at the reference stations $E1$, I, S, P, R, and $E2$ is shown in figure 4.6. While C_f varies at station $E1$ in the undisturbed boundary layer by a magnitude of approximately $\pm 0.24 \cdot 10^{-3}$, this variation increases to about $\pm 0.69 \cdot 10^{-3}$ at station $E2$ after reattachment. It is obvious that the spanwise variation of the mean flow should be taken into account when comparing

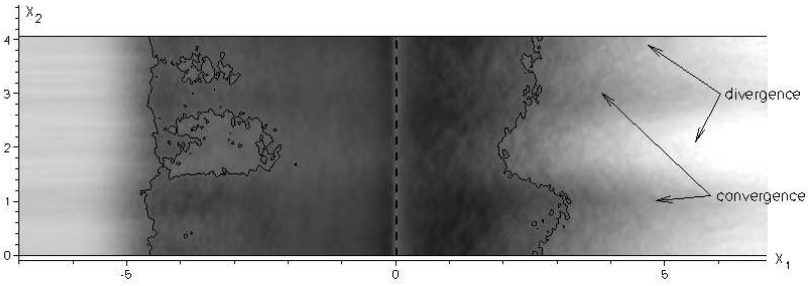

Figure 4.4: Distribution of the mean skin-friction coefficient. ——— *,* $C_f = 0$*;* - - - - *, corner position.*

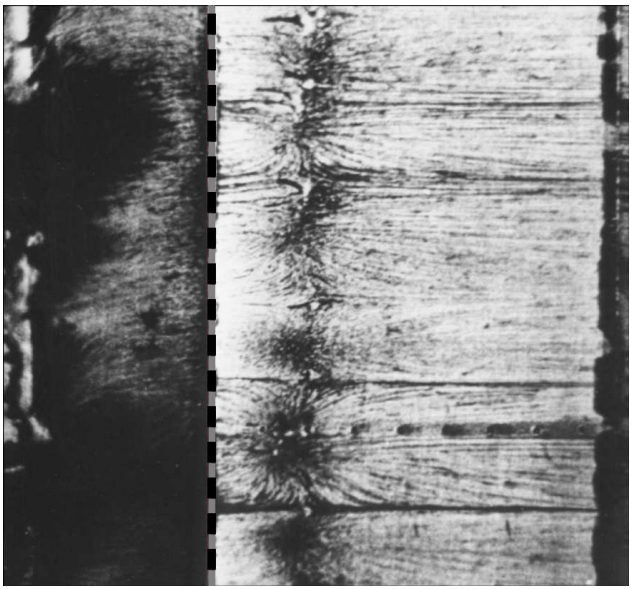

Figure 4.5: Oil-flow visualization pattern from higher-Reynolds-number experiment, the thick dashed vertical line indicates the corner position.

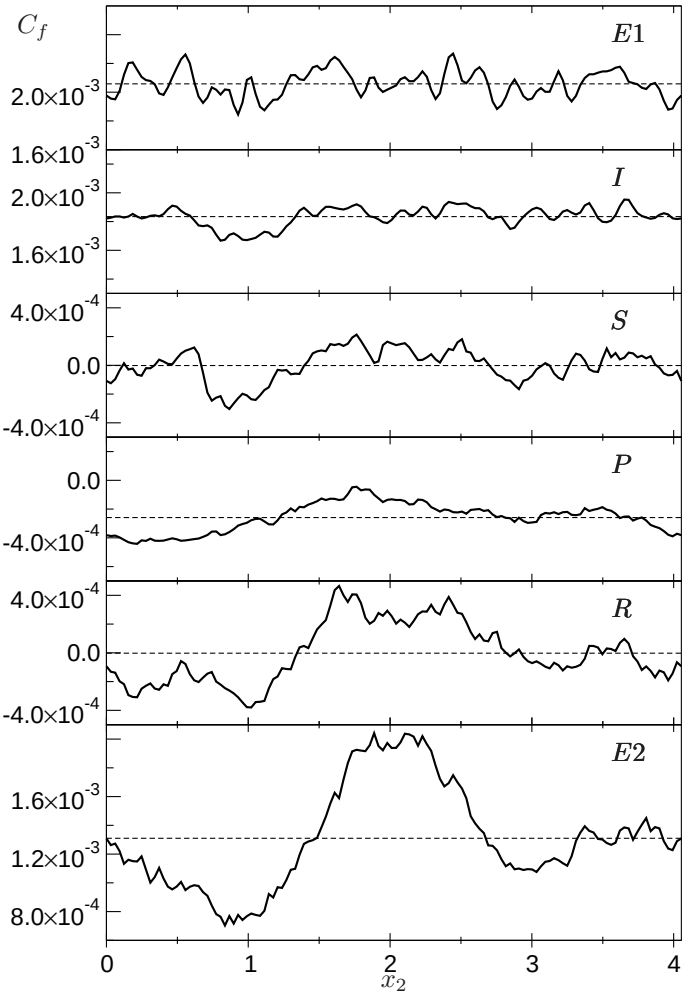

Figure 4.6: Distribution of the mean skin-friction coefficient at the wall in spanwise direction. ——— *, averaged in time;* – – – – *, averaged in time and over spanwise direction.*

computational data with the experiment since experimental data usually are collected only at a single section $x_2 = const$ (usually the model centerline).

To assess the agreement of our computation with the experiment we compare skin-friction coefficient and surface pressure in figure 4.7. The mean skin-friction measurements were done by the Global Interferometry Skin Friction technique (GISF) (Borisov *et al.*, 1993, 1999). The method allowed panoramic skin-friction measurements. Because of poor picture quality only several partially overlapping datasets were generated near the model centerline between convergence-divergence-line pairs, but the exact position, with respect to these is unknown. The computational data averaged in time and in the spanwise direction (thick solid line) are in very good agreement with the experimental data (circles), figure 4.7(a). Deviations of experimental data from computed spanwise averaged values are in between of $\min_{x_2} C_f$ and $\max_{x_2} C_f$ denoted by dotted lines. We recall that in this computation the decompression corner is not considered. Instead, the deflected part of the compression ramp is longer than for the reference experiment and a sponge zone is added at the outflow of the computational domain. Therefore, no agreement of computational and experimental data can be expected near the decompression corner and beyond. The mean-flow separation is located at $x_{1S} = -4.5 \pm 0.25\delta_0$ and mean-flow reattachment occurs at $x_{1R} = 2.5 \pm 0.7\delta_0$. The separation length L_{sep} can be estimated as $7\delta_0$. Separation and reattachment positions are determined by zero spanwise averaged skin-friction are displayed with S and R respectively.

A less strong spanwise variation is observed for the surface pressure, shown in figure 4.7(b) normalized by the surface pressure of the incoming boundary layer value at reference station $E1$. The surface pressure exhibits a pressure plateau with an inflection point P as indicated in the figure. Further downstream, the wall-pressure eventually recovers to the inviscid oblique-shock value shown by dash-dotted line, but the point where this occurs is located farther downstream. For our case, the inviscid value is not recovered before the decompression corner position. Again, a very good agreement between computational and experimental results is found. Here, we can also verify that differences between computation and experiment near the decompression corner are due to the mentioned differences in the length of the deflected part of the ramp and due to the sponge zone. With open squares we also show in figure 4.7(b) surface-pressure data from the higher-Reynolds-number experiment with

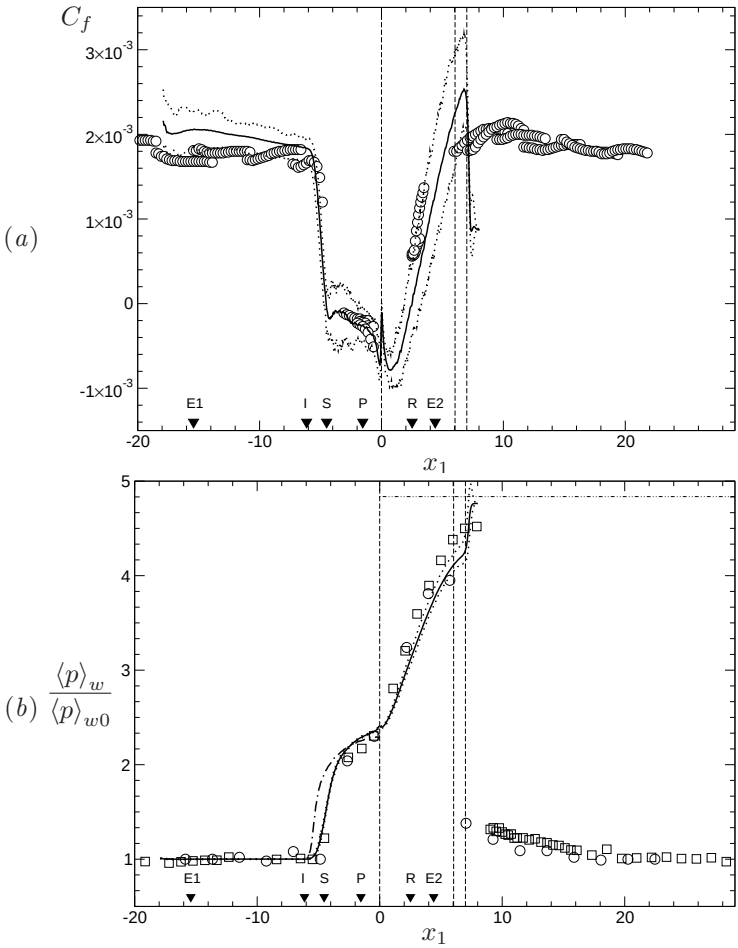

Figure 4.7: Averaged skin-friction coefficient (a) and wall-pressure (b) distributions in the streamwise direction. ○ *, reference experiment;* ——— *, current LES averaged in time and over spanwise direction;* ····· *, current LES averaged in time only,* min *and* max *values over spanwise;* □ *, higher-Reynolds-number experiment;* —·— *, free interaction theory;* —··— *, inviscid solution. The leftmost dashed vertical line indicates the compression-corner position, the middle dashed vertical line the decompression-corner of the experiment and the right-most dashed vertical line the beginning of the sponge-zone at outflow of the computation.*

a longer deflected surface. First, we note that in the considered range the Reynolds number has a negligible effect on the surface pressure. Second, it can be seen that the computational data indeed follow the additional experimental data before they are affected by the outflow sponge zone. By comparison with experimental data the sponge zone invalidates a layer with a length of about δ_0 upstream of outflow.

For an analytic prediction of the separation location in shock-boundary-layer interaction frequently the free-interaction theory for large Reynolds numbers is invoked (Chapman *et al.*, 1957). A result of this theory is an empirical formula for the surface pressure across the interaction region (Erdos & Pallone, 1962)

$$F(s) = (p(s) - p_I)\sqrt{\frac{\sqrt{M_\infty^2 - 1}}{2C_{fI}}},$$

where $p(s)$ and p_I are the wall pressure normalized by the dynamic pressure $q = \frac{1}{2}\rho_\infty U_\infty^2$ as function of the normalized streamwise coordinate

$$s = \frac{x - x_I}{x_S - x_I}.$$

The index I indicates that data are to be taken from the incoming undisturbed boundary layer just before the interaction. Although the free interaction theory predicts a steeper pressure raise and an earlier separation than is observed for experiment and LES, the predicted pressure-plateau value agrees with both.

Figure 4.8 gives an impression of the mean flow evolution. The computational data are shown by thick solid and dotted lines, having the same meaning as in figure 4.7. The black dots correspond to sections $E1$ and $E2$ of the reference experiment, open circles indicate higher-Reynolds-number experimental data at sections $1 - 9$, their streamwise positions are detailed in table 1.1*a*. The incoming undisturbed turbulent boundary-layer profile in section 1 transforms into a profile with weak reverse flow slightly downstream of the separation point (section 2). Further downstream the reverse flow becomes stronger (sections $3 - 5$). At section 6 the boundary layer is reattached while still expressing a momentum deficit in the wake. This reestablished attached boundary layer develops towards an undisturbed profile further downstream. The experimental profiles exhibit only a weak dependence on the Reynolds number

in the considered range (only at sections 1 and 8 data from both experiments are available). Taking into account the spanwise variation of the computed mean velocity experimental and numerical data generally agree well. Excessive negative experimental velocity data at section 5 can be explained by difficulties to measure the reverse flow, also near the line of the zero velocity the accuracy and reliability of the experimental data are reduced. Differences inside the boundary layer at section 2 ($x_3 < \delta_0$) and in the outer flow at section 8 ($x_3 > \delta_0$) may be attributed to difficulties with pitot probes in the highly unsteady regions as pointed out by Dolling (1998). A pitot probe overestimates data in these regions. Also the accuracy of the static pressure measurements is very limited near unsteady shock waves and near separation and reattachment regions.

The spanwise averaged mean flow field is presented in figure 4.9 by the shock wave (thick solid line), by streamlines originating from the inflow section at $x_3/\delta_0 = 0.2; 0.4; 0.6$, the sonic line with $\langle M \rangle = 1$ (dashed line) and the zero-velocity line with $u_1^c = 0$ enveloping the reverse flow (thick dotted line). Generally speaking averaging in homogeneous spanwise direction is not valid in our case since the considered flow is essentially inhomogeneous in spanwise direction. Nevertheless we used this traditional approach in order to present an overall impression of the flow.

4.2 Görtler vortices

The question arises about the origin of streamwise vortices as mentioned in section 1. When a boundary layer develops on a concave wall, streamwise vortices can occur within the boundary layer. A centrifugal force imposed by the curvature of the wall forces fluid particles to be displaced towards the wall. On the other hand the pressure force opposes this centrifugal force to restore the particles to their original position. When the centrifugal force is larger than the pressure force such that the viscosity cannot damp the motion, the flow field is considered to be unstable and small disturbances are likely to be amplified. Görtler (1954) proposed a stability criterion

$$G = \frac{U_\infty \delta_2}{\nu} \sqrt{\frac{\delta_2}{R}} \tag{4.1}$$

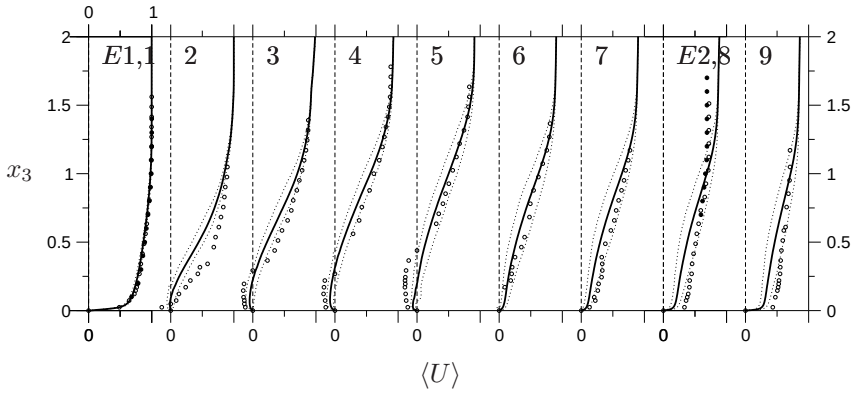

Figure 4.8: Velocity profiles at several downstream positions.

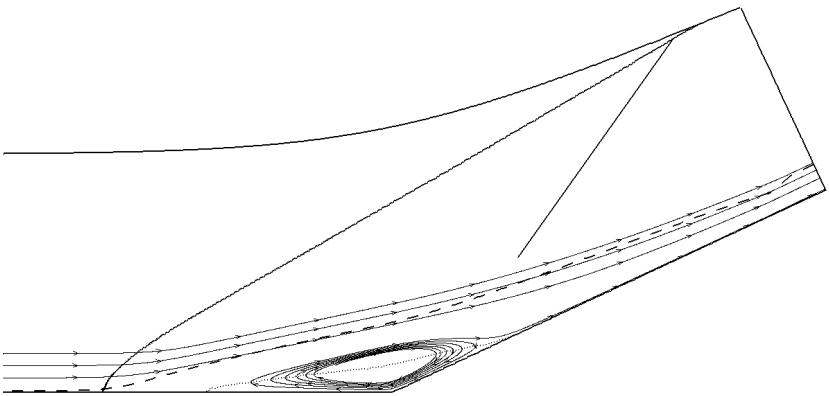

Figure 4.9: Two-dimensional representation of the mean flow. ——— *, shock wave with λ-configuration;* - - - - *, sonic line with* $\langle M \rangle = 1$*;* ····· *, zero-velocity line with* $u_1^c = 0$*.*

for this situation. Here $R = \frac{d^2 z_s}{dx_s^2}\left(1+\left(\frac{dz_s}{dx_s}\right)^2\right)^{-1.5}$ is the curvature radius of the mean-flow streamlines within the boundary layer close to the corner, x_s, z_s are streamline coordinates. Although the Görtler instability, which is inviscid in nature, has been the subject of many investigations, these investigations have been limited mainly to laminar and incompressible flow fields with emphasis on the role of the vortices in the transition process. For a detailed overview of current knowledge of the subject, readers are referred to the reviews by Floryan (1991) and Saric (1994).

If the mean streamline curvature in the separation region or in the reattachment region is larger than the critical value for laminar flow a similar mechanism generating streamwise vortices may be active in the turbulent flow as well. Tani (1962) suggested that criterion (4.1) could be applied to turbulent flows by using the same characteristic length scale, δ_2, and simply replacing the molecular viscosity ν by the eddy viscosity ν_T. If we assume that the eddy viscosity in the outer layer is given by $\nu_T = 0.018 U_\infty$ then the Görtler number for a turbulent boundary layer can be estimated as

$$G_T = \frac{\delta_2}{0.018\delta_1}\sqrt{\frac{\delta_2}{R}}.$$

For an estimation of the Görtler number in the considered flow, the mean velocity field averaged in spanwise direction was used to plot the streamlines. For the streamlines shown in figure 4.9 the Görtler number distribution in streamwise direction is shown in figure 4.10. Numerous streamlines through the boundary layer were checked, all of them show a similar trend. Near the separation region all streamlines within the boundary layer have $G_T > 1$ which is well above the critical value of about 0.6 for laminar flows (Görtler, 1954). G_T is slightly smaller in the reattachment region but still near the critical value. Another criterion for the significance of streamline curvature is given by the curvature parameter δ_0/R which was used for the investigation of subsonic turbulent flows (Floryan, 1991). From our simulation we find $\delta_0/R > 0.1$ near the separation line and $\delta_0/R \geq 0.03$ near reattachment. Again these values are much larger than the critical value $\delta/R = 0.01$, for which the first appearance of streamwise vortices was found. These two indicators, Görtler number and curvature parameter, point to a Görtler-like mechanism being responsible for the observed streamwise vortices.

For a statistically two-dimensional turbulent flow there is no reason

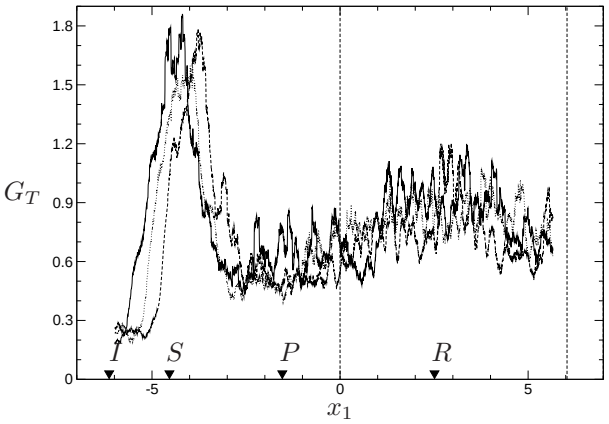

Figure 4.10: Görtler number distribution in streamwise direction. ——— *, for streamline at* $x_3 = 0.2$*;* ····· *, for streamline at* $x_3 = 0.4$*;* – – – – *, for streamline at* $x_3 = 0.6$*; Vertical lines have the same meaning as in figure 4.7.*

why the observed streamwise vortices should remain steady at a fixed spanwise position. A hypothesis about the existence of instantaneous streamwise vortices was suggested by several researchers. Steady or very low frequency spanwise variations within the incoming boundary layer or model imperfections can result in fixing the spanwise location of these vortices, as was observed by Lüdeke *et al.* (2004) and pointed out by Floryan (1991). As described in section 3 the incoming boundary layer is not ideally two dimensional in the mean. It contains steady disturbances over a range of wave numbers. These steady disturbances can act as a seed similarly to experimental-model imperfections and probably fix the vortex locations. The streamwise curvature imposed by streamlines acts as a filter, allowing amplification of certain wave numbers and suppressing the others in accordance with the Görtler criterion.

LES of Comte & David (1996) indirectly supports this selection mechanism. Inflow conditions for this simulation were composed of a mean velocity profile calculated using a $k - \epsilon$ model and white noise with an amplitude of $2 \times 10^{-3} U_\infty$ superimposed onto three components at each time-step. Thus the broadband range of spanwise wavelengths was imposed onto the incoming boundary layer. Such a procedure results in

streamwise vortices with estimated wavelength of about $0.75\delta_0$ found in the instantaneous and in the mean flow. This result is not quite in accordance with the current simulation, it is worthy to note that the flow field of Comte & David (1996) cannot be considered as fully a turbulent one due to the low Reynolds number of $Re_{\delta_1} = 280$.

4.3 Shock wave system behavior

An impression of the instantaneous shock-wave structure can be obtained from a computed Schlieren-type visualization in figure 4.11. This figure is similar to figure 4.2, the flow snap-shot is taken at a time instant, however, and corresponds roughly to an experimental spark shadowgraph. The figure legend refers to the same events as shown in figure 4.2. The spanwise variation of the shock position causes some smearing of the shock position in the interaction region after averaging in the spanwise direction. Clearly visible are compression waves (5) above the separated shear layer (4) and the rearward stem of the λ-shock which originates from the reattachment region. Also the general shape of the forward shock appears to have changed slightly. A similar observation can be made for experimental visualizations at two different time instants for the higher-Reynolds-number experiment (Zheltovodov *et al.*, 1983), shown in figures 4.11(c) and (d).

An animation of a time-series of shock visualizations for our computation is available under the URL `http://www.aer.mw.tum.de/gallery/grad_rho.avi` which clearly shows the unsteady motion of the shock system and the shedding of compression waves behind the forward shock. We find in our simulations a small-scale shock motion, as reported by Andreopoulos & Muck (1987) and Adams (2000), along with a LSSM, as reported by Dolling & Murphy (1983). We also observe that the rearward shock is highly unsteady and becomes invisible at irregular time intervals. The compression waves, indicated as 5 in figure 4.11, travel downstream with a speed of about $0.1U_\infty$ to $0.4U_\infty$.

4.3.1 Unsteady motion

A series of instantaneous snapshots with a diamond marker in the field is shown in figure 4.12. Initially at $t = 95$ (subfigure a) the shock is located slightly downstream of the marker, then it moves upstream until

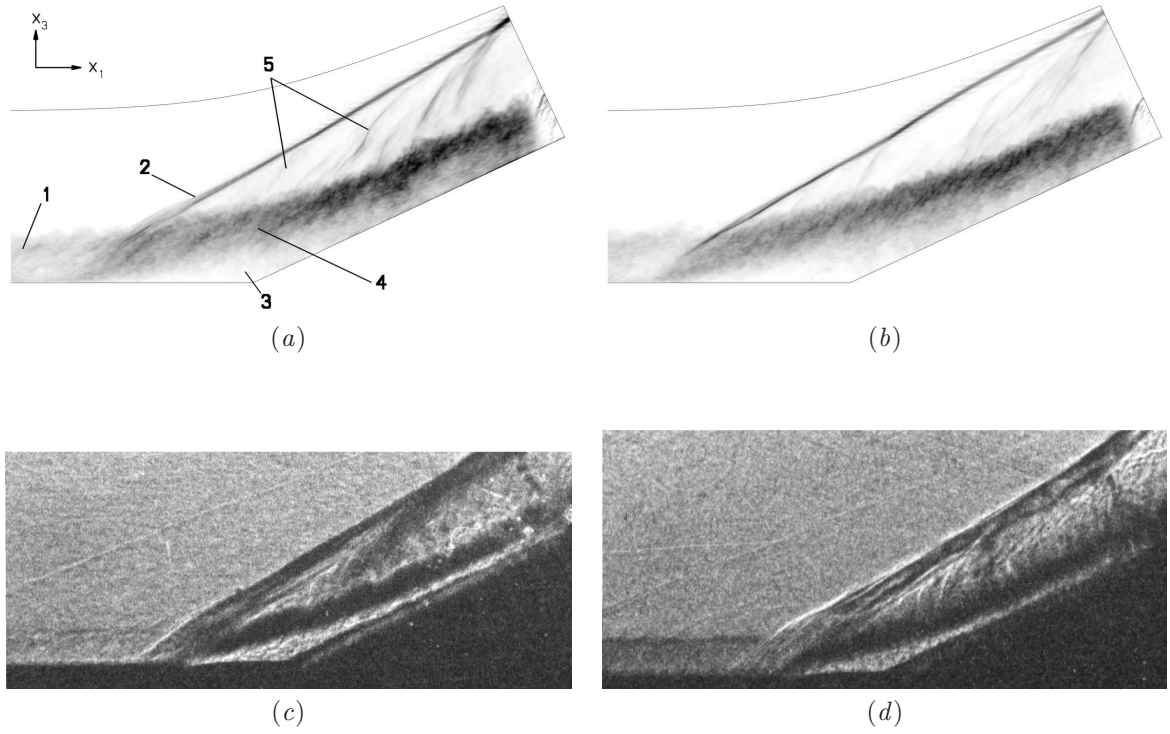

Figure 4.11: Schlieren-type visualization at two time instants: simulation, computed as density gradient $\|\nabla\rho\|$ averaged in spanwise direction (a, b); higher Reynolds number experiment (c, d). Computational and experimental time instants are not related to each other, legend is the same as in figure 4.2.

it reaches its maximum upstream position at $t \approx 500$ (subfigure f). Finally the shock wave roughly recovers its initial position at $t = 691$ (subfigure h).

For an analysis of the shock motion Dolling & Or (1985) recorded the time evolution of wall-pressure signals to identify the shock-foot location. A direct comparison is possible if we apply a similar analysis to our computational data. Time-histories of wall pressure normalized by the mean value at station I are shown in figure 4.13 at six different downstream positions. Sensors were placed at the centerline of the domain, their streamwise positions are shown in figure 4.12(a) as a–f and corresponding to:

(a) within the undisturbed boundary layer at station I,

(b) near the beginning of the interaction where the mean pressure starts to rise above the value in the incoming boundary layer $\langle p \rangle = 1.1 \langle p \rangle_I$ at position $x_1 = -5$ (see figure 4.7b),

(c) maximum pressure fluctuation position at $x_1 = -4.5$ (refer to figure 4.14),

(d) inside the separation region at station P,

(e) near the reattachment line at station R,

(f) downstream of the separation at the experimental station $E2$.

The arrows and dashed lines indicate the respective time-averaged pressure values. Within the insets in each figure the normalized probability-density function (PDF) for the respective pressure signal is shown. For reference also a Gaussian PDF is indicated by a dashed curve. Evidently the PDF distribution is essentially Gaussian within the incoming boundary layer, figure 4.13(a), and within the separation region, figure 4.13(d). An off-center peak in the PDF at the beginning of the interaction (figure 4.13b) indicates that the shock wave does not simply oscillate around its mean position, but that larger excursions have higher probability. By the appearance of a PDF peak at negative pressure values near the onset of the interaction the motion of the forward shock front manifests itself in the pressure fluctuations. The PDF also shows that the forward shock intermittently crosses the sensor position, pre-shock pressure values being more likely found than post-shock values. This finding agrees with the observations of Dolling & Or (1985). The streamwise length of the

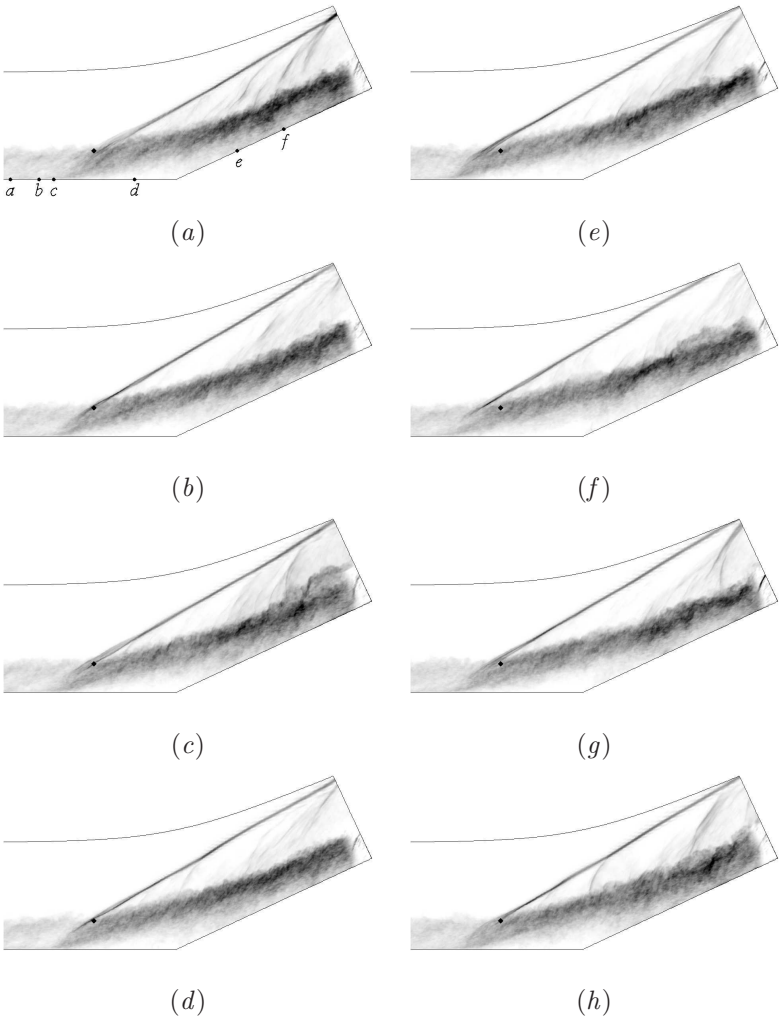

Figure 4.12: A series of instantaneous Schlieren-type visualizations. The time in subfigures (a) – (h) corresponds to $t = 95; 180; 265; 351; 436; 518; 623; 691$.

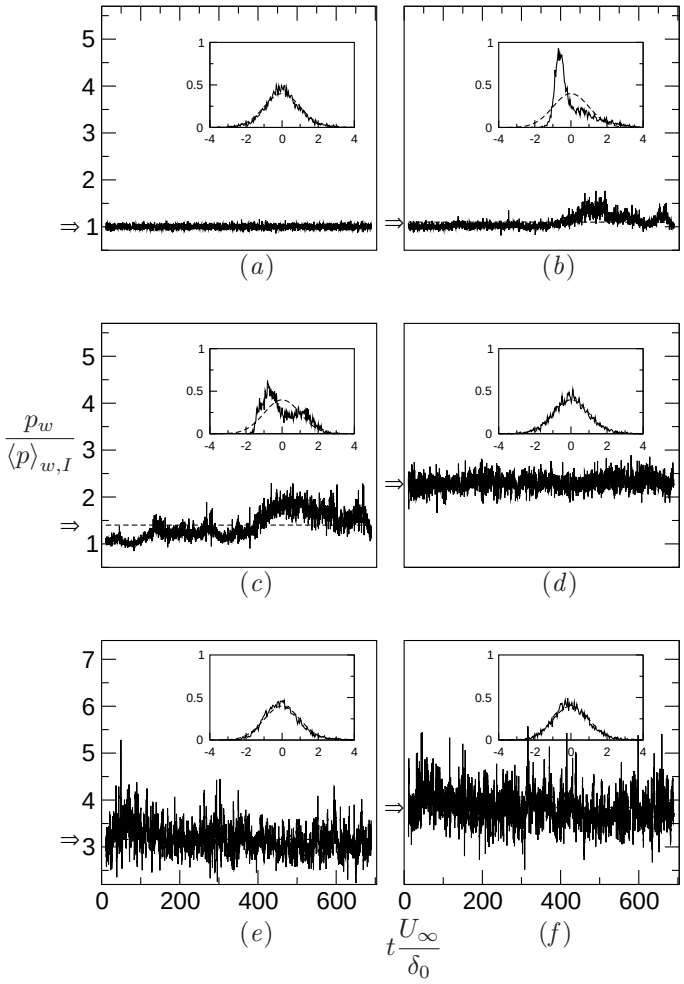

Figure 4.13: Wall pressure history and probability distributions at six different wall positions, (a) at I within the incoming boundary layer, (b) near the beginning of the interaction region, (c) near the location of maximum pressure fluctuations (refer to figure 4.14), (d) at P inside the separation region, (e) at R near reattachment, (f) at E2 downstream of reattachment.

forward-shock excursion can be estimated as $1.16\delta_0$. Further evidence of LSSM can be found at the next sensor position, figure 4.13(c). Initially, the observed pressure is below its average value (the shock wave is downstream of the sensor position). Subsequently, the shock moves upstream, and the pressure value increases beyond its average value at about $400\delta_0/U_\infty$. At the end of the observation time interval the pressure roughly recovers its initial value. Given a limited observation time interval a LSSM time scale cannot be deduced quantitatively. For this purpose, the simulation should cover several cycles of shock motion. Since such a requirement would multiply the computational cost by at least a factor of two it is impractical for us.

We find a PDF with a single off-center peak at the beginning of the interaction and a double-peaked PDF within the interaction region. This reflects the highly intermittent shock motion which has been observed in earlier experiments (Dolling & Murphy, 1983; Dolling & Or, 1985). Inside of the separation zone, figure 4.13(d) and further downstream, figure 4.13(e), the PDF distributions resume a Gaussian shape. The qualitative difference of the pressure signal in the intermittent region near the beginning of the interaction, figure 4.13(b), which is dominated by the separation shock motion, and the one near reattachment, figure 4.13(e), which is affected by the unsteady rearward stem of the λ-shock suggests that the motion of the rearward stem is not related to the motion of the foreward stem.

As was mentioned in section 1, while several studies (e.g. Andreopoulos & Muck, 1987; Adams, 2000) indicate that the small-scale shock motion is driven by turbulent bursting events in the incoming boundary layer, there is currently no theory available which explains LSSM (Dolling, 1998, 2001). It should be mentioned that we can exclude that LSSM in our simulation was driven by the periodically repeated inflow data since the time-scales of LSSM and data repetition differ by about one order of magnitude.

Dolling & Murphy (1983) found a characteristic shape of the standard-deviation distribution of the wall-pressure fluctuations across the interaction, figure 4.14(b). Normalized by the local mean wall pressure our computational results (figure 4.14a) agree quantitatively with the experimental results of Dolling & Murphy (1983), although for these results the Reynolds numbers are one to two orders of magnitude larger. Since no Reynolds-number independent scaling of the interaction-region extent is known, $\sigma(p_w)$ at locations corresponding to respective interac-

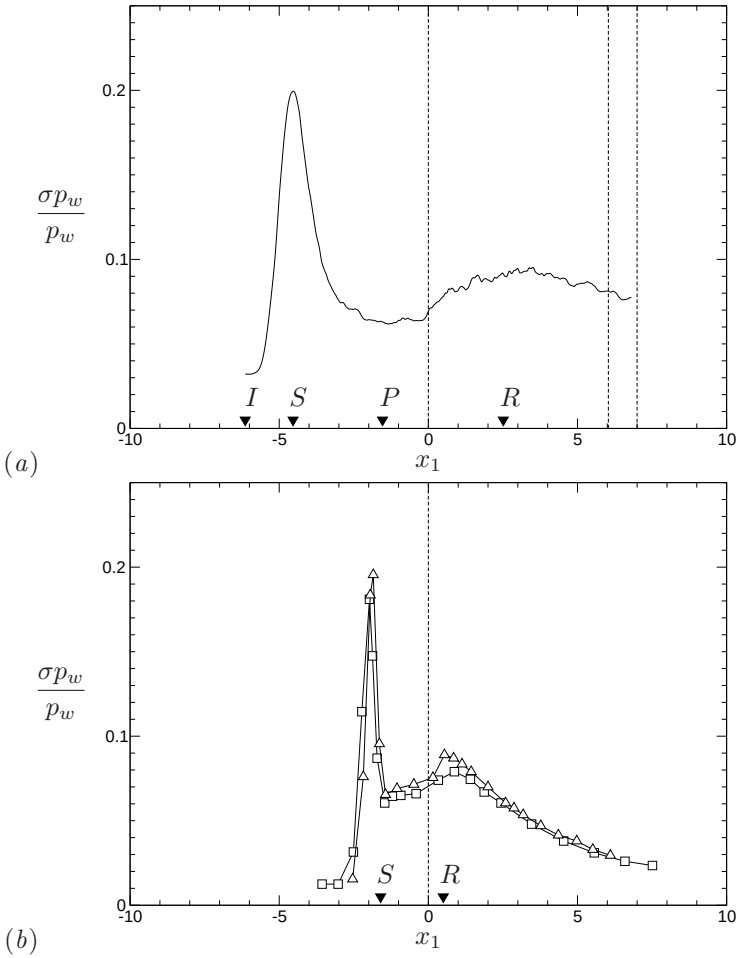

Figure 4.14: Standard deviation of wall pressure fluctuation (a) computation and (b) experiment of Dolling & Murphy (1983). —□— , $Re_{\delta_0} = 780000$; —△— , $Re_{\delta_0} = 1400000$. *Vertical lines have the same meaning as in figure 4.7.*

tion events, such as separation location S, pressure-plateau location P and reattachment location R have to be compared. A global maximum at about 20% of the local mean wall pressure is observed for the LES in the separation region at $x_1 \approx -4.5\delta_0$ which corresponds to the mean separation position S, figure 4.14(a). The maximum value agrees well with the experimental data of Dolling & Murphy (1983) at larger Reynolds number. Note that Dolling & Murphy (1983) find the peak location slightly upstream of their measured separation point. The reason may be that the separation location was identified visually from kerosene-lampblack streak pattern, whereas for the computation $C_f = 0$ could be identified directly. As discussed before, the observed large variance of the pressure fluctuations is a consequence of the shock-foot motion. Characteristic for the standard-deviation distribution is a second peak which can be found near the reattachment position. Its value is at about 9% of the local mean wall pressure for both, computation and experiment. Three-dimensionality of the field indeed affects unsteady loads as well. In spanwise direction the peak value varies in the range of $0.186 - 0.21$. Unfortunately, no clear dependence of the curve shape can be found if different spanwise positions with respect to the vortex core are considered.

The intermittency factor is defined by Dolling & Or (1985) as

$$\lambda = \frac{time[p_w > (\langle p \rangle_{wI} + 3\sigma(p_{wI}))]}{totaltime}$$

and represents the fraction of the time that p_w is above the maximum pressure of the undisturbed flow at station I. The streamwise distribution is shown in figure 4.15. The curve resembles the Gaussian probability distribution, found to be universal for separated flows (Dolling & Or, 1985). The mean flow separation point S corresponds to a high intermittency value of $\lambda = 0.88$.

The flow unsteadiness rises a question about the averaging time period necessary for obtaining converged statistical data. The sensitivity of flow properties with respect to the averaging period is illustrated in figure 4.16, where examples of the time-averaged wall pressure distributions were obtained using described instantaneous data. The averaging periods correspond to $\Delta t = 53.6; 107.2; 214.4$. The pressure in the intermittent region and the reattached flow are affected the most by the unsteady motion, while the plateau value remains constant. The plateau region seems to be independent of the shock unsteadiness, and to exist in

the instantaneous flow also. This partially explains the success of free-interaction theory. A similar analysis is performed by Dolling (1998) using ensemble-averaging of the wall pressure taken instantaneously for different shock wave positions.

4.3.2 Shocklets

An instantaneous representation of the flow is shown in figure 4.17. The slices are colored with the instantaneous density, the isosurface of the pressure with $p = 0.1$ represents the shock wave, the horizontal black line crosses the isosurface at the mean incoming boundary layer thickness for reference purposes. The eight gray lines on the shock surface show the spanwise positions, where data were analyzed. The large scale turbulent structures perturb the shock foot, causing a spanwise wrinkling. It can be observed that the perturbations propagate along the shock to the outer flow and are damped as they move outwards.

Behind the separation shock compression waves exist. They are represented by isosurfaces of the density gradient colored by red in figure 4.17. Some of these compression waves originate from the reattachment region forming the second stem of the λ-configuration. Others are located above the separated shear layer. Obviously, they have a three-dimensional shape with a wave front directed primarily in the streamwise direction. A detailed view of this time instant is given in figure 4.18, where density gradients are shown in several spanwise planes (see also figure 4.12(h) for a spanwise averaged picture) The waves belonging to the λ-configuration generally persist over a longer spanwise length. A separation shock corrugation is observed where it intersects with shocklets.

It is found that waves travelling at larger speed are truly shocklets. Their speed is of the same order of magnitude as the convection velocity of the largest eddies in the detached shear layer (4) so that the ambient-flow speed is supersonic relative to these eddies. For verification of the shocklet character of the stronger compression waves, we have confirmed that the change of the flow state across the shocklets satisfies the Rankine-Hugoniot conditions (Lee *et al.*, 1991) relative to the ambient flow behind the separation shock. The shocklet Mach number, defined as the ratio of ambient-flow velocity relative to the shocklet and sound speed, varies between 1.23 and 2.2. The stronger shocklets with larger Mach numbers have lower absolute velocity and belong to the unsteady

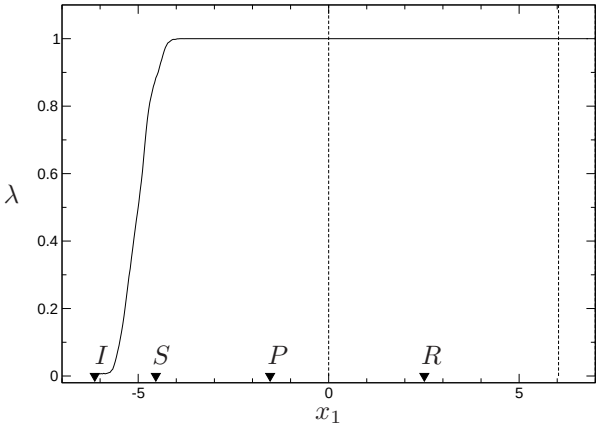

Figure 4.15: Intermittency distribution. Vertical lines have the same meaning as in figure 4.7.

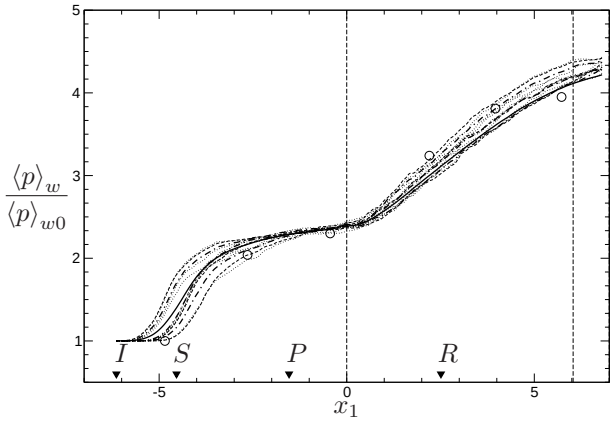

Figure 4.16: Mean pressure dependency on the averaging time. ∘ , reference experiment; ——— , current LES averaged in time and over spanwise direction; ····· , LES averaged over $\Delta t = 53.6$; – – – – , LES averaged over $\Delta t = 107.2$; —·— , LES averaged over $\Delta t = 214.4$; Vertical lines have the same meaning as in figure 4.7.

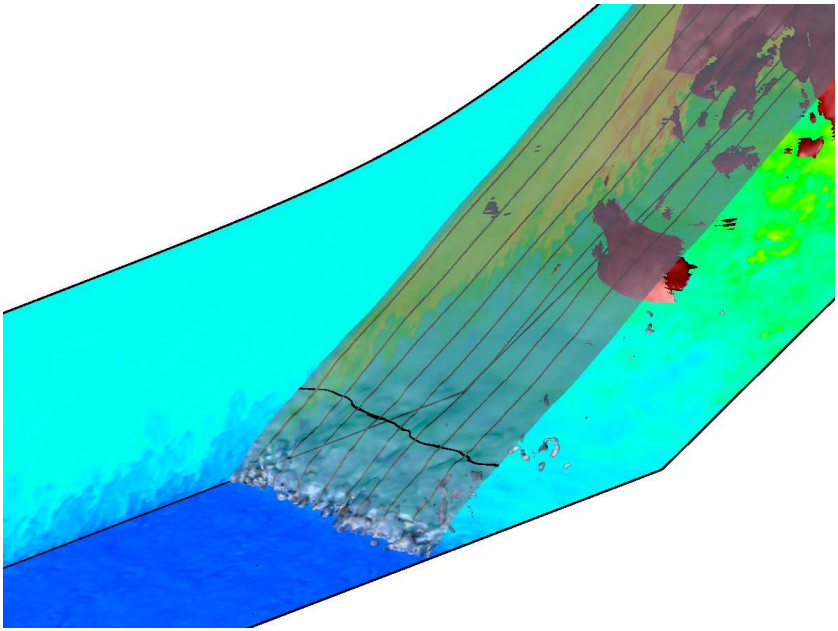

Figure 4.17: Three-dimensional flow field at $t = 691$.

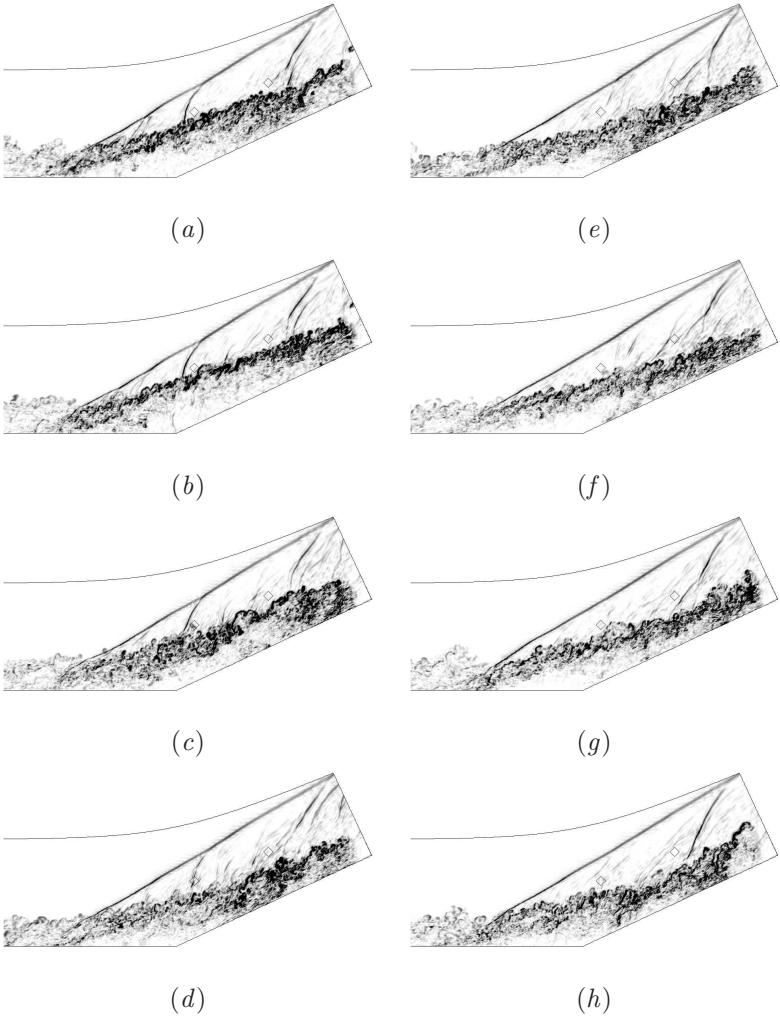

Figure 4.18: Instantaneous density gradient $\|\nabla\rho\|$ in several spanwise sections with $t = 691$. The spanwise position in subfigures (a) – (h) corresponds to $x_2 = 0.6; 1.1; 1.5; 2.0; 2.4; 2.9; 3.4; 3.8$, also shown by lines on the shock in figure 4.17.

second stem of the λ-shock.

We believe that the presence of travelling compression waves and shocklets in the wake of the compression shock explains the high level of turbulent fluctuations in the external flow between the separation shock and the detached shear layer which was observed earlier in experiments by hot-wire measurements (Zheltovodov & Yakovlev, 1986). The observed phenomenon provides evidence for an additional mechanism which enhances the level of turbulent fluctuations in this flow region along with direct interaction of shock and turbulence (Anyiwo & Bushnell, 1982; Andreopoulos *et al.*, 2000). By the method of diagrams of Kovasznay (1953) it was shown by Zheltovodov & Yakovlev (1986) that the acoustic mode is prevalent in this region which is consistent with the existence of weak shocklets.

4.4 Turbulence enhancement

One of the most significant effects of shock-turbulence interaction is that turbulent fluctuations increase and turbulent length scales decrease when passing through sufficiently strong shocks. For a comprehensive summary on the current knowledge the reader is referred to Andreopoulos *et al.* (2000). For the case considered here, the amplification of turbulent fluctuations is evident from figure 4.19. Profiles of root-mean-square (RMS) values of the mass-flux $\langle (\rho U)'^2 \rangle^{1/2}$, density $\langle \rho'^2 \rangle^{1/2}$, and velocity $\langle U'^2 \rangle^{1/2}$ fluctuations (top to bottom) are shown at several downstream sections as given in table 1.1. All quantities are normalized by the incoming free-stream quantities. The solid line denotes the time and spanwise averaged value, the spanwise variation is indicated by dotted lines. Thin horizontal lines correspond to the location of zero mean velocity, which bounds the reverse flow region. The outer maxima which can be observed in sections $2-9$ originate from unsteady shock motion as described in section 4.3. The maxima between $x_3 = 0.75\delta_0$ and $x_3 = 1.25\delta_0$ are located within the detached shear layer. (i.e. inflection point in the velocity profile) and thus exhibit high level of fluctuations. The velocity fluctuations in the first section show the typical near-wall peak. Further downstream this peak remains but its fluctuation level is smaller than that of the detached shear layer. While in the outer flow fluctuations are small at section 1, they grow by interaction with the shock wave (sections $5-9$, $x_3 \approx 2.25$) up to values of larger than $0.1\rho_\infty$ for the density and about $0.01U_\infty$ for the velocity fluctuations. As mentioned

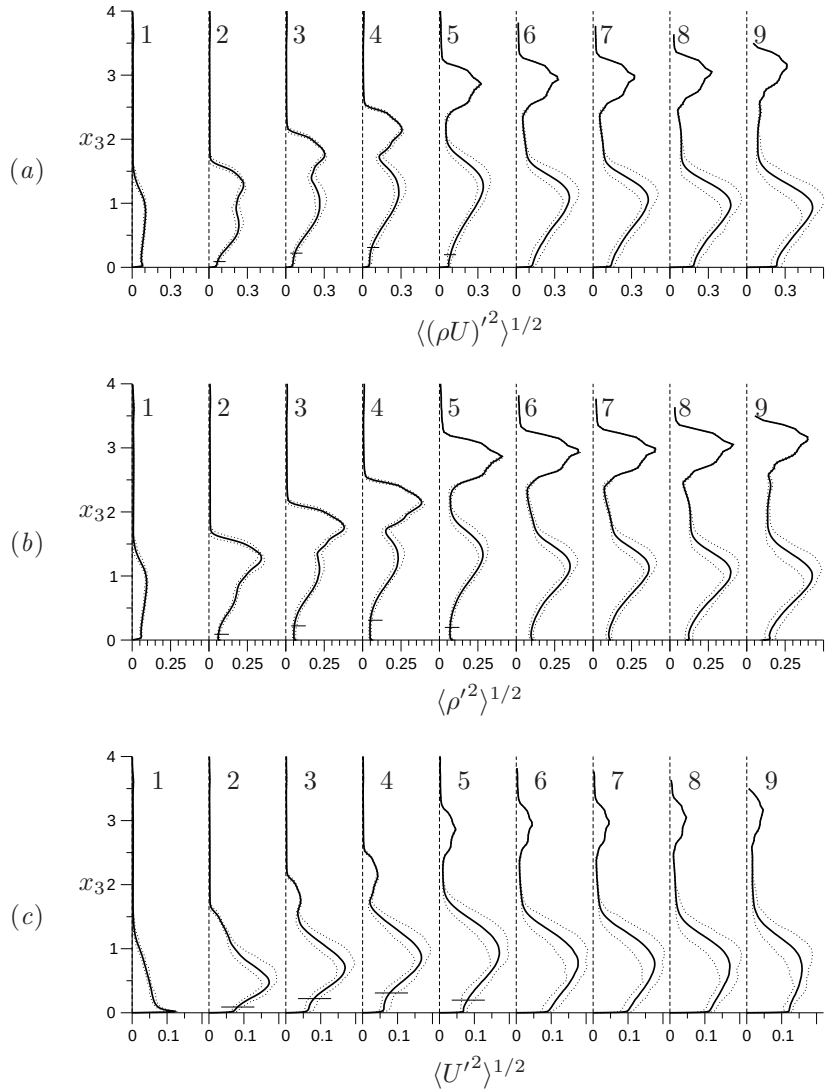

Figure 4.19: Downstream evolution of mass-flux (a), density (b) and velocity (c) fluctuations. Positions are detailed in table 1.1.

before, aside from direct interaction with the shock wave, downstream travelling shocklets contribute additionally to this increase.

We compare data from RMS fluctuations with the reference experiment at positions $E1$ and $E2$ in figure 4.20. Since the measurement technique does not cover the entire frequency range of fluctuations, it is more reliable to use relative changes of the RMS values where data of the undisturbed boundary layer serve as reference. We try to resemble the experimental procedure by normalizing our computational data with the respective maxima in the first section $E1$. Fluctuations of momentum and density are amplified by about a factor of 4 across the interaction, which agrees well with previous observations (Smits & Muck, 1987; Adams, 2000). The simulation shows larger amplifications than the experiment for all quantities near the local maxima in $0.7\delta_0 < x_3 < 1\delta_0$ at position $E2$, and for the density fluctuations in the external flow $x_3/\delta_0 > 1.5$. Given that the measurement error is at best between 15% and 20% the agreement between computational and experimental data nonetheless can be considered as satisfactory. Near-wall maxima of the RMS distributions are not captured by the experiment due to the lack of near-wall resolution.

The Reynolds normal stress $\tau_{11} = \left\langle \rho u_1^{c\prime\prime} u_1^{c\prime\prime} \right\rangle$, the Reynolds shear stress $\tau_{13} = \left\langle \rho u_1^{c\prime\prime} u_3^{c\prime\prime} \right\rangle$ and the structure parameter $-\tau_{13}/\tau_{ii}$ are shown using their contravariant representation in figures 4.21(a), 4.21(b) and 4.21(c), respectively. The Reynolds-normal-stress maximum is located near the wall in the incoming flow, shifts to the detached shear layer and diminishes at the last station. The amplification ratio of about 8 and the quantitative evolution are in agreement with those reported by Smits & Muck (1987) for a compression ramp with $\beta = 25^\circ$ at $M_\infty = 2.79$ and $Re_{\delta 0} = 1570000$. A direct comparison is not possible due to the large difference in Reynolds number. The Reynolds-shear-stress maxima (figure 4.21b) are amplified by a factor of about 28, which is larger than that reported by Smits & Muck (1987). It was noted by Adams (2000) that τ_{13} is very sensitive to the experimental probe adjustment and the transformation of the computational data into the contravariant representation (see also 4.22b). The spanwise variation reaches about $\pm 50\%$ in the calculation, while it was claimed that three-dimensional effects are small in the experiments of Smits & Muck (1987).

Figures 4.21(a, b) and 4.22 indicate that Reynolds normal and shear stresses behave differently so that the turbulence structure changes. Anisotropy can be measured by the structure parameter, in fig-

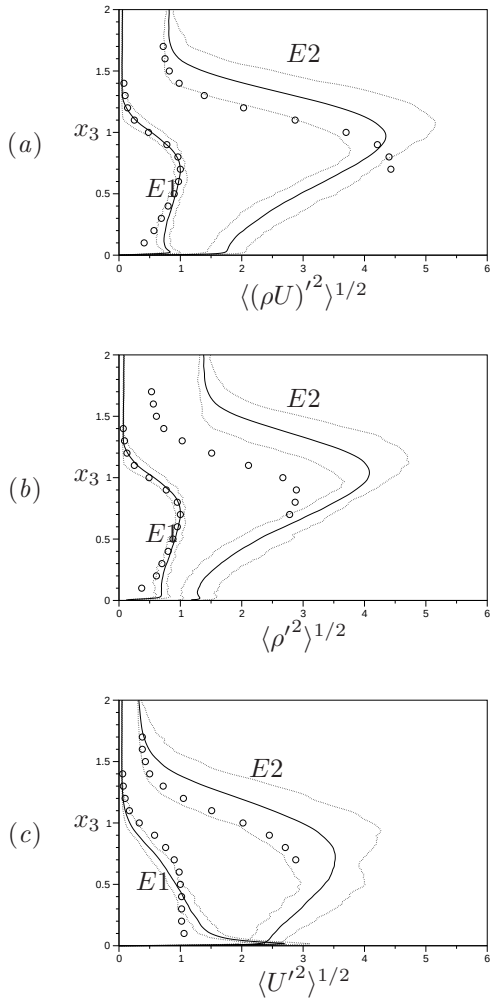

Figure 4.20: Amplification of RMS of momentum (a), density (b) and velocity fluctuations (c) between position $E1$ and position $E2$. ∘ , reference experiment; ——— , current LES averaged in time and over spanwise direction; ····· , current LES averaged in time only, minimum and maximum values over the spanwise direction.

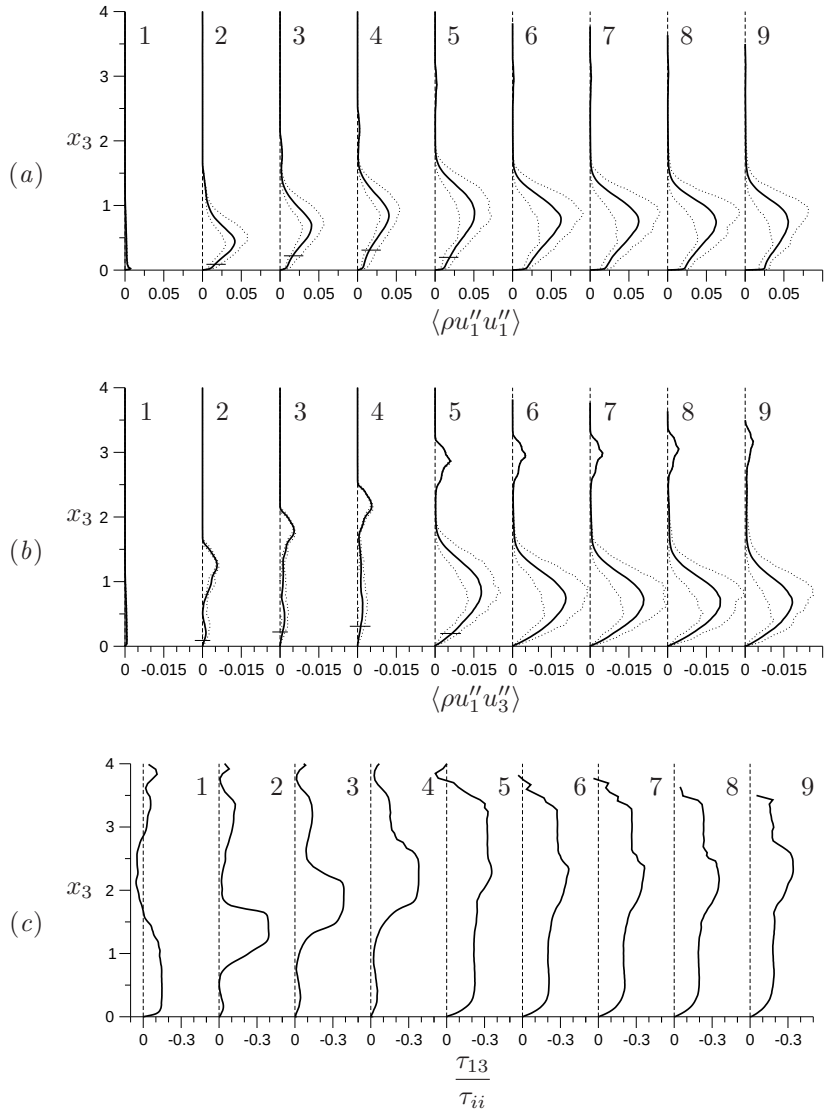

Figure 4.21: Reynolds normal stress $\tau_{11} = \langle \rho u_1^{c\prime\prime} u_1^{c\prime\prime} \rangle$ (a), the Reynolds shear stress $\tau_{13} = \langle \rho u_1^{c\prime\prime} u_3^{c\prime\prime} \rangle$ (b) and the structure parameter $-\tau_{13}/\tau_{ii}$ (c) in several downstream positions.

ure 4.21(c). Its value between 0.13 and 0.15 in the incoming boundary layer agrees well with data reported by Adams (2000) and with incompressible boundary layers (Smits & Dussauge, 1996). Through the interaction it decreases inside the separation zone and then increases again up to the value of ≈ 0.2 in the region after reattachment. Further downstream values tend to decrease towards their magnitude before the interaction. Particularly large values can be observed in the detached shear layer.

4.5 Relaminarization effects

As already mentioned in section 1 the reverse flow exhibits indications of relaminarization inside the separation zone. Zheltovodov (1979) found that a favorable pressure gradient acting on the reverse flow between reattachment and separation line and a decrease of the local Reynolds number can lead to a transformation of the reverse-flow velocity profiles from a shape which is typical for turbulent near-wall jets to a shape which is typical for laminar ones. RANS calculations for a 90° step with a $k-\omega$ turbulence model also revealed indications of this kind of transformation and a decrease of the eddy viscosity in the reverse flow ahead of a 90° step (Borisov *et al.*, 1996). Bedarev *et al.* (1998) have demonstrated that it is possible to predict relaminarization trends in the separation regions for forward-facing steps and compression ramps through an *ad hoc* modification of ω. These computations indicate the importance to model this phenomenon for a better prediction of surface pressure, skin-friction, and heat transfer in the separation region. A comparison of RANS calculations with experimental data at $M_\infty = 3$ and a wide range of deflection angles of $\beta = 8°, 25°, 45°$ and 90° was performed by Borisov *et al.* (1999).

The reverse flow inside the separation zone can be considered as a near wall jet (Zheltovodov, 1979) and we use this fact to analyse effects of inverse transition. The mean velocity profiles for the separated region are plotted in figure 4.23. The reverse velocity is normalized by its maximum value $U_{\max}$, the wall-normal coordinate is normalized by $l_{\frac{1}{2}}$ where the mean velocity is half of its maximum value. In such variables a turbulent near-wall jet has a universal profile indicated by the thick solid line, the dashed line denotes a laminar profile (Vulis & Kashkarov, 1965, p. 262). The higher-Reynolds-number experimental data at sections 3,4 and 5 are shown in the figure 4.23(a), computational results at corresponding

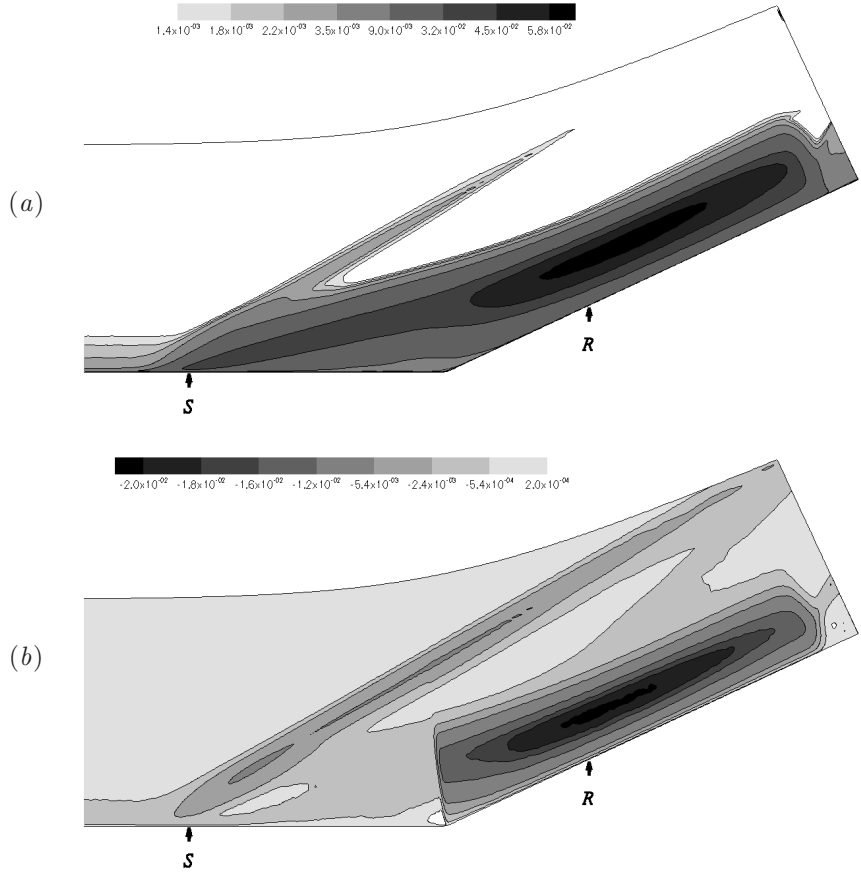

Figure 4.22: Reynolds normal stress $\tau_{11} = \left\langle \rho u_1^{c\prime\prime} u_1^{c\prime\prime} \right\rangle$ *(a), the Reynolds shear stress* $\tau_{13} = \left\langle \rho u_1^{c\prime\prime} u_3^{c\prime\prime} \right\rangle$ *(b) isolevels.*

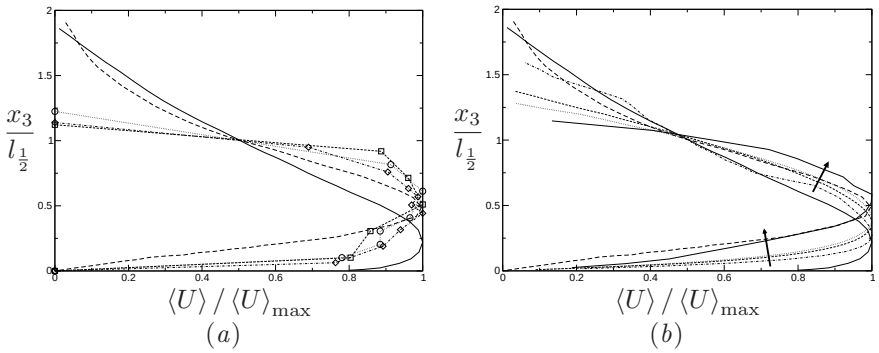

Figure 4.23: Mean velocity in the reverse flow plotted in wall jet variables: higher-Reynolds-number experiment (a) and current simulation (b). ——— *, turbulent near wall jet;* - - - - *, laminar near wall jet;* ○ *, section 3;* □ *, section 4;* ◇ *, section 5;* ——— *, section 2;* ····· *, section 3;* – – – – *, section 4;* —·— *, section 5.*

streamwise positions are shown in the figure 4.23(b). It can be seen that the experimental data scatter around the laminar jet profile. The simulation exhibits a clear tendency of a transformation from turbulent to laminar jet profiles. This agrees with the experimental findings of Zheltovodov (1979) for a forward-facing 90° step.

Based on an analysis of mean-flow and turbulence measurements for a backward-facing step, Adams & Johnston (1988) found that a process similar to an inverse transition can appear also in subsonic turbulent separation. Following their suggestion we show the evolution of mean flow profiles scaled in outer units, figure 4.24(a) and in wall units, figure 4.24(b). For reference, a $\frac{U}{U_{\max}} = \left(\frac{x_3}{\delta_{\max}}\right)^{1/7}$ law and a log-law $U^+_{VD} = \ln x_3^+ / 0.4 + 5.1$ are shown additionally, where the boundary-layer thickness $\delta_{\max}$ here is defined as wall-normal distance of the point of maximum reverse velocity. An evolution away from the turbulent shape is evident.

The variation of maximum negative velocity in the reverse flow $U_{\max}$ is shown in figure 4.25. From reattachment R to separation S the reverse flow accelerates strongly by the favorable (negative) pressure gradient

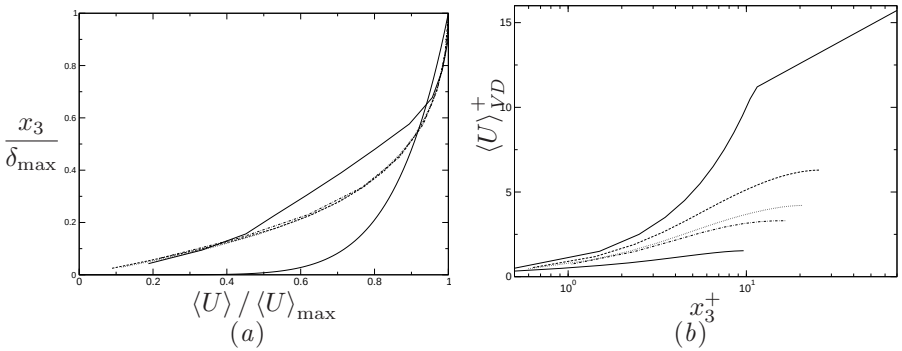

Figure 4.24: Mean velocity in the reverse flow plotted in outer boundary layer scaling (a) and inner scaling (b). ——— *, section 2;* ····· *, section 3;* – – – – *, section 4;* —·— *, section 5.* ▬▬▬ *, power-law* $\langle U \rangle / \langle U \rangle_{\max} = (x_3/\delta_{\max})^{1/7}$ *and log-law* $\ln x_3^+ / 0.4 + 5.1$.

up to the corner position. From these data the acceleration parameter $\frac{\nu}{U_{\max}^2} \frac{dU_{\max}}{dx}$, which is commonly used to assess the relaminarization conditions can be estimated between 10^{-4} and 4×10^{-4} which is in the same range as reported by Adams & Johnston (1988). It is two orders of magnitude larger then the relaminarization limit of 3.0×10^{-6} (Adams & Johnston, 1988). This fact supports the possibility of relaminarization which is also in agreement with the decrease of velocity fluctuations along the line of maximum negative velocity, figure 4.25. After the corner the reverse flow slows down and the near-wall-jet mean-velocity profile assumes a laminar shape. A slight increase of velocity fluctuations can be attributed to approaching the highly unsteady region near separation S.

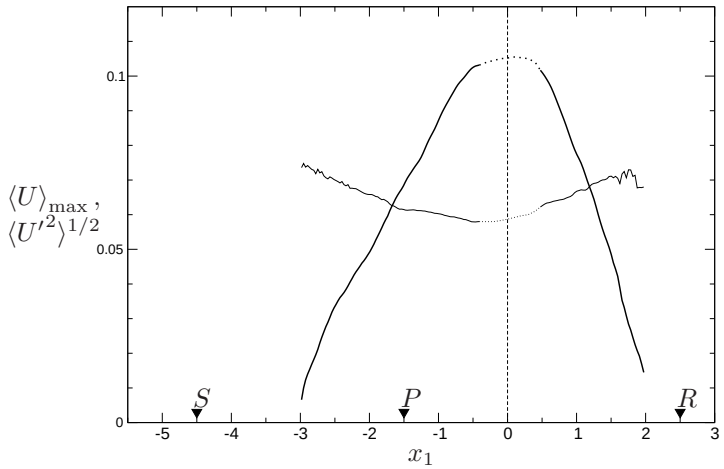

Figure 4.25: Maximum reverse velocity distribution and RMS of velocity fluctuations inside reverse flow. ——— , $\langle U \rangle_{\max}$; ——— , $\langle U'^2 \rangle^{1/2}$ *along* $U_{\max}$. *The region around the corner where data were not analyzed is indicated by dotted line.*

Chapter 5

Compression-decompression corner

So far we have considered a turbulent boundary layer influenced by the shock wave, as the only perturbation imposed. In many practical configurations, however, more than one perturbation event may occur sequentially. For instance, in the compression-decompression corner (see figure 1.1*c*) a rapid compression by the shock wave is followed by an expansion fan. Considering them together allows to investigate the effect of successive perturbations on the turbulent boundary layer. We follow the experimental approach and results are discussed for a full configuration, keeping in mind that two separate simulations on different domains were performed as described in section 2.1.

The domain of the second simulation, considering the decompression corner only, has the extent $L_1 = 14.4$ in the streamwise, $L_2 = 4$ in the spanwise direction, and in the wall-normal direction L_3 varies from 3.6 at inflow to 7.6. The computational mesh consists of $401 \times 132 \times 201$ (about 10.6 million in total) points. The rather big domain height made it possible to avoid an influence of the upper boundary condition on the flow field near the triple point of the λ-configuration. As explained in section 2.1 the inflow section of the decompression-corner domain is exactly matched to a cross-section of the compression-corner domain. In this section the instantaneous field of all conservative variables was saved 5033 times during a period of $259\delta_0/U_\infty$ of the compression-corner simulation. The experimental section $E2$ belongs to both domains, furthermore a short overlapping region of length $x_1 \approx 2\delta_0$ exists, allowing for a cross-checking of the results. The decompression corner results may suffer from inflow-data interpolation. Differences between compression-corner and decompression-corner data in the overlapping region are expected to be small due to very fine time slices, spaced by $\Delta t \approx 0.05\delta_0/U_\infty$, and avoiding spatial interpolation. It should be noted however, that an exact match of the results is not possible, since the explicit filter utilized in ADM depends on the grid, which is different for the two simulations. On the other hand the compression corner simulation does not take into account the effect of the decompression corner, which was substituted by an outflow sponge-layer condition. The estimated upstream distance affected by the decompression corner is about δ_0 (see

section 4.1, figure 4.7), which is not considered when analyzing data in the entire configuration.

Numerical method and boundary conditions are essentially the same as used in the compression corner simulation as described in section 2. Minor modifications of the boundary conditions were made. The employed central scheme is not able to provide sufficient dissipation near the upper boundary, where the grid is very coarse. In order to maintain numerical stability a second order Jameson-like (Jameson *et al.*, 1981) dissipation is added locally in this region. Similarly to the compression-corner simulation, the inflow-boundary conditions are prepared from the preceeding simulation. It is worthwhile noting that an essential temporal inhomogeneity of the inflow data caused by the shock-system unsteadiness does not permit the use of temporally periodic inflow conditions.

An instantaneous snapshot of the flow averaged in spanwise direction is presented in figure 5.1. The density (a) increases in the shock wave, and diminishes in the Prandtl-Meyer expansion. The boundary layer becomes thicker downstream of the expansion. The undisturbed boundary layer, the separated shear layer, the shock wave system with an unsteady second stem of the λ-configuration, and shocklets can be identified from the density gradient magnitude (b). Turbulent fluctuations are suppressed in the expansion fan after the decompression corner. The shocklets cannot be identified as organized structures downstream of the expansion fan, but a higher level of fluctuations in the external flow still exists. A corresponding Schlieren-type photograph from the higher-Reynolds number experiment shown in fig 5.1(c) exhibits a qualitative agreement with numerical results.

5.1 Mean flow and turbulence

The mean flow is computed from 105 samples taken with an interval of $\Delta t \approx 0.5\delta_0/U_\infty$. Due to the limited number of samples the flow is averaged additionally in the spanwise direction for smoother statistics. The mean skin-friction coefficient and the wall pressure distribution are shown in figure 5.2. The mean flow quantities of the boundary layer tend to recover their initial values during a streamwise distance of $x_1 \approx 12$ downstream of the perturbations. Generally, the comparison with the reference experiment is favorable. Some discrepancies in the overlap region may be attributed to the difficulties described earlier. The spike near the decompression corner in the skin friction is likely due to limited

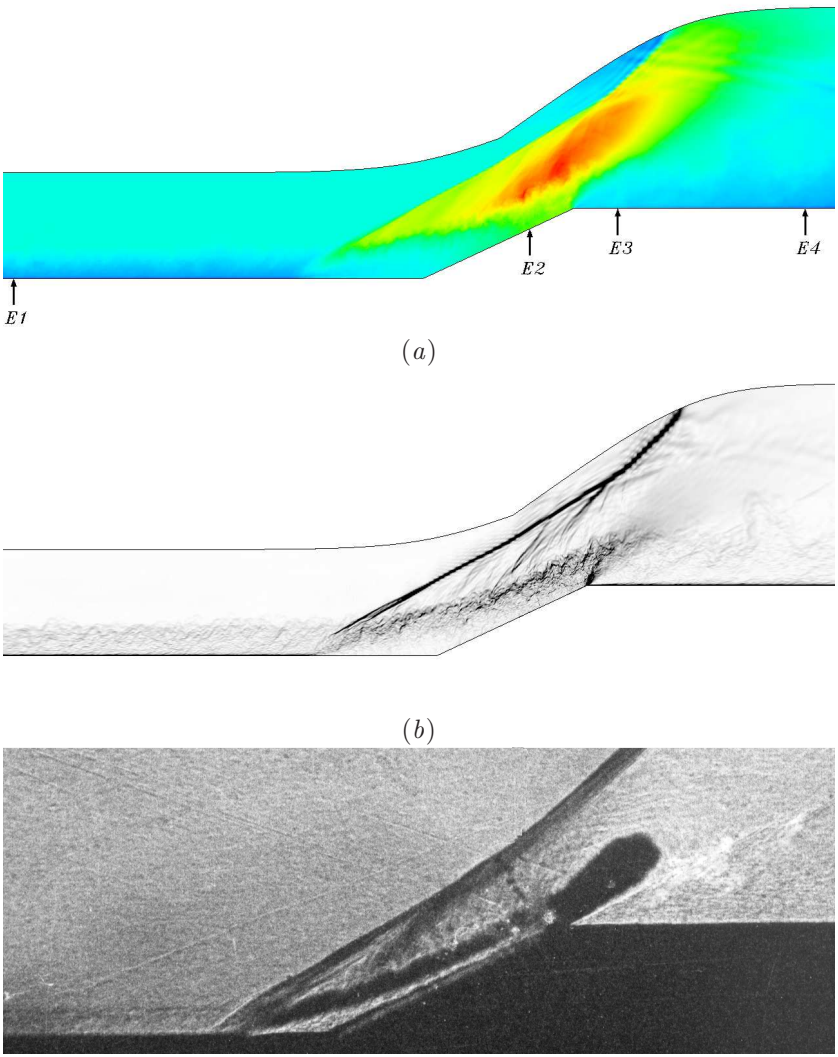

Figure 5.1: Instantaneous representation of the flow for the entire configuration. The calculated density (a), Schlieren-type picture (b) and Schlieren visualization of the higher-Reynolds number experiment (c).

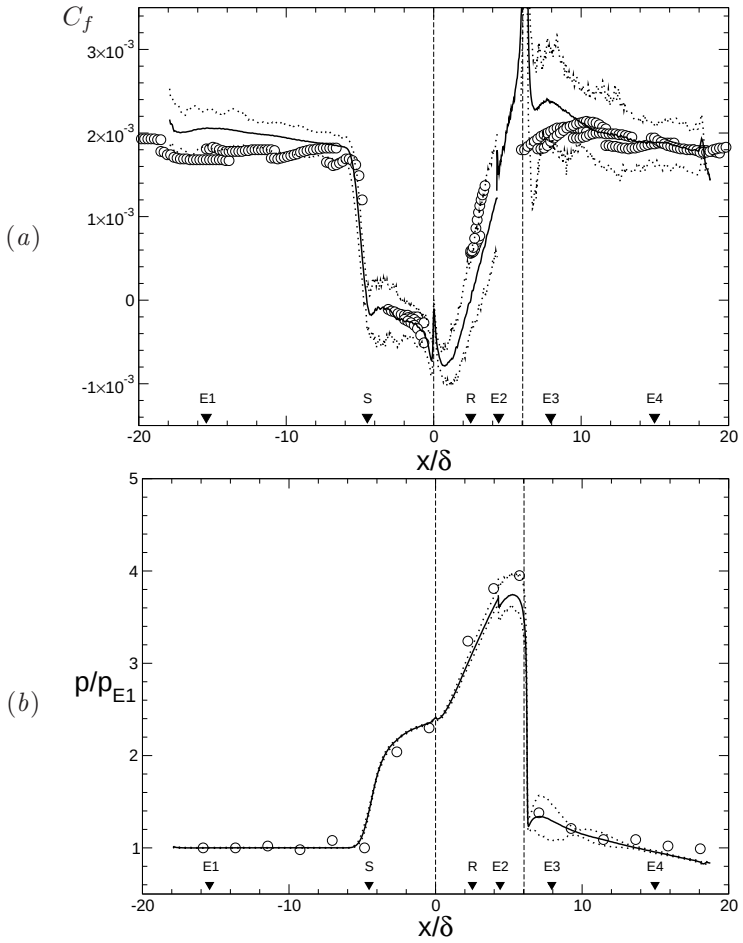

Figure 5.2: Averaged skin-friction coefficient (a) and wall-pressure (b) distributions in the streamwise direction. ○ *, reference experiment;* ——— *, current LES averaged in time and over spanwise direction;* ····· *, compression corner simulation results in the overlapping part of the domains. Symbols* $E1 - E4$ *point to the experimental positions,* S *and* R *are separation and reattachment positions. The leftmost dashed vertical line indicates the compression-corner position and the right-most dashed vertical line the decompression-corner of the experiment.*

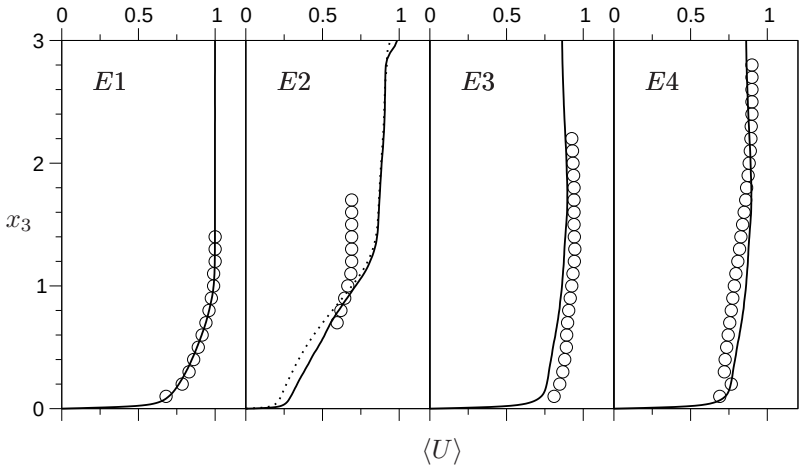

Figure 5.3: Velocity profiles at several downstream sections $E1 - E4$. ∘ , reference experiment; ——— , current LES averaged in time and over spanwise direction; ····· , compression corner simulation results in the overlapping part of the domains.

resolution of the corner singularity. Sharp gradients of flow variables occur over a short distance near the compression and decompression corner positions causing a Gibbs-like oscillation in the numerical solution. A slight pressure increase in the region $6 < x_1 < 7$ may indicate the existence of a weak compression wave inside the boundary layer downstream of the expansion as sketched in figure 1.4.

Figure 5.3 gives an impression of the mean velocity profile evolution in the streamwise direction. The computational data are shown by solid and dotted lines, having the same meaning as in figure 5.2. The inner velocity deficit at station $E2$ is compensated by the expansion (station $E3$). A developed turbulent boundary layer profile is recovered approximately at the downstream station $E4$. The profiles of the undisturbed turbulent boundary layer at station $E1$ and downstream of the expansion at stations $E3, E4$ agree well with experimental data. As explained in section 4.1, differences inside the boundary layer at section $E2$ ($x_3 > 1$) may be attributed to a deficiency of the experimental measurement technique.

The spanwise distribution of C_f is presented in figure 5.4. A comparison of data in the overlap region (station $E2$) reveals a deviation of the decompression-corner results (solid line) from the compression-corner simulation (dotted line). The difference can be attributed to the different amount of statistical data collected in both simulations. The influence of Görtler-like vortices on the surface data decreases at station $E3$ and disappears further downstream at station $E4$, suggesting that streamwise vortices decay while passing through the expansion. A volumetric visualization also supports this conclusion. Apparently in the current simulation vortices decay shortly downstream of the decompression corner. Generally, the evolution of the streamwise vortices further downstream is an open question. It is unclear how long they exist in the subsonic flow, even in the absence of a favorable pressure gradient (Floryan, 1991), while for a compression corner at hypersonic speeds at $M = 6$ they survive only for a rather short distance downstream of the region with concave streamline curvature (Simeonides, 1993). The oil-flow visualization in the higher Reynolds number experiment supports this claim also.

Root-mean-square (RMS) values of the mass-flux $\langle (\rho U)'^2 \rangle^{1/2}$, density $\langle \rho'^2 \rangle^{1/2}$, and velocity $\langle U'^2 \rangle^{1/2}$ fluctuations (top to bottom) are shown at several downstream sections $E1 - E4$ in figure 5.5. The profiles are normalized with values of the undisturbed boundary layer in accordance with the experiment of Zheltovodov & Yakovlev (1986). As predicted by the experiment the RMS values increase during the interaction with the shock (see station $E2$) shifting the maximum from a near wall position to the shear layer. The Prandtl-Meyer expansion moves the maximum further away from the wall and damps the RMS values. Fluctuations are rather large outside of the boundary layer. Obviously the RMS profiles at the downstream section $E4$ have a shape which is different from that of the equilibrium boundary layer at the inflow station $E1$. The agreement with the experimental data is good, some discrepancies at station $E2$ are discussed in section 4.4. The near-wall peaks which are well-resolved in the simulation are not captured by the experiment.

The behavior of the mass-flux fluctuation in the boundary layer and in the external flow is compared with the reference experiment in figure 5.6. The maxima of the profiles are taken for a fluctuation analysis within the boundary layer, while the values in the range $2 < x_3 < 3$ are taken from the outer flow (refer to figure 5.5*a*). The data are normalized with their respective values at station $E1$. The results inside the

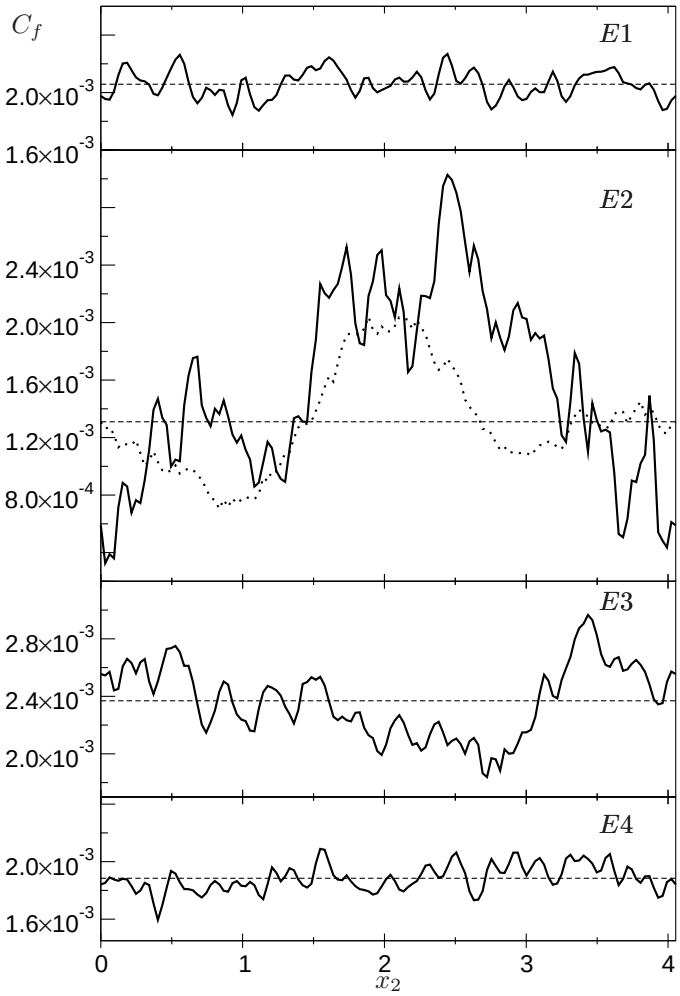

Figure 5.4: Distribution of the mean skin-friction coefficient at the wall in spanwise direction. ——— *, averaged in time;* – – – – *, averaged in time and over spanwise direction;* ····· *, compression corner simulation results in the overlapping part of the domains.*

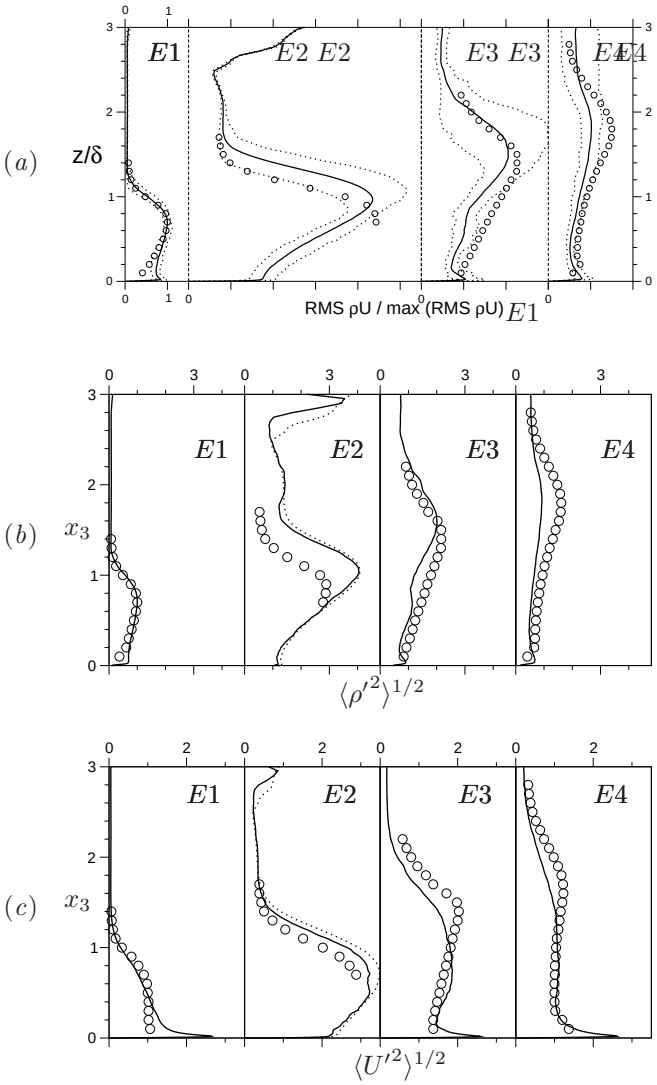

Figure 5.5: Root-mean-square of the momentum (a), density (b) and velocity (c) fluctuations between position $E1$ and position $E4$. ∘ , reference experiment; ——— , current LES averaged in time and over spanwise direction; ····· , compression corner simulation results in the overlapping part of the domains.

boundary layer show a good agreement with the experiment. The fluctuations are amplified within the shock at station $E2$ and then damped by the expansion almost down to the initial level at station $E4$. In the outer flow turbulent fluctuations grow by an order of magnitude during the interaction with the shock. The expansion decreases this level, but it remains at a significantly higher level than the initial one over a long distance downstream. The simulation qualitatively follows this trend, a quantitative comparison is difficult because of the low level of external turbulence at station $E1$ which is used for normalization. An additional uncertainty is introduced by the ambiguity in determining the *external* part of the profile in the separation region. This behavior of the turbulence outside the boundary layer can be explained as follows. The turbulence is amplified by the interaction with the shock wave, the shocklets also contribute to the enhancement of fluctuation, as described in section 4.3.2. The expansion destroys the shocklets as coherent structures, but does not damp entirely the fluctuations caused by them, thus keeping the external turbulence level high. This is an important feature of the flow captured by the current LES, since the outer turbulence has an influence on the heat transfer at the wall.

5.2 Turbulent kinetic energy balance

A fundamental equation used in turbulence modeling is the transport equation of the turbulent kinetic energy which can be written according to Gatski (1997) as:

$$\underbrace{\frac{\partial \langle\rho\rangle K}{\partial t} + \frac{\partial}{\partial x_j}\left(\{u_j\}\langle\rho\rangle K\right)}_{I} = \underbrace{\langle\rho\rangle \mathcal{P}}_{II} + \underbrace{\langle\rho\rangle \Pi^d}_{III} + \underbrace{\mathcal{M}}_{IV} + \underbrace{\frac{\partial \mathcal{D}_j^t}{\partial x_j}}_{V} - \underbrace{\langle\rho\rangle \varepsilon}_{VI} + \underbrace{\frac{\partial}{\partial x_j}\left(\frac{\langle\mu\rangle}{Re}\frac{\partial K}{\partial x_j}\right)}_{VII}, \tag{5.1}$$

where the turbulent kinetic energy (TKE) is defined as

$$\langle\rho\rangle K = \frac{1}{2}\langle\rho u_i'' u_i''\rangle \ .$$

The following definitions and interpretations are assigned to the individual terms of equation (5.1):

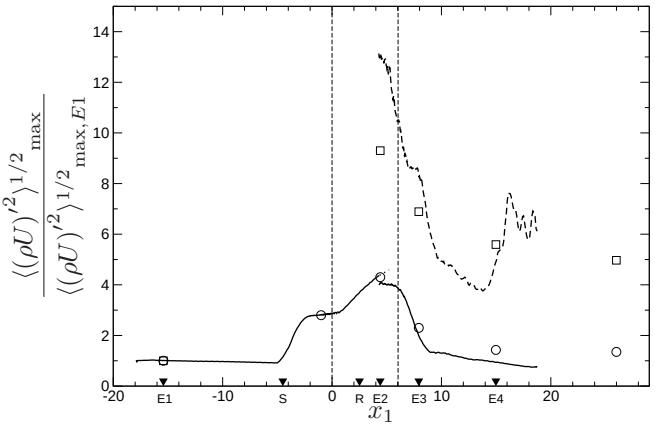

Figure 5.6: Relative changes of RMS of momentum fluctuations with streamwise direction. ——— *, along the profile maxima in the boundary layer;* - - - - *, in the external flow;* ∘ *, reference experiment. The compression corner data were not analyzed for the external flow.*

(I) is the convection of K;

(II) is the production of K

$$\langle\rho\rangle\,\mathcal{P} = -\left\langle\rho u_i'' u_j''\right\rangle \frac{\partial\left\{u_i\right\}}{\partial x_j}\ ;$$

(III) is the pressure dilatation

$$\langle\rho\rangle\,\Pi^d = \left\langle p' \frac{\partial u_k'}{\partial x_k}\right\rangle\ ,$$

which is a purely compressible term since it vanishes for divergence-free flows;

(IV) is the mass flux variation

$$\mathcal{M} = \langle u_i''\rangle \left(\frac{\partial\langle\tau_{ij}\rangle}{\partial x_j} - \frac{\partial\langle p\rangle}{\partial x_i}\right)\ ,$$

(V) is the turbulent diffusion

$$\frac{\partial \mathcal{D}_j^t}{\partial x_j} = -\frac{\partial}{\partial x_j}\left[\frac{1}{2}\left\langle \rho u_i'' u_i'' u_j'' \right\rangle + \left\langle p' u_j' \right\rangle\right] \ ;$$

(VI) is the turbulent dissipation

$$\langle \rho \rangle \, \varepsilon = \left\langle \tau_{ij}' \frac{\partial u_i'}{\partial x_j} \right\rangle \ ;$$

(VII) is the viscous diffusion.

These terms are non-dimensionalized by the free-stream quantities as described in section 2.2. It should be noted that correlations involving viscosity fluctuations have been neglected in the definitions of terms VI and VII. They are certainly unimportant in the present case (Huang *et al.*, 1995).

The wall-normal distribution of individual terms at stations $E1 - E4$ is presented in figures 5.7, 5.8. Our results show that the turbulent convection (I), pressure dilatation (III) and mass-flux-variation (IV) are very small at station $E1$. In order to show relatively small terms clearly we presented them magnified in the insets. TKE production (II) and the turbulent dissipation (VI) occur mainly near the wall. In the interaction region at section $E2$ convection (I) and production (II) terms become significantly higher and have a different distribution across the boundary layer. Along with increased fluctuation levels (see figure 5.5) the dissipation (V) also increases. Near the wall, a steep increase of velocity fluctuations causes large dissipation rates. Other terms change only slightly. At section $E3$ the production term (II) becomes negative indicating a damping of turbulent fluctuations. Further downstream the profiles tend to recover the undisturbed shapes. Due to limited statistical samples collected in the decompression corner simulation some terms are difficult to analyze. They incorporate third and fourth order correlations and definitely are statistically not converged.

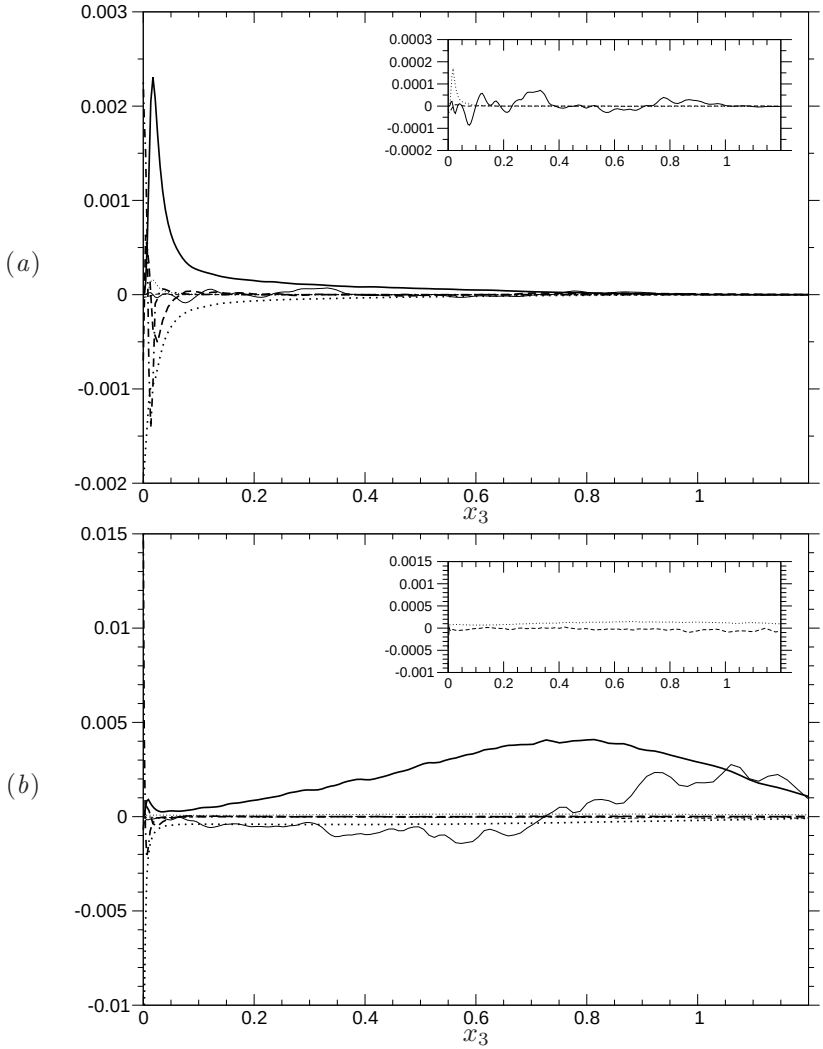

*Figure 5.7: Turbulence kinetic energy budget at station E*1 *(a), E*2 *(b). Individual terms are according to equation (5.1):* ——— *, I;* ——— *, II;* - - - - *, III;* ····· *, IV;* - - - - *, V;* ····· *, VI;* —·— *, VII.*

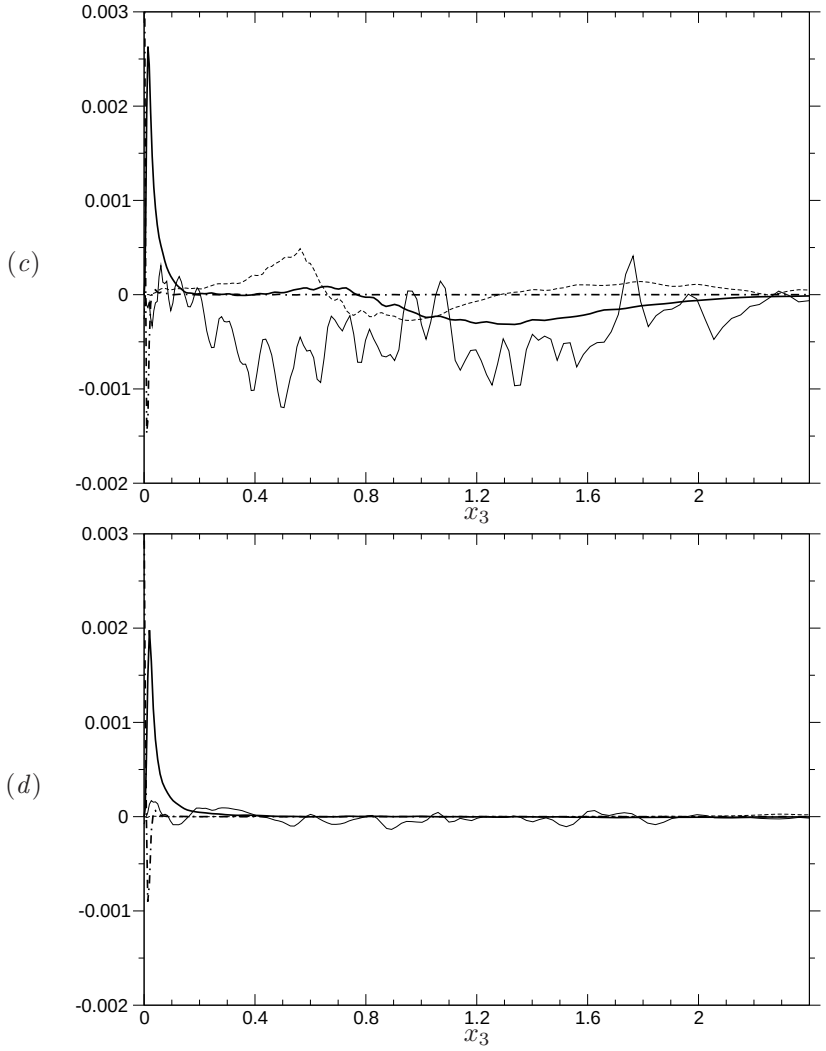

Figure 5.8: Turbulence kinetic energy budget at station E3 (c), E4 (d). Individual terms are according to equation (5.1): ——— *, I;* ——— *, II;* – – – – *, III;* ····· *, IV;* – – – – *, V;* ····· *, VI;* —·— *, VII.*

Chapter 6

Conclusions

The numerical investigation of compression-decompression ramp flow was performed using large-eddy simulation. Unprecedentedly, a high Reynolds number corresponding to experimental conditions is achieved, allowing direct comparison. The Reynolds number based on the incoming boundary-layer thickness is $Re_{\delta_0} = 63560$, the free-stream Mach number is $M_\infty = 2.95$. For obtaining the numerical solution a high-order compact difference scheme was used. The subgrid-scales are modelled by the Approximate Deconvolution Method.

The results are validated successfully against the reference experiment. In particular a good agreement was achieved for surface-pressure and skin-friction distributions, mean velocity profiles, mass-flow, density and velocity fluctuations and wall-pressure-fluctuation distributions. It was possible to resolve entirely the unsteady behavior of the shock system around the separation region. Along with high frequency fluctuations of the shock system a large-scale shock motion was confirmed by the simulation. Aside of the direct shock-turbulence interaction a mechanism for turbulence amplification in the external flow above the detached shear layer was proposed based on downstream travelling shocklets. This explains a nature of experimentally observed turbulence amplification and details its acoustic mode downstream of the shock wave. The existence of streamwise Görtler-type vortices was corroborated by the simulation. The effect of these structures on the spanwise mean-flow variation should be taken into account in validation efforts of CFD methods based on experimental data. Indications for a relaminarization tendency in the separation region were found.

The results of current research was presented at several seminars held in the Institute of Fluid Dynamics (ETHZ, Zürich), Institute of Theoretical and Applied Mechanics (Novosibirsk), Institute of Aerodynamics (TUM, Munich), Institute of Aerodynamics and Flow Technology (DLR, Göttingen). The publications include conference proceedings (Zheltovodov *et al.*, 2003; Loginov & Adams, 2003; Loginov *et al.*, 2003, 2004*a*,*b*,*c*, 2005*c*,*a*,*b*, 2006*b*) and a paper in a peer-reviewed journal (Loginov *et al.*, 2006*a*).

Appendix A

Summary of flat-plate boundary layer simulations

Reference	M_∞	Re_θ	$N_1 \times N_2 \times N_3$	$\Delta^+_{x_1} \times \Delta^+_{x_2} \times \Delta^+_{x_3}$	SGS	comments
Rai *et al.* (1995)	2.25	≈ 4500	$971 \times 321 \times 55$	$27 \times 10.4 \times 0.95$	DNS	SE, AW
Spyropoulos & Blaisdell (1998)	2.25	≈ 4300	$416 \times 257 \times 55$	$59 \times 11.4 \times 0.87$	DS	SE, AW
Guarini *et al.* (2000)	2.5	1577	$256 \times 192 \times 209$	$8.86 \times 5.96 \times 0.48$	DNS	SG, AW
Maeder *et al.* (2001)	3	3038	$192 \times 144 \times 180$	$2.9 \times 2.2 \times 1.3$	DNS	ET, IW
Maeder *et al.* (2001)	4.5	3305	$432 \times 192 \times 200$	$2.9 \times 1.6 \times 0.6$	DNS	ET, IW
Maeder *et al.* (2001)	6	2945	$240 \times 160 \times 220$	$1.3 \times 1.1 \times 0.5$	DNS	ET, IW
Gatski & Erlebacher (2002)	2.25	4250	$1701 \times 501 \times 55$	$13.9 \times 6.8 \times 0.97$	DNS	SE, AW
Yan *et al.* (2002*b*)	2.88	$Re_\delta = 20000$	1.4×10^6 cells	$20; 18 \times 7; 6.4 \times 1.8; 1.6$	MILES	RRM, AW; IW
Yan *et al.* (2002*b*)	4	$Re_\delta = 20000$	1.4×10^6 cells	$12; 11 \times 4; 3.4 \times 1.8; 1.6$	MILES	RRM, AW; IW
Yan *et al.* (2002*a*)	2.88	$Re_\delta = 82400$	N/A	$17 \times 17 \times 1.8$	MILES	RRM, AW
Stolz & Adams (2003)	2.5	4530	$251 \times 51 \times 101$	$41 \times 21 \times 2.7$	ADM	RRM, IW
Stolz & Adams (2003)	2.5	10049	$361 \times 73 \times 145$	$59 \times 29 \times 3.6$	ADM	RRM, IW
Pirozzoli *et al.* (2004)	2.25	4246	$2065 \times 255 \times 56$	$14.5 \times 6.56 \times 1.05$	DNS	SE, AW
Rizzetta & Visbal (2004)	2.25		$371 \times 151 \times 61$	$83.81 \times 21.55 \times 0.9$	MILES, S, DS	SE, AW

Table A.1: Summary of DNS/LES for a flat-plate boundary layer. Subgrid scale models: DNS — direct numerical simulation (no SGS model); DS — dynamic Smagorinsky SGS model; MILES — monotonically integrated large-eddy simulation; ADM — approximate deconvolution model; S — Smagorinsky SGS model. Comments: SE — spatially evolving boundary layer; SG — "slow growth" formulation; ET — "extended temporal" approach; AW — adiabatic wall; IW — isotermal wall.

Appendix B

Summary of compression ramp simulations

Reference					
Hunt & Nixon (1995)	Adams (1998), Adams (2000)	Urbin *et al.* (1999)	Yan *et al.* (2001)	Rizzetta *et al.* (2001)	Rizzetta & Visbal (2002)
Deflection angle (β)					
24°	18°	8°	25°	18°	8; 16; 20; 24°
Free-stream Mach number (M_∞)					
2.8	3	3	2.88	3	3
Free-stream Reynolds number (Re_{δ_0})					
10^6	21365	20000	20000	20807	20807
SGS model					
two part eddy-viscosity model of Moin & Kim (1982)	DNS	classical constant-coefficient Smagorinsky (1963) model with Van Driest dumping near the wall	MILES (Boris *et al.*, 1992)	Smagorinsky (1963) model, dynamic Smagorinsky model (Germano *et al.*, 1991), MILES (Boris *et al.*, 1992)	dynamic Smagorinsky model (Germano *et al.*, 1991)
Grid size *(streamwise × spanwise × wall-normal, total)*					
$117 \times 61 \times 59$, $\approx 0.42 \times 10^6$	$1001 \times 81 \times 181$, $\approx 14.7 \times 10^6$	unstructured grid, 1.6×10^6	unstructured grid $213 \times 57 \times 35$ nodes, $\approx 2 \times 10^6$ tetras	$421 \times 81 \times 151$, $\approx 5.1 \times 10^6$	$421 \times 81 \times 151$, $\approx 5.1 \times 10^6$

Hunt & Nixon (1995)	Adams (1998), Adams (2000)	Urbin *et al.* (1999)	Yan *et al.* (2001)	Rizzetta *et al.* (2001)	Rizzetta & Visbal (2002)
Spatial discretization					
convective terms					
N/A	hybrid compact-ENO finite-difference scheme (Adams & Shariff, 1996): 5th-order Padé-like upwind biased scheme, 4th-order ENO scheme around discontinuities	finite volume, 2nd order reconstruction by least square method of Ollivier-Gooch (1997)	finite volume, 2nd order reconstruction by least square method of Ollivier-Gooch (1997)	6th-order compact finite-difference scheme of Lele (1992) in conjunction with a 10th-order nondispersive filter (Gaitonde *et al.*, 1997), upwind biased scheme of Roe (1981) using MUSCL interpolation is employed near the shocks	6th-order compact finite-difference scheme of Lele (1992) in conjunction with a 10th-order nondispersive filter (Gaitonde *et al.*, 1997), upwind biased scheme of Roe (1981) using MUSCL interpolation is employed near the shocks
diffusion terms					
N/A	6th-order compact finite-difference scheme of Lele (1992)	finite volume, 3D version of 2nd order scheme of Knight (1994)	finite volume, 3D version of 2nd order scheme of Knight (1994)	6th-order compact finite-difference scheme of Lele (1992)	6th-order compact finite-difference scheme of Lele (1992)

Hunt & Nixon (1995)	Adams (1998), Adams (2000)	Urbin *et al.* (1999)	Yan *et al.* (2001)	Rizzetta *et al.* (2001)	Rizzetta & Visbal (2002)
Temporal discretization					
N/A	explicit low-storage 3rd-order Runge-Kutta scheme of Williamson (1980)	2nd-order	2nd-order Runge-Kutta	2nd-order approximately factored finite difference algorithm of Beam & Warming (1978) employing Newton-like subiterations	2nd-order approximately factored finite difference algorithm of Beam & Warming (1978) employing Newton-like subiterations
Domain size, δ					
streamwise (L_1)					
16	27.4	12.1	16.8	28.1	31.2
spanwise (L_2)					
5	1.22	4.4	1.925	2.9	2.9
wall-normal (L_3) inflow ÷ outflow					
3	4.57 ÷ 8.99	3.4	3.4	4.7	4.7
Inflow generation method					
Sampling time, δ_0/U_∞					
N/A	385	N/A	48	≈ 385	≈ 385
Number of samples					
N/A	600	N/A	N/A	12469	12469

Table B.1: Summary of DNS/LES for a compression corner

Reference					
Stolz *et al.* (2001*a*)	Kannepalli *et al.* (2002)	El-Askary *et al.* (2003)	von Kaenel *et al.* (2004)	Smits *et al.* (2006)	Comte & David (1996)
Deflection angle (β)					
18°	$8; 24^\circ$	$8; 18^\circ$	18°	24°	20°
Free-stream Mach number (M_∞)					
3	2.88	3	3	2.9	2.5
Free-stream Reynolds number (Re_{δ_0})					
21365	20000	20000	21365	35921	≈ 840
SGS model					
Approximate Deconvolution Model of Stolz *et al.* (2001*a*)	MILES	MILES	Approximate Deconvolution Model of Stolz *et al.* (2001*a*)	DNS	selective structure-function model of Métais & Lesieur (1992)
Grid size *(streamwise × spanwise × wall-normal, total)*					
$334 \times 31 \times 91$, $\approx 0.9 \times 10^6$	$300 \times 56 \times 65$, $\approx 1.1 \times 10^6$	$347 \times 33 \times 113$, $\approx 1.3 \times 10^6$ $975 \times 33 \times 125$, $\approx 4 \times 10^6$	$332 \times 30 \times 90$, $\approx 0.9 \times 10^6$	$412 \times 128 \times 96$, $\approx 5.1 \times 10^6$	$220 \times 25 \times 140$, $\approx 0.8 \times 10^6$
Spatial discretization					
convective terms					
6th-order compact finite-difference scheme of Lele (1992)	5th-order upwind biased with Roe-flux-extrapolation procedure (Rai & Moin, 1993)	2nd-order advection upstream splitting method of Liou & Steffen (1991)	4th-order discretization in skew-symmetric form	3rd-order accurate WENO	N/A
diffusion terms					
6th-order compact finite-difference scheme of Lele (1992)	4th-order central differencing	2th-order central differencing	computed using the gradient theorem on a shifted volume	4th-order accurate central standard method	N/A

Stolz *et al.* (2001*a*)	Kannepalli *et al.* (2002)	El-Askary *et al.* (2003)	von Kaenel *et al.* (2004)	Smits *et al.* (2006)	Comte & David (1996)
Temporal discretization					
explicit low-storage 3rd-order Runge-Kutta scheme of Williamson (1980)	2nd-order implicit three-factor approximate factorization	2nd-order explicit Runge-Kutta scheme	explicit low-storage four-stage Runge-Kutta scheme	3rd- or 4th-order accurate low-storage Runge-Kutta method	fully explicit McCormack scheme
Domain size, δ					
streamwise (L_1)					
27.4	14.8	11; 30.5	27.4	13	N/A
spanwise (L_2)					
1.22	1.93	N/A	1.22	2	≈ 1.5
wall-normal (L_3) *inflow* $\div$ *outflow*					
$4.57 \div 8.99$	3.4	N/A	$4.57 \div 8.99$	4.5	N/A
Inflow generation method					
Sampling time, δ_0/U_∞					
370	320	N/A	63	35; 90	N/A
Number of samples					
N/A	N/A	N/A	1500	N/A	N/A

Table B.2: Summary of DNS/LES for a compression corner (continue)

Appendix C

Computational details

For the current computations a FORTRAN code designed and optimized for shared memory vector-parallel computers is used. Computations are performed on the NEC SX-5/6/8 systems available at High Performance Computing Center (Höchstleistungsrechenzentrum, HLRS) in Stuttgart . Parallelization and vectorization of the code relies on the compiler automatic parallelization and manual tuning in critical sections with compiler directives (the NEC FORTRAN90/SX compiler is used). Typical values for production runs on NEC SX-5 machine are given in the table C.1. The performance ratio is in accordance with previously obtained data at another SX-5 computer with 8 GFLOPS peak performance of Swiss National Supercomputing Centre (CSCS, Switzerland). It varies slightly when running on different number of processors. Approximately 10000 CPU hours are used on this platform. Significant performance ratio decreasing was observed when calculation was running on NEC SX-6 platform. A dependence on the number of CPUs is significant in this case. We spent more then 8000 CPUh on SX-6 platform. The decomperession corner simulation was running on SX-8 platform, see table C.1 for details. The simulation is requires a vast amount of disk space to save results since a lot of instantaneous data have to be saved for time-history analysis. More than 500 GigaBytes of data have been saved for post-processing.

Table C.1: Details of the production runs SX platforms

parameter	value	comment
	SX-5	
Memory, GB	6.7	7.7 with concurrent postprocessing
Performance, MFLOPS	1748	$\approx$ 44% of peak performance
Number of CPU	5	tried 4 – 12 CPUs
Vector optimization ratio, %	99.3	
Wall clock time, hours	185.3	for 694.8 CPUh user time
	SX-6	
Memory, GB	6.9	
Performance , MFLOPS	2763	$\approx$ 30% of peak, varies 25–34%
Number of CPU	6	
Vector optimization ratio, %	99.3	
Wall clock time, hours	38.9	for 163.3 CPUh user time
	SX-8	
Memory, GB	9.8	
Performance , MFLOPS	3815	
Number of CPU	4	
Vector optimization ratio, %	99.2	
Wall clock time, hours	5.8	for 19.4 CPUh user time

Bibliography

Adams, E. W. & Johnston, J. P. 1988 Flow structure in the near-wall zone of a turbulent separated flow. *AIAA J.* **26**, 932–939.

Adams, N. A. 1998 Direct numerical simulation of turbulent compression corner flow. *Theor. Comp. Fluid Dyn.* **12**, 109–129.

Adams, N. A. 2000 Direct simulation of the turbulent boundary layer along a compression ramp at $M = 3$ and $Re_\theta = 1685$. *J. Fluid Mech.* **420**, 47–83.

Adams, N. A. & Shariff, K. 1996 A high-resolution hybrid compact-ENO scheme for shock-turbulence interaction problems. *J. Comp. Phys.* **127**, 27–51.

Adamson, T. C. & Messiter, A. F. 1980 Analysis of two-dimensional interactions between shock waves and boundary layers. *Annu. Rev. Fluid Mech.* **12**, 103–138.

Agarwal, R. 1999 Computational fluid dynamic of whole-body aircraft. *Annu. Rev. Fluid Mech.* **31**, 125–169.

Andreopoulos, J. & Muck, K. C. 1987 Some new aspects of the shock-wave/boundary-layer interaction in compression-ramp flows. *J. Fluid Mech.* **180**, 405–428.

Andreopoulos, Y., Agui, J. H. & Briassulis, G. 2000 Shock wave-turbulence interactions. *Annu. Rev. Fluid Mech.* **32**, 309–345.

Anyiwo, J. C. & Bushnell, D. M. 1982 Turbulence amplification in shock-wave boundary-layer interaction. *AIAA J.* **20**, 893–899.

Bardina, J., Ferziger, J. H. & Reynolds, W. C. 1980 Improved subgrid-scale models for large-eddy simulation. *AIAA Paper* 80-1357.

Beam, R. & Warming, R. 1978 An implicit implicit factored scheme for the compressible Navier-Stokes equations. *AIAA J.* **16**, 393–402.

Bedarev, I. A., Zheltovodov, A. A. & Fedorova, N. N. 1998 Supersonic turbulent separated flows numerical model verification. In *International Confenference on the Methods of Aerophysical Research, Part 1*, pp. 30–35. Novosibirsk, Russia, June 29 - July 3, 1998.

Bertero, M. & Boccacci, P. 1998 *Introduction to Inverse Problems in Imaging*. Bristol: IOP Publishing.

Bookey, P., Smits, A. J., Martin, M. P. & Wyckham, C. 2005 New experimental data of STBLI at DNS/LES accessible Reynolds numbers. *AIAA Paper* 05–309.

Boris, J. P., Grinstein, F. F., Oran, E. S. & Kolbe, R. L. 1992 New insights into large eddy simulation. *Fluid Dynamics Research* **10**, 199–228.

Borisov, A. V., Vorontsov, S. S., Zheltovodov, A. A., Pavlov, A. A. & Shpak, S. I. 1993 Development of experimental and computational methods of studies of supersonic separated flows. Preprint 9-93 ITAM, RAS SB, Novosibirsk, (in Russian).

Borisov, A. V., Zheltovodov, A. A., Maksimov, A. I., Fedorova, N. N. & Shpak, S. I. 1996 Verification of turbulence models and computational methods of supersonic separated flows. In *International Confenference on the Methods of Aerophysical Research, Part 1*, pp. 54–61. Novosibirsk, Russia, September 2 - 6, 1996.

Borisov, A. V., Zheltovodov, A. A., Maksimov, A. I., Fedorova, N. N. & Shpak, S. I. 1999 Experimental and numerical study of supersonic turbulent separated flows in the neighborhood of two-dimensional obstacles. *Mekhanika Zhidkosti i Gaza (Fluid Dynamics)* **2**, 26–37, (in Russian).

Bradshaw, P. 1977 Compressible turbulent shear layers. *Annu. Rev. Fluid Mech.* **9**, 33–54.

Brazhko, V. N. 1979 Periodic structure of the flow and heat transfer in the reattachment region of supersonic flow. *Uchenye Zapiski TsAGI (Scientifical Notes of TsAGI)* **10**, 113–118, (in Russian).

Chakraborty, P., Balachandar, S. & Adrian, R. J. 2005 Shock unsteadiness in a reattaching shear layer. *J. Fluid Mech.* **535**, 189–214.

Chapman, D., Kuehn, D. & Larson, H. 1957 Investigation of separated flows in supersonic and subsonic streams with emphasis on the effect of transition. *Tech. Rep.* 1356. NACA.

Comte, P. & David, E. 1996 Large-eddy simulation of Görtler vortices in a curved compression ramp. In *Experimentation, modelling and computation in flow, turbulence and combustion, vol. 1* (ed. J. A. Dsidi, B. N. Chetverushkin, Y. A. Kuznetsov, J. Priaux & B. Stoufflet), pp. 45–61. John Willey and Sons.

Delery, J. & Marvin, J. 1986 Turbulent shock-wave / boundary layer interaction. *Tech. Rep.* AR–280. AGARD Report.

Dolling, D. S. 1998 High-speed turbulent seaparated flows: consistency of mathematic models and flow physics. *AIAA J.* **36**, 725–732.

Dolling, D. S. 2001 Fifty years of shock-wave/boundary-layer interaction research: What next? *AIAA J.* **39**, 1517–1531.

Dolling, D. S. & Murphy, M. T. 1983 Unsteadiness of the separation shock wave structure in a supersonic compression ramp flowfield. *AIAA J.* **12**, 1628–1634.

Dolling, D. S. & Or, C. T. 1985 Unsteadiness of the shock wave structure in attached and separated compression ramp flows. *Exp. in Fluids* **3**, 24–32.

El-Askary, W. A., Schröder, W. & Meinke, M. 2003 LES of compressible wall-bounded flows. *AIAA Paper* 03-3554.

Erdos, J. & Pallone, A. 1962 *Shock-Boundary Layer Interaction and Flow Separation*. Stanford University Press.

Erengil, M. E. & Dolling, D. S. 1991 Correlation of separation shock motion with pressure fluctuations in the incoming boundary layer. *AIAA J.* **29**, 1868–1877.

Fernholz, H. H. & Finley, P. J. 1977 A critical compilation of compressible turbulent boundary layer data. *Tech. Rep.* AGARDograph No. 223. AGARD, Neuilly sur Seine, France.

Fernholz, H. H. & Finley, P. J. 1981 A further compilation of compressible boundary layer data with a survey of turbulence data. *Tech. Rep.* AGARDograph No. 263. AGARD, Neuilly sur Seine, France.

Floryan, J. M. 1991 On the Görtler instability of boundary layers. *Prog. Aerospace Sci.* **28**, 235–271.

Gaitonde, D., Shang, J. S. & Young, J. L. 1997 Practical aspects of high-order accurate finite-volume schemes for electomagnetics. *AIAA Paper* 97-0363.

Garnier, E., Sagaut, P. & Adams, N.A. 2007 *Large-Eddy Simulation for compressible flows*. Springer.

Garnier, E., Sagaut, P. & Deville, M. 2002 Large eddy simulation of shock / boundary-layer interaction. *AIAA J.* **40**, 1935–1944.

Gatski, B. & Erlebacher, G. 2002 Numerical simulation of a spatially evolving supersonic turbulent boundary layer. *Tech. Rep.* NASA TM-2002-211934. NASA Langley Research Center, Hampton, Virginia 23681-2199.

Gatski, T. B. 1997 Modeling compressibility effects on turbulence. In *New Tools in Turbulence Modelling* (ed. O. Métais & J. H. Ferziger), pp. 73–104. Springer Verlag.

Germano, M., Piomelli, U., Moin, P. & Cabot, W. H. 1991 A dynamic subgrid-scale eddy viscosity model. *Phys. Fluids* **3**, 1760–1765.

Ginoux, J. J. 1971 Streamwise vortices in reattaching high-speed flows: a suggested approach. *AIAA J.* **9**, 759–760.

Görtler, H. 1954 On the three-dimensional instability of laminar boundary layers on concave walls. *Tech. Rep.* 1375. NACA.

Guarini, S. E., Moser, R. D., Shariff, K. & Wray, A. 2000 Direct numerical simulation of a supersonic turbulent boundary layer at mach 2.5. *J. Fluid Mech.* **414**, 1–33.

Hopkins, E. J. & Inouye, M. 1971 An evaluation of theories for predicting turbulent skin friction and heat transfer on flat plates at supersonic and hypersonic Mach numbers. *AIAA J.* **9**, 993–1003.

Huang, P. G., Coleman, G. N. & Bradshaw, P. 1995 Compressible turbulent channel flows: DNS results and modeling. *J. Fluid Mech.* **305**, 185–218.

Hunt, D. L. & Nixon, D. 1995 A very large eddy simulation of an unsteady shock wave/turbulent boundary layer interaction. *AIAA Paper* 95-2212.

Inger, G. R. 1977 Three-dimensional heat- and mass- transfer effects across high-speed reattaching flows. *AIAA J.* **15**, 383–389.

J.-P. Dussauge, P. Dupont & J.-F.Debiève 2006 Unsteadiness in shock wave boundary layer interactions with separation. *Aerospace Science and Technology* **10**, 85–91.

Jameson, A., Schmidt, W. & Turkel, E. 1981 Numerical solution of the euler equations by finite volume methods using runge-kutta time-stepping schemes. *AIAA Paper* 81-1259.

Kannepalli, C., Arunajatesan, S. & Dash, S. M. 2002 RANS/LES methodology for supersonic transverse jet interactions with approach flow. *AIAA Paper* 02-1139.

Knight, D., Yan, H. & Zheltovodov, A. A. 2001 Large eddy simulation of supersonic turbulent flow in expansion-compression corner. In *Third AFOSR Intern. Conf. on DNS and LES*, pp. 183–194. Arlington: Univ. of Texas, August 5–9, 2001.

Knight, Doyle D. 1994 A fully implicit navier-stokes algorithm using an unstructured grid and flux difference splitting. *Applied Numerical Mathematics* **16**, 101–128.

Knight, D. D. & Degrez, G. 1998 Shock wave boundary layer interactions in high mach number flows – a critical survey of current CFD prediction capabilities. *Tech. Rep.* AR-319. AGARD Report.

Knight, D. D., Yan, H., Panaras, A. G. & Zheltovodov, A. A. 2003 Advances in CFD prediction of shock wave turbulent boundary layer interactions. *Progress in Aerospace Sciences* **39**, 121–184.

Kovasznay, L. S. G. 1953 Turbulence in supersonic flow. *J. Aero. Sci.* **20**, 657–682.

Lee, S., Lele, S. K. & Moin, P. 1991 Eddy shocklets in decaying compressible turbulence. *Phys. Fluids A* **3**, 657–664.

Lee, S., Lele, S. K. & Moin, P. 1997 Interaction of isotropic turbulence with shock waves: effect of shock strength. *J. Fluid Mech.* **340**, 225–247.

Lele, S. K. 1992 Compact Finite Difference Schemes with Spectral-like Resolution. *J. Comp. Phys.* **103**, 16–42.

Liou, M.-S. & Steffen, C.J. 1991 A new flux splitting scheme. *Tech. Rep.* NASA TM 104404. NASA Technical Memorandum.

Loginov, M. S. & Adams, N. A. 2003 Large eddy simulation of supersonic turbulent flow in compression corner at high Reynols number. In *STAB Workshop (book of abstracts)*, pp. 157–158. Göttingen, Germany, November 4 – 5, 2003.

Loginov, M. S., Adams, N. A. & Zheltovodov, A. A. 2004*a* Large-eddy simulation of shock-wave / turbulent-boundary-layer interaction. In *21st International Congress of Theoretical and Applied Mechanics (book of abstracts and CD-ROM proceedings)*, p. 177. Warsaw, Poland, August 15 – 21, 2004.

Loginov, M. S., Adams, N. A. & Zheltovodov, A. A. 2004*b* Large-eddy simulation of shock wave / turbulent boundary layer interaction at high Reynolds number. In *Gesellschaft für Angewandte Mathematik und Mechanik e.V. 75th Annual Scientific Conference (book of abstracts)*, pp. 163–164. Dresden, Germany, March 21 – 27, 2004.

Loginov, M. S., Adams, N. A. & Zheltovodov, A. A. 2004*c* Large-eddy simulation of turbulent boundary layer interaction with successive shock and expansion waves. In *International Confenference on the Methods of Aerophysical Research, Part 1*, pp. 149–157. Novosibirsk, Russia, June 28 – July 3, 2004.

Loginov, M. S., Adams, N. A. & Zheltovodov, A. A. 2005*a* Large-eddy simulation of separated flow along a compression ramp at high Reynolds number. In *ERCOFTAC workshop: Direct and Large-eddy simulations — 6 (book of abstracts)*, pp. 164–165. Poitiers-Futuroscope, France, September 12 – 14, 2005.

Loginov, M. S., Adams, N. A. & Zheltovodov, A. A. 2005*b* Large-eddy simulation of the compression ramp flow. In *EUROMECH Colloquium 469: Large-eddy simulations of complex flows (book of abstracts)*, pp. 63–64. Dresden, Germany, October 6 – 8, 2005.

Loginov, M. S., Adams, N. A. & Zheltovodov, A. A. 2005*c* LES of shock wave / turbulent boundary layer interaction. In *High Performance Computing in Science and Engineering 04* (ed. E. Krause, W. Jäger & M. Resch), pp. 177–188.

Loginov, M. S., Adams, N. A. & Zheltovodov, A. A. 2006*a* Large-eddy simulation of shock-wave/turbulent-boundary-layer interaction. *J. Fluid Mech.* **565**, 135–169.

Loginov, M. S., Adams, N. A. & Zheltovodov, A. A. 2006*b* LES of shock wave / turbulent boundary layer interaction. In *High Performance Computing in Science and Engineering 05* (ed. W. E. Nagel, W. Jäger & M. Resch), pp. 221–234.

Loginov, M. S., Zheltovodov, A. A. & Adams, N. A. 2003 Large-eddy simulation of shock / turbulent boundary layer interaction in a compression corner. In *III all-Russian young scientist conference, Problems in mechanics: theory, experiment and new technologies (book of abstracts)*. Novosibirsk, Russia, November 19 – 21, 2003 (in Russian).

Lüdeke, H., Radespiel, R. & Schülein, E. 2004 Simulation of streamwise vortices at the flaps of re-entry vehicles. *Aerospace Science and Technology* **8**, 703–714.

Lund, T. S., Wu, X. & Squires, K. D. 1998 Generation of turbulent inflow data for spatially-developing boundary layer simulations. *J. Comp. Phys.* **140**, 233–258.

Maeder, T., Adams, N. A. & Kleiser, L. 2001 Direct simulation of turbulent supersonic boundary layers by an extended temporal approach. *J. Fluid Mech.* **429**, 187–216.

Meneveau, C. & Katz, J. 2000 Scale-invariance and turbulence models for large-eddy simulation. *Annu. Rev. Fluid Mech.* **32**, 1–32.

Métais, O. & Lesieur, M. 1992 Spectral large-eddy simulations of isotropic and stably-stratified turbulence. *J. Fluid Mech.* **239**, 157–194.

Moin, P. 2002 Advances in large eddy simulation methodology for complex ?ows. *Int. J. Heat and Fluid Flows* **23**, 710–720.

Moin, P. & Kim, J. 1982 Numerical investigation of turbulent channel flow. *J. Fluid Mech.* **118**, 341–377.

Morkovin, M. V. 1962 Effects of compressibility on turbulent flows. In *M'ecanique de la Turbulence* (ed. A. Favre), pp. 367–380. CNRS, Paris.

Ollivier-Gooch, Carl F. 1997 High-order eno schemes for unstructured meshes based on least-squares reconstruction. *AIAA Paper* 97-0540.

Pirozzoli, S., Grasso, F. & Gatski, T. B. 2004 Direct numerical simulation and analysis of a spatially evolving supersonic turbulent boundary layer at m=2.25. *Phys. Fluids* **16**, 530–545.

Plotkin, K. J. 1975 Shock wave oscillation driven by turbulent boundary-layer fluctuations. *AIAA J.* **13**, 1036–1040.

Poggie, J. & Smits, A. J. 2001 Shock unsteadiness in a reattaching shear layer. *J. Fluid Mech.* **429**, 155–185.

Poggie, J. & Smits, A. J. 2005 Experimental evidence for Plotkin model of shock unsteadiness in separated flow. *Phys. Fluids* **17**, 018107–1–018107–4.

Rai, M.M. & Moin, P. 1993 Direct numerical simulation of transition and turbulence in a spatially evolving boundary layer. *J. Comp. Phys.* **109** (2), 169–192.

Rai, M. M., Gatski, T. B. & Erlebacher, G. 1995 Direct simulation of spatially evolving compressible turbulent boundary layers. *AIAA Paper* 95-0583.

Ribner, H. S. 1954 Shock-turbulence interaction and the generation of noise. *Tech. Rep.* 1233. NACA.

Rizzetta, D. P. & Visbal, M. R. 2002 Application of large-eddy simulation to supersonic compression ramps. *AIAA J.* **40**, 1574–1581.

Rizzetta, D. P. & Visbal, M. R. 2004 Large-eddy simulation of supersonic boundary-layer flow by a high-order method. *International Journal of Computational Fluid Dynamics* **18**, 15–27.

Rizzetta, D. P., Visbal, M. R. & Gaitonde, D. V. 2001 Large-eddy simulation of supersonic compression-ramp flow by high-order method. *AIAA J.* **39**, 2283–2292.

Roe, P. L. 1981 Approximate Riemann solvers, parameter vectors and difference schemes. *J. Comput. Phys.* **43**, 357–372.

Sagaut, P. 2002 *Large-Eddy Simulation for Incompressible Flows*, 2nd edn. Springer.

Saric, W. S. 1994 Görtler vortices. *Annu. Rev. Fluid Mech.* **26**, 379–409.

Settles, G. S. & Dodson, L. J. 1991 Hypersonic shock/boundary-layer interaction database. *Tech. Rep.* NASA CR 177577. NASA Ames Research Center, Moffet Field, California.

Settles, G. S. & Dodson, L. J. 1994 Supersonic and hypersonic shock / boundary layer interaction database. *AIAA J.* **32**, 1377–1383.

Settles, G. S. & Dolling, D. S. 1990 Swept shock/ boundary-layer interactions – tutorial and update. *AIAA Paper* 90-0375.

Settles, G. S., Fitzpatrick, Th. J. & Bogdonoff, S. M. 1979 Detailed study of attached and separated compression corner flowfields in high Reynolds number supersonic flow. *AIAA J.* **17**, 579–585.

Simeonides, G. 1993 Hypersonic shock wave boundary layer interactions over simplified deflected control surface configurations. *Tech. Rep.* AR-792. AGARD Report.

Sinha, K., Mahesh, K. & Candler, G. V. 2005 Modeling the effect of shock unsteadiness in shock / turbulent boundary-layer interactions. *AIAA J.* **43**, 586–594.

Smagorinsky, J. 1963 General circulation experiments with the primitive equations. i. the basic experiment. *Mon. Weather Rev.* **91**, 99–164.

Smits, A. J. & Dussauge, J.-P. 1996 *Turbulent Shear Layers in Supersonic Flow*. Woodbury, New York: AIP Press.

Smits, A. J. & Muck, K.-C. 1987 Experimental study of three shock wave / turbulent boundary layer interactions. *J. Fluid Mech.* **182**, 291–314.

Smits, A. J. & Wood, D. H. 1985 The response of turbulent boundary layers to sudden perturbations. *Annu. Rev. Fluid Mech.* **17**, 321–358.

Smits, M. P. Martin A., Wu, M. & Ringuette, M. 2006 The turbulence structure of shockwave and boundary layer interaction in a compression corner. *AIAA Paper* 06–0497.

Spalart, P. R. 1988 Direct simulation of a turbulent boundary layer up to $Re_\theta = 1410$. *J. Fluid Mech.* **187**, 61–98.

Spina, E. F., Smits, A. J. & Robinson, S. K. 1994 The physics of supersonic turbulent boundary layers. *Annu. Rev. Fluid Mech.* **26**, 287–319.

Spyropoulos, E. T. & Blaisdell, G. A. 1998 Large-eddy simulation of a spatially evolving supersonic turbulent boundary-layer flow. *AIAA J.* **36**, 1983–1990.

Squires, K. D. 2004 Detached-eddy simulation: current status and perspectives. In *Direct and Large-eddy simulations — 5*, pp. 465–480. Dordrecht, The Netherlands: Kluwer, poitiers-Futuroscope, France, September 12 – 14, 2005.

Stolz, S. & Adams, N. A. 2003 Large-eddy simulation of high-Reynolds-number supersonic boundary layers using the approximate deconvolution model and a rescaling and recycling technique. *Phys. Fluids* **15**, 2398–2412.

Stolz, S., Adams, N. A. & Kleiser, L. 2001*a* The approximate deconvolution model for large-eddy simulation of compressible flows and its application to shock-turbulent-boundary-layer interaction. *Phys. Fluids* **13**, 2985–3001.

Stolz, S., Adams, N. A. & Kleiser, L. 2001*b* An approximate deconvolution model for large-eddy simulation with application to incompressible wall-bounded flows. *Phys. Fluids* **13**, 997–1015.

Tani, I. 1962 Production of longitudinal vortices in the boundary layer along a concave wall. *Journal of Geophysical Research* .

Urbin, G., Knight, D. & Zheltovodov, A. A. 1999 Compressible large eddy simulation using unstructured grid - supersonic turbulent boundary layer and compression corner. *AIAA Paper* 99-0427.

Urbin, G., Knight, D. & Zheltovodov, A. A. 2000 Large eddy simulation of a supersonic compression corner. *AIAA Paper* 00-0398.

Volkov, V. F. & Loginov, M. S. 2000 Computational study of supersonic flow over the wings at high angles of attack and sideslip in the framework of euler equations. In *International Confenference on the Methods of Aerophysical Research, Part 2*, pp. 149–157. Novosibirsk, Russia, July 9 – 16, 2000.

Volkov, V. F., Zheltovodov, A. A., Derunov, E. K. & Loginov, M. S. 2002 Numerical simulation of supersonic inviscid flow around lifting bodies. *Thermophysics and Aeromechanics* **9** (2), 215–232, (in Russian).

von Kaenel, R., Kleiser, L., Adams, N. A. & Vos, J. B. 2004 Large-eddy simulation of shock-turbulence interaction. *AIAA J.* **42**, 2516–2528.

Vulis, L. A. & Kashkarov, W. P. 1965 *Theory of the Viscous Liquid Jets*. Moscow: Nauka, (in Russian).

Williamson, J. H. 1980 Low-storage Runge-Kutta schemes. *J. Comput. Phys.* **35**, 48–56.

Xiao, X., Edwards, J. R., Hassan, H. A. & Baurle, R. A. 2003 Inflow boundary conditions for hybrid large eddy / Reynolds averaged Navier-Stokes simulations. *AIAA J.* **41**, 1481–1489.

Xu, S. & Martin, M. P. 2004 Assessment of inflow boundary conditions for compressible turbulent boundary layers. *Phys. Fluids* **16**, 2623–2639.

Yan, H., Knight, D. & Zheltovodov, A. A. 2001 Large eddy simulation of supersonic compression corner using ENO scheme. In *Third AFOSR Intern. Conf. on DNS and LES*, pp. 381–388. Arlington: Univ. of Texas, August 5–9, 2001.

Yan, H., Knight, D. & Zheltovodov, A. A. 2002*a* Large eddy simulation of supersonic flat plate boundary layer part II. *AIAA Paper* 2002-4286.

Yan, H., Knight, D. D. & Zheltovodov, A. A. 2002*b* Large-eddy simulation of supersonic flat-plate boundary layers using the monotonically integrated large-eddy simulation (MILES) technique. *Journal of Fluids Engineering* **124**, 868–875.

Yan, H., Urbin, G., Knight, D. & Zheltovodov, A. A. 2000 Compressible large eddy simulation using unstructured grid: supersonic boundary layers and compression ramps. In *International Confenference on the Methods of Aerophysical Research, Part 1*, pp. 215–224. Novosibirsk, Russia, 9 – 14 July, 2000.

Zheltovodov, A. A. 1979 Analysis of properties of two-dimensional separated flows at supersonic speeds conditions. In *Investigations of near-wall flows of viscous gas* (ed. academician N. N. Yanenko), pp. 59–94. Novosibirsk: Institute of Theoretical and Applied Mechanics, USSR Academy of Sciences, (in Russian).

Zheltovodov, A. A. 1991 Peculiarities of development and modeling possibilities of supersonic turbulent separated flows. In *Separated Flows and Jets: IUTAM Symposium* (ed. V. V. Kozlov & A. V. Dovgal), pp. 225–236. Novosibirsk, USSR July 9 - 13, 1990.

Zheltovodov, A. A. 1996 Shock waves/turbulent boundary-layer interactions – fundamental studies and applications. *AIAA Paper* 96-1977.

Zheltovodov, A. A. 2004 Advances and problems in modelling of shock wave turbulent boundary layer interactions. In *International Confenference on the Methods of Aerophysical Research, Part 2*, pp. 149–157. Novosibirsk, Russia, June 28 – July 3, 2004.

Zheltovodov, A. A., Borisov, A. V., Knight, D. D., Horstman, C. C. & Settles, G. S. 1992 The possibilies of numerical simulation of shock waves / boundary layer interaction in supersonic and hypersonic flows. In *International Confenference on the Methods of Aerophysical Research, Part 1*, pp. 164–170. Novosibirsk, Russia, August 31 - September 4, 1992.

Zheltovodov, A. A., Loginov, M. S., Maksimov, A. I., Adams, N. A., Knight, D. & Thivet, F. 2003 Problems, achievements and

prospects in supersonic turbulent separation research. In *Airgasodynamics in XXI century, all-Russian conference dedicate to 80th anniversary of academician G. G. Chernyi (book of abstracts)*. Moscow, Russia, January 27 – 30, 2003 (in Russian).

Zheltovodov, A. A., Schülein, E. & Yakovlev, V. N. 1983 Development of turbulent boundary layer under conditions of mixed interaction with shock and expansion waves. Preprint 28–83 ITAM, USSR Academy of Sciences, Siberian Branch, Novosibirsk, (in Russian).

Zheltovodov, A. A., Trofimov, V. M., Schlein, E. & Yakovlev, V. N. 1990 An experimental documentation of supersonic turbulent flows in the vicinity of forward- and backward-facing ramps. *Tech. Rep.* 2030. Institute of Theoretical and Applied Mechanics, USSR Academy of Sciences, Novosibirsk.

Zheltovodov, A. A. & Yakovlev, V. N. 1986 Stages of development, flowfield structure and turbulence characteristics of compressible separated flows in the vicinity of 2-D obstacles. Preprint 27–86 ITAM, USSR Academy of Sciences, Siberian Branch, Novosibirsk, (in Russian).

Zheltovodov, A. A., Zaulichnyi, E. G., Trofimov, V. M. & Yakovlev, V. N. 1987 Investigation of heat transfer and turbulence in the compressible separated flows. Preprint 22–87 ITAM, USSR Academy of Sciences, Siberian Branch, Novosibirsk, (in Russian).